Cadmium and Lead Thiosemicarbazide Complexes: Precursors for the Synthesis of CdS Nanorods and PbS Nanoparticles

Sibusiso Nkosikhona Mlondo

(991530)

Department Of Chemistry

University Of Zululand

Private Bag X1001

KwaDlangezwa

3886

July 2005

Cadmium and Lead Thiosemicarbazide Complexes: Precursors for the Synthesis of CdS and Nanorods PbS Nanoparticles

A dissertation submitted by

Sibusiso Nkosikhona Mlondo

991530

to the Faculty of Science and Agriculture in fulfilment of the requirements for the award of the degree of

Master of Science

in the Department of Chemistry

University of Zululand

Supervisor: Prof. N. Revaprasadu

July 2005

Declaration

"I declare that *'Cadmium and Lead Thiosemicarbazide Complexes: Precursors for the Synthesis of CdS nanorods and PbS nanoparticles'* is my own work, which was conducted in the Department of Chemistry at the University of Zululand and in the Department of Chemistry at the University of Manchester. I declare that all the sources used or quoted have been indicated and acknowledged by means of complete references"

Mlondo, Sibusiso Nkosikhona

.....

Abstract

This work reports the shape controlled synthesis of metal sulfide nanomaterials with varying morphologies using single source precursors based on the thiosemicarbazide ligand. The single crystal X-ray structures of $[Cd(NH_2CSNHNH_2)Cl_2]_n$, $[Cd(NH_2CSNHNH_2)_2Cl_2]_n$ and $[Pb(NH_2CSNHNH_2)(NO_3)_2]$ precursor complexes are reported and discussed. The non crystalline analogue of the cadmium complexes, $[Cd(NH_2CSNHNH_2)_2Cl_2]$ was also synthesized and principally used to determine the effect of the precursor concentration and the growth temperature on the growth and final morphology of the CdS nanoparticles. The precursors were thermolysed in a hot co-ordinating solvent such as hexadecylamine (HDA) for CdS and tri-*n*-octylphosphine (TOPO) for PbS, using the "one-pot" single-molecule precursor route. The shape was found to move from short rods and dots to long rods at higher temperatures, where the growth is not easy to control. By contrast, at moderate temperatures the shape evolution was the opposite with the precursor concentration being the variation, as we moved from higher to lower concentrations. On the temperature variable's front, higher temperatures were found to favour the formation of shorter rods and dots whereas lower temperatures favour longer rods. By varying the important parameters such as precursor concentration and reaction temperature, various nanomaterials with a range of morphologies and sizes could be prepared. The effect of the nature of the precursor was also varied by synthesising nanoparticles from different crystalline complexes of the same metal (cadmium) and ligand (thiosemicarbazide) as precursors, which were found to give the nanoparticles of different crystallinity and aspect ratios. $[Pb(NH_2CSNHNH_2)(NO_3)_2]$ was also used to synthesize PbS nanoparticles, in which determination shape control could not

be achieved. UV/Vis and photoluminescence spectra were used to study the materials optical properties of the material. The structural properties of the materials were studied by X-ray diffraction and TEM instruments.

Contents

List of figures

Abbreviations and symbols

Chemicals

Et	ethyl group
HDA	hexadecylamine
R	alkyl group
Me	methyl group
Hex	n-hexyl group
E	chalcogenide element (S or Se)
^{t}Bu	tert-butyl group
^{i}Pr	isopropyl group
M	transition metal
TOP	tri-*n*-octylphosphine
TOPO	tri-*n*-octylphosphine oxide
MeOH	methanol

Techniques and methods

CHN/Micro	Elemental
UV-Vis	ultraviolet-visible
IR	infrared
XRD	x-ray powder diffraction
TGA	thermogravimetric analysis
TEM	transmission electron microscopy

Symbols and constants

k	wave factor
a.u.	arbitrary units
d	diameter
R	gas constant
ε	dielectric coefficient
m*	effective mass (m_e*: electron; m_h*: hole)
T	temperature
E	energy
E_g	band gap energy
E_p	phonon energy
f	oscillator strength
h	Planck's constant
e	elementary charge
t	time
n	refractive index
N	complex index of reflection
k	proportionality factor
α	absorption coefficient
I	intensity
ν	frequency
rf	radiofrequency
λ	wavelength

λ_{exc}	excitation wavelength (luminescence)
σ	specific surface energy
V_m	molar volume of the material
S_b	solubility of bulk crystals
S_r	solubility of nanocrystals
μ	chemical potential
δ	surface atom ratio
$\propto$	proportionality sign

Acknowledgements

I would like to thank Prof. Neerish Revaprasadu for supervising my work. Thank you for being there with your directional guidance and warm support during the good and hard times of my work, and to warm heartedly be there when you had to travel an extra mile beyond your professional capacity to make sure my interests are tended, both at UZ and Manchester. I'm really thankful. My gratitude also goes to Prof. G. A. Kolawole for his unparalleled support and guidance throughout all the years of my Chemistry career up to now. Your parental pieces of advice and guidance are of huge value in my career and life at large.

Words can not adequately express my deep sense of gratitude to Dr. Paul Christian for supervising and shaping up my work in Manchester. I would also like to thank Prof. Paul O'Brien for inviting me to the University of Manchester at the first place and believing in my potential when there was nothing at hand, and also for his overall supervision during my visit. My thanks also go to the whole POB Group for their support and help during my visit. This work wouldn't have been this far if it wasn't for the XRD, TEM, CHN and Mass spectroscopy done at the University of Manchester, thank you again to Prof. P. O'Brien and the responsible technical staff. I would also like to gratefully acknowledge Dr. M. Heliwell and Dr. James Raftery for their precious time devoted to solve my crystal structures. I also thank Keith Pell at Queen Mary and Westfield University for the TEM images.

I sincerely thank CSIR for financing my studies. My thanks are also extended to NRF/RS funding for my subsistence support and the programme through which I found myself in Manchester.

To my loving family; Ma, Baba, S'du, Malungi, Thulile, and Ng'theni. Thank you for your love, endless support, understanding and believing in me at all times. You are the motivation that keeps me going on. To Mja, thank you for all your brotherhood love and support man. I also thank Mom Phila in Preston for all her love and support during my visit in Manchester. Thank you for all your generosity,

I'll make it up to you someday. I'm also indebted to Miss N. P. Ngcobo, you and I know how I wouldn't be this far if it wasn't for your warm heart. I would also thank Mr M. Hlongwane for his compassion to recollect my career when my hopes were lost, I'm really thankful. To Mrs Z. Ndlela and family, my one and the only Uncle (S'fiso Makhunga), Aunt Gugu and Dumisani Makhunga for their love and support throughout my career up to now.

I extend my gratitude to the UZ Department of Chemistry staff, and the research group; Justice, Sosibo, Peter, Phumudzo, Chili and Nosipho for their cooperation during work. Thank you very much to Justice for all his useful discussions and suggestions in the lab and results. I also sincerely thank Prof. and Mrs Revaprasadu on a personal note for being my second family at the house in Manchester, I really enjoyed staying with you and miss the good times we had. To my friend Sos, man, thanks for everything "I won't be particular on this one Chief", long live to the brotherhood. To my cousin and my friend "Mzala" (Dumisani), you are a star you know that, and keep shining, thank you for being there at all times.

None of this would have been possible without the Almighty God, Praise to Him.

This Dissertation Is Dedicated

To My Loving Ma, Baba,

Sdu, Malungi, Thulile and

Ng'theni

Chapter 1

Introduction

1.1 General Introduction to Nanoparticles

Nanoscale materials have attracted significant scientific and industrial interest during the last decade.[1-5] These materials are novel compounds of theoretical interest currently, but have huge potential to develop as important classes of materials for the electronics and photonics industries in the current century. This field of research has been widely recognized as one of the most promising and rapidly emerging research area in various scientific disciplines. The functional materials for information storage have stimulated great interest in recent years, with metal sulfide semiconductor nanomaterials being an area of intense activity.[6-8] The ultimate scientific and technological impact of these materials mainly depend on their novel electronic, optical, and catalytic properties. Hence, studies concerning quantum and electronic confinement observed in these materials are of exceptional importance.

Semiconductor nanoparticles are materials which fall in an intermediate position between the metals and insulators, exhibiting both physical and chemical properties within an intermediate state of matter, between molecular and bulk. These materials have dimensions ranging from 1-20 nm, which allows them to exhibit unique properties that are due to their reduced size in relation to the excitonic radius of their bulk materials and their large surface to volume ratios. The quantum size effect of nanomaterials results in their exhibiting novel electronic, magnetic and optical mechanical properties that differ from their bulk counterparts. Metal chalcogenide nanocrystals have been the most studied among the various nanocrystals due to their

enhanced quantum confinement effects and photoemission characteristics. These nanocrystals have been applied to many different technological areas including biological labeling and diagnostics, light emitting diodes, electroluminescent devices, photovoltaic devices, lasers and single electron transistors.[9-11]

Over the past 15-20 years, remarkable progress has been made in the synthesis of the nanomaterials using various methods. II-VI semiconductor quantum dots were the materials of immense interest since they exhibit a wide range of electrical and optical properties that are tunable by tailoring the sizes and shapes of the nanocrystals and consequently find potential applications in optoelectronic devices.[12,13] One of the first attempts to produce II-VI nanoparticles by Spenhel, *et al.*[14,15] was the synthesis of the colloidal suspensions where CdS was formed by the precipitation of Cd^{2+} in aqueous solution by adding H_2S. Growth was controlled conveniently by using microheterogeneous media, which was pioneered by Steigerwald and Brus,[16] and Petit, *et al.*[17] Subsequent interest was devoted to the study focusing on the synthesis of II-VI quantum dots using a very successful organometallic process developed by Bawendi, Alivisatos and their co-workers.[18,19] The nanoparticles prepared by this method were of high quality, but the reaction required harsh conditions such as injection of hazardous metal alkyls at elevated temperatures, which was clearly undesirable for health and safety. Trindade and O'Brien[20,21] investigated cadmium dithio- and diseleno- carbamate complexes as single molecular precursors for preparation of TOPO-capped II-VI materials. The use of single source molecular precursors is a very good way to avoid such problems incurred in organometallic route, since the metal chalcogen bond is

already in place in this route. Revaprasadu, *et al.*[45] also reported the synthesis of many metal chalcogenides nanoparticles including the doped nanoparticulates using single source complexes. Thiourea, xanthate and the thiosemicarbazide complexes of cadmium and zinc were also used by Revaprasadu *et al.*[45] and Nair, *et al.*[22,48] as the single source precursors to synthesize the nanoparticles that displayed both isotropic and anisotropic morphologies. Recent interest in this field is now devoted to the control of size in the quantum confinement range, since the electronic properties of the nanocrystals are also shape-dependent. It is a challenge to chemists to synthesize anisotropic shaped metal chalcogenides nanoparticles, since they offer tunability of properties of materials via control of shape in addition to size-dependent quantum confinement effects.

1.2 Electronic properties of nanoparticles

One of the defining features of a semiconductor is the energy gap separating the conduction and the valence energy bands. The color of light emitted by the semiconductor material is determined by the width of the gap.

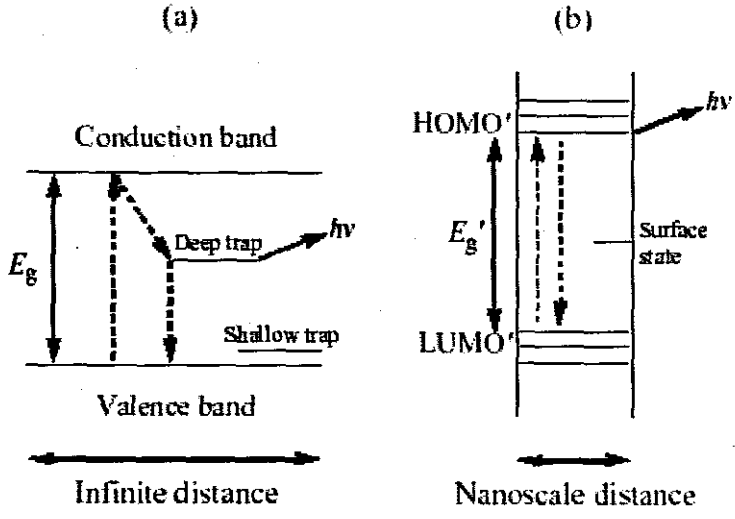

Figure 1.1: *The spatial electronic state diagram showing the quantum confinement effect in bulk semiconductors (a) and nanoparticles (b).*[24]

For a semiconductor crystal, electronic excitation consists of loosely bounded electron-hole pair (Mott-Wannier exciton) usually delocalized over a length much longer than the lattice constant. For the exciton to occur, $h\nu$ > energy gap. Pumping energy into a semiconductor can excite an electron, e^-, into the conduction band (Figure 1.1), leaving behind a hole, h, in the normally filled valence band, and thus an electron-hole pair is created. The electron and hole each relax to the respective band edge states by non-radiative processes. During the band edge transition a photon is emitted as the excited electron spontaneously recombines with the hole. The band-edge is explained as the direct recombination of charge carriers from atomic-like orbitals. Charge carriers in bulk semiconductor recombine from deep and shallow traps giving emission at different wavelengths from the band edge.[23]

In the case of nanoscale semiconductor particles with smaller sizes (<10 nm), the situation, however, changes. As the diameter of the crystalline material approaches the exciton Bohr diameter, its electronic properties start to change. This size range corresponds to the regime of the so-called quantum confinement effect, which can be observed as a blue shift in the band gap or exciton energy. The charge carriers are confined in all three dimensions in a quantum dot and thus the exciton has zero degrees of freedom for its motion, with the result that the electron exhibits a discrete atomic like-spectrum. As a result of these geometrical constrains an electron feels the particle boundaries and responds to particle sizes by adjusting their. This phenomenon is known as the quantum size effect. [23,24]

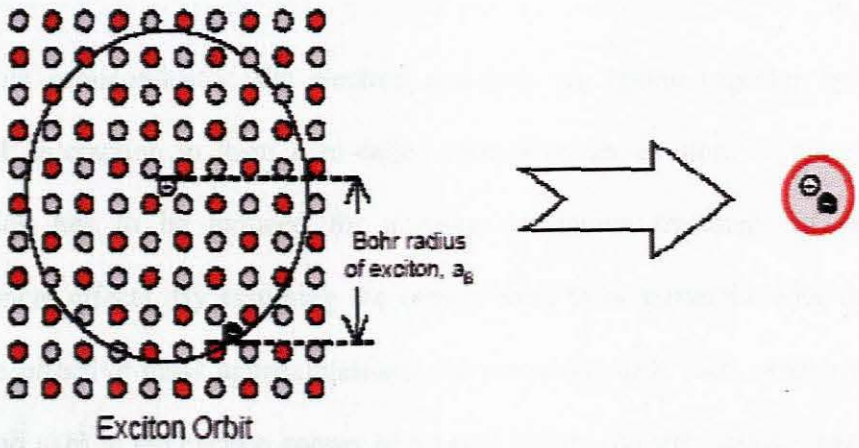

***Figure 1.2**: Simulation of the exciton Bohr radius, and its confinement.*[25]

Nanocrystalline materials which conserve the wave function are called direct band gap materials, and those where the lowest electronic transition between valence band and conduction band is forbidden are said to be indirect band gap materials, which have

very small absorption coefficients. Typically, bulk samples of CdS, irrespective of their size, once > ca. 20 nm will absorb all electromagnetic radiation with an energy greater than the band gap ($h\nu > 2.42$ eV); which is classified as direct band gap in this case. However, as particles become smaller, their electronic structure starts to change as highlighted previously. Eventually continuous bands break down and there are discrete bonding and antibonding orbitals in this material. The electronic properties of such small particles are more like those of the molecule than an extended solid. Figure 1.1 shows a spatial electronic state diagram showing the quantum confinement effect. As the cluster properties are intermediate between molecules and bulk semiconductors, the quantum size effect can be best explained with hybrid molecular and semiconductor nomenclature.

In a bulk semiconductor, the electron and hole are bound together by a screened Coulomb interaction to form a so-called Mott-Wannier exciton.[16] This electron-hole interaction has to be induced for a more qualitative treatment of the quantum confinement effects. By assuming the energy band to be parabolic near the band gap (i.e., the effective mass approximation), the size-dependent shift (with respect to the bulk band gap) in the exciton energy of a small cluster (cluster radius ~ exciton radius) can be derived as

$$E(R) = E_g + \hbar^2\pi^2 / 2\mu R^2 - 1.786e^2 / \varepsilon R - 0.248E^*_{Ry} \qquad (1)$$

where R is cluster radius, $1/m = 1/m_e^* + 1/m_h^*$, m_e^* is the electron effective mass, m_h^* is the hole effective mass, ε is the dielectric constant, and E^*_{Ry} is the effective Rydberg

energy, $e^4/2\varepsilon^2\hbar^2(m_e^{*-1} + m_h^{*-1})$. The first term in the above equation is the band gap of the bulk materials, the second represents the particle-in-a-box quantum localization energy and has a simple $1/R_2$ dependence, the third term the Coulomb energy with $1/R$ dependence, and the last term is the result of the spatial correlation effect. This last size-independent term is usually small but can become significant for semiconductors with small dielectric constant. Therefore, the cluster radius can be easily determined according to the above formula based on the absorption spectra.[23]

The quantum size effect can be clearly explained by a simple quantum size box model in which the electron is restricted in all three dimensions by impermeable walls. For a spherical quantum dot with radius R, this model predicts that a size independent contribution to the energy gap is simply proportional to $1/R^2$, which implies that the gap increases as the quantum dot size decreases. Moreover, quantum confinement leads to a collapse of the continuous energy bands of a bulk material into discrete, atomic-like energy levels.[23] The discrete structure of energy state leads to a discrete absorption spectrum of quantum dots, which is in contrast to the absorption spectrum of a bulk semiconductor.

The nanocrystals quantum dots discussed earlier in this context are small quantum dots made by organometallic chemical methods and are composed of a semiconductor core capped with a layer of organic molecule. The organic capping prevents uncontrolled growth and agglomeration of nanoparticles. It also allows the nanocrystals quantum dots to be chemically manipulated as if they were large molecules, with solubility and

chemical reactivity determined by the identity of the organic molecules. The capping also provides electronic passivation of the nanocrystals quantum dot. It terminates the dangling bonds that remain on the semiconductor's surface as they might affect nanocrystals quantum dot's emission efficiency. This is done through a mechanism where electrons are rapidly trapped at the surface before they have a chance to emit a photon. Because of quantum size effect, this ability to tune nanocrystals quantum dot translates into means of controlling its various properties such as emission and absorption wavelengths.

1.3 Luminescence Properties

Luminescent properties i.e. emission color, quantum yield, luminescent lifetime and stability must be strictly controlled to realize a wide range of potential applications of the semiconductor nanocrystals. The fluorescence spectroscopy is the key tool to examine the nanoparticle's size and quality. Nanoparticles that fluoresce with a narrow line width and small Stokes shift are dominated by what is referred to as near band gap emission and characterized by a generally continuous surface with most surface atoms exhibiting the coordinated and oxidation state of their bulk counterparts. In contrast, nanoparticles that emit broadly with a larger Stokes shift are considered to exhibit deep trap emission.[24]

Deep trap emission is characterized as emission from the recombination of trapped electrons and holes with broad energy distributions. For example, the sulfur deficiency in CdS is due to the $S^{2-}(V_s^+)$ defects. The V_s^+ is a deep trap and can exothermically

extract an electron from the valence band. A hole is left behind by an electron, which localizes away from the V_s^+ site. It is virtually impossible for V_s^+ site to pull out another electron from the valence band. The V_s^+ vacancy sets a deep (c. 0.007 eV) trap for a photo-generated electron in the conduction band, which combines forming the V_s^+ state. The photo-generated electron is quickly trapped by the V_s^+, forming a V_s^0 site, which could then either be quenched by some surface species or recombine with the nearest pre-existing hole.

The role of surface in determining the luminescence quantum yields of semiconductors is fundamental and has long been recognized and ascribed to the higher concentration of defects at the surface e.g. unsaturated bonds, ion vacancies, disorder due to adsorbed impurities, or uncommon oxidation states, which gives rise to high density mid-gap states acting as electron and hole states. The surface properties are expected to have large influence on the optical properties of the semiconductor nanocrystals because of the high surface to volume ratio.

When a nanoparticle size is reduced such that the particle is essentially all the surface, the curvature of the surface is so high that virtually all the surface atoms have slightly different coordination or effective oxidation state.[26-29] The experimental and theoretical studies of very small metal chalcogenides are examples of such nanoparticle systems that are dominated by surface interactions. These small nanoparticles emit light that is characteristic of deep trap luminescence, unless they are coated with a wider band gap material which confines the carriers to the materials core.

To understand how the growth conditions that determine the surface structure of the nanocrystals contribution of each individual parameter (growth temperature, precursor concentration and capping group) should be considered, and later consider the effect of their combination. The solvent composition is known to have large impact on the growth kinetics and quantum yields of the nanocrystals.[29-31] The influence of the growth temperature can be understood in terms of the growth rates and surface annealing. The initial period after hot injection is characterized by rapid growth which results in the surface disorder and low quantum yields. Surface ordering and reconstruction can subsequently be achieved during annealing (prolonged heating), reducing the concentration of the defects and increasing quantum yields.

The use of lower temperatures during the surface reorganization process has proven to be very advantageous in maintaining high yields for hours during the growth.[29] Higher growth temperatures lead to faster growth rates and therefore the surface roughening and degradation compete with surface ordering. Higher temperatures induce faster surface degradation, which reduces the luminescence efficiency shortly after the maximum efficiency has been reached. Surface degradation can also be observed at lower temperatures for specific growth, but after much longer heating times, as could be expected for thermally induced process. This could be stopped by quenching ensemble of nanocrystals with optimum surface-to-room temperature. Furthermore, addition of metal or chalcogenides precursors (in case of metal chalcogenides) during thermolysis has the effect of bringing back the quantum yields and thus luminescence,

by filling the vacancies of either the metal or chalcogenides and growing the fresh surface.[29]

In broad scope of semiconductor quantum dots, high emission from band edge states would be required if one wants to study their electronic structure or more practically if they are to be used as emitters in any application. It is most unfortunate that the band edge emission from nanocrystals has to compete with both radiative and non-radiative decay channels, originating from surface electronic states. Coating the surface of the nanocrystals with suitable organic molecules can minimize this problem. The judicious choice of passivation agent can, in fact, improve the size-dependent band edge state luminescence efficiency, while promoting the solubility and the processibility of the nanoparticles. Passivation by means of organic molecules accomplishes this role and is widely used but can sometimes have a drawback of incomplete or irreversible passivation. This passivation can expose some of the regions of the surface to degradation effects such as photo oxidation. In some cases, chemical degradation of the ligand molecule itself or its exchange with other ligands might lead to unstable surfaces and therefore unusable nanocrystals.

In the case of nanorods, there are two additional factors that might further reduce the luminescence band edge states when compared to spherical nanocrystals. In nanorods, the surface-to-volume ratio is higher than in spheres and this increases the occurrence of surface trap states. In larger dots the increased delocalization of carriers reduces the overlap of the electron and hole wave functions, lowering the probability of radiative

combination. The delocalization of carriers should be particularly higher in nanorods, where they are free to move throughout the length of the rod thereby leading to reduced luminescence in nanorods. Quantum confinement effects are most prominent in the luminescent properties of the nanoparticles in the so called strong confinement regime when $L \leq a_B$ where a_B is the exciton Bohr radius and L is the size of the nanocrystals, as opposed to these bulk solids with $L/a_B \longrightarrow \infty$. At the same time, nanocrystals, even with a size of an order of magnitude larger than the exciton Bohr radius still show quantum confinement effects as well as the same bulk properties and are interesting areas for research.[32]

1.4 Preparative methods for the synthesis of the nanoparticles

1.4.1 Colloidal Routes

La Mer *et al.*[33] explained the synthesis of highly monodispersed colloids in the past decades; they suggested that if seeds (nuclei) could be made to grow in concert into larger particles, monodispersed sols could be formed. The first reported routes to such small particles involved the precipitation of dilute colloidal solution and the cessations of growth soon after nucleation. In early years of this work, the particles were typically monomeric. Later on, nucleation and growth were properly monitored and the particles with dimensions of the order of the nanometers could be reproducibly synthesized as small crystals which are less stable, dissolved, and then recrystallize on larger and more stable crystals. This process is known as Oswald ripening. Solvent, pH and the passivating agent are chosen such that nanoparticles possess low solubility. The highly monodispersed samples are obtained if nucleation and growth process are distinctly

separated (fast nucleation and slow growth). The colloidal growth stability of those crystals has been improved by using solvents with low dielectric constant or by using stabilizers such as styrene/maleic acid copolymer. Henglein and Weller *et al.*,[14,15] and Brus *et al.*[16,19,34] have made significant contributions to this field, especially studies of CdS.

Reaction between aqueous solution of $CdSO_4$ and $(NH_4)_2S$ is a typical example for colloidal route preparation method. The particle size of the CdS was controlled by varying the pH, altering the nucleation kinetic. Although these methods can be efficient, some important semiconductors cannot be easily synthesized and there is annealing of amorphous colloidal particles which tend to be low temperature processes producing poorly crystalline material.[35] The particles prepared via this method are not sufficiently stable at higher temperatures before annealing without agglomeration.[36] Colloidal methods have also been used to grow a solid on the surface of another solid, the latter acting as a seed for heterogeneous nucleation of the former. TiO_2/Cd_3P_2 and the other similar systems are good examples of the system of this nature.[37]

1.4.2 Synthesis in confined matrices

Quantum dots have been synthesized by using materials which provide distinct defined cavities, being used as nanomeric size reaction chambers.[38] Zeolites,[39] micelles molecular sieves[40] and polymers[41] have all been used to restrict growth. The matrix may also play a role in determining the final properties of the particle; e.g. micelles are labile. Nanoparticles of cadmium and zinc chalcogenides have produced inverse

micelle solutions. A microemulsion containing the metal ion was reacted with a silyl chalcogenide resulting in nanoparticles; the surface was then capped by phenyl groups or another semiconductor. The surface compositions of the crystal were interesting owing to their ability to react further with other silyl groups owing to excess Cd^{2+} sites effectively growing larger and developing a different surface capping.[42,43]

Internal cavities of the zeolites have also been used as substrates to grow the nanocrystals; which also limits the particle size of the materiral, typically less than 20 nm. Cadmium sulfide has been synthesized in two different zeolites by ion exchange from the sodium cationic form to the cadmium cationic form, followed by the exposure to H_2S gas. The size of the nanoclusters could be controlled by using either the potassium or sodium resin, which altered pore diameters. Transition metal chalcogenides have also been reported to be synthesized in the cavities of zeolites.[36]

1.4.3 Metal-Organic Routes

Murray, *et al.*[44] first prepared the semiconductor nanoparticles using organometallic and/or metal-organic compounds under anaerobic conditions, involving organic main group compounds. In this method, a volatile metal alkyl and a chalcogenide source TOPX (tri-*n*-octylphosphine chalcogenide) was mixed in TOP (tri-*n*-octylphosphine) and injected into hot TOPO (tri-*n*-octylphosphine oxide), a polar coordinating Lewis base solvent at high temperatures (120-300 °C). The thermolysis of molecular precursors in high boiling point coordinating solvent like TOPO, was reported to be a very efficient method not only for II—VI, but also for III—V nanomaterials, which are

more difficult to prepare because of their numerous difficulties in preparation such as their increased covalent nature, highly toxic reagents used and fast oxidation.[44,45] During this preparation method, short burst nucleation was followed by slow growth and annealing, consistent with Ostwald ripening. This is then followed by the addition of the solvent to a cooled solution, thereby increasing the barriers to flocculation. The solid nanoparticles were then separated from decomposition by-products in the centrifuge, and then the solids were dissolved in a solvent (e.g. toluene) followed by centrifugation to dispose the by-products resulting in an optically clear solution of TOPO-capped nanoparticles. The coordinating solvent plays a major role in stabilizing the nanocrystalline colloidal dispersions and passivating the semiconductor surface.

Using a similar approach as above, III-V nanomaterials were also prepared by thermolysis of single molecular source precursors at 167 °C in 4-ethylpyridine acting both as a solvent and a capping agent. High quality nanoparticles were produced showing distinct quantum size effects in their optical properties.[45] Alivisatos, *et al.*[46] reported the synthesis of exclusive TOPO capped InP nanoparticles using a similar method to that of Murray, *et al.*[44] $InCl_3$ was reacted with $P(SiMe_3)_3$ in hot TOPO (Scheme 1), with subsequent annealing of the particles in the presence of a surfactant (dodecylamine).

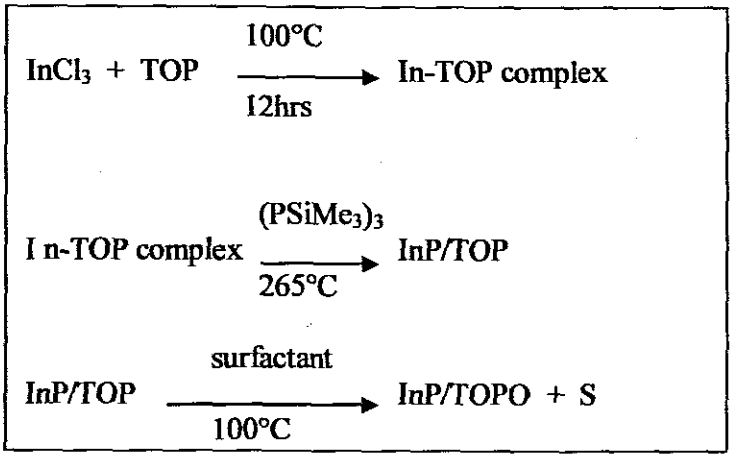

***Scheme 1:** Preparation of the TOPO capped InP nanoparticles, via the metal-organic route*

Trindade and O'Brien,[20,21,47] first reported the use of dithio- and diseleno-carbamato complexes as single molecule precursors for the preparation of the TOPO-capped II-VI materials. Bis(dialkyl/selenocarbamato)cadmium(II)/zinc(II) compounds were thermolysed in 4-ethylpyridine to prepare MS and MSe nanoparticles (M = Cd, Zn). The preparation of these precursors follow a simple procedure in which CSe_2 or CS_2 is reacted with an excess of the amine and hydroxides at below 0 °C to give the dithio/seleno carbamate as the salt. This compound is then reacted with stoichiometric quantity of aqueous solution of cadmium(II) chloride/zinc(II) chloride, to give the (dialkyldithio/diseleno-carbamato)cadmium(II)/zinc(II) compound as a precipitate, which is then recrystallized to give the pure precursor. The O'Brien group prepared a number of bis(dialkyldithio/diseleno-carbamato)cadmium(II)/zinc(II) compounds of the type $M(E_2CNRR')_2$ either containing symmetric amine alkyl groups (R = R′= alkyl) or having asymmetric groups on the amine (R = Me or Et and R′ = ^{n}Hex, ^{n}Bu) (see the reaction scheme: 2).[20-22,37,45,47]

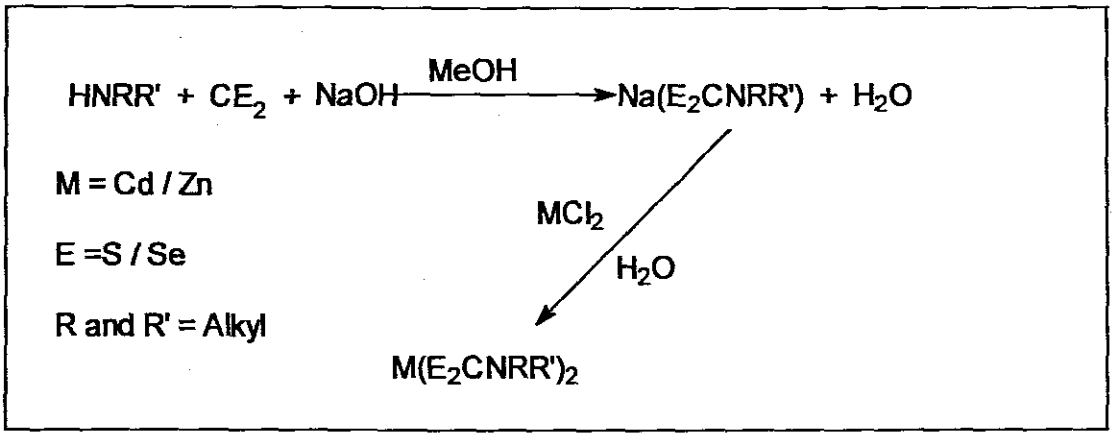

Scheme 2: *The schematic reaction for the preparation of single-source precursors*

This method has an advantage over the other methods of preparation as it avoids the need for volatile, pyrophoric and toxic decomposition by-products. The use of this route lessens the chances of incorporating impurities into the nanoparticles, and low deposition rates are possible. Revaprasadu, *et al.*[45] reported the use of the single source precursor method in preparing InS and InSe nanoparticles, using similar metal thio- and seleno- precursors.

Nair, *et al.*[48] has recently reported the synthesis of CdS nanoparticles from the complex of cadmium with dithiobiurea. The precursor was decomposed in tri-*n*-octylphosphine oxide to give CdS nanoparticles that show quantum confinement effects with characteristic close-to-band edge luminescence. Anisotropic-shaped CdS nanocrystals were also prepared by Nair, *et al.*[22] using $[Cd(NH_2NHNH_2)_2Cl_2]$ as a single-source precursor. The prepared rods exhibited a very slight blue shift in relation to bulk CdS.

1.5 General applications of the nanoparticles

The most physical advancement to date has undeniably been in the field of nanomaterials, where the speed of development has been remarkable. Of course, it could be argued that nanomaterials are not new, given that Raney nickel catalysts, nanoporous aluminosilicate zeolites, activated carbons, glazes for early dynasty Chinese porcelain, and a Roman 'Lycurgus cup' (Fig. 1.2) have been around for centuries. What is certainly new, however, is the availability of an extraordinarily wide range of nano-sized materials, many of which have unique functional properties with potential in many exciting new applications. Given that the venture capital community has become relatively conservative over the last few years, it is not surprising that a large amount of the nanotechnology start-ups attracting venture capital funding are in the nanomaterials area.

***Figure 1.3**: The Lycurgus Cup made of gold nanocrystals, from 4th Century A. D.*

An assortment of up to date technologies and technological devices are already employing the use of nanoparticles with communal and economic impact.

1.5.1 Biological Applications

It is the application of nanomaterials to biology and medicine which has attracted the most attention in modern-day research. Living organisms are built of cells that are approximately 10 microns in size, with the cell parts a fraction of this. Proteins, which are about 5 nanometers, are even smaller. Now one could imagine nanoparticles which are 1-3 nanometers in size which can act as probes within cells causing much interference. In order for the nanoparticles to function as biological labels or tags, the particles have to interact with the biological targets, which can be done through the attachment of a molecular coat or layer which acts as a bioinorganic interface. Antibodies, biopolymers or monolayers of small molecules that make nanoparticles compatible are examples of biological coatings. A control of the average particle size and size distribution tunes the wavelength of emission in wide range of wavelengths, making them very efficient probes.

The nanoparticles are brighter and last longer than conventional fluorescent dyes making them potentially useful for diagnosing cancers. Recent animal studies conducted showed that nanoparticles could be used to map the lymph node nearest a breast cancer. These nodes are checked to see if the cancer has spread. The fluorescent properties of the particles also could make them an energy source for certain therapies. Inactivated drugs could be attached to nanoparticles and once they have reached a tumor they could be activated by a flash of light. Insoluble nanoparticles of varying sizes and colors could be packed inside a bead the size of a virus. Subsequently each

microbead has a distinctive optical signature that can be used as a barcode to label individual cells and proteins.

The majority of commercial nanoparticle applications in medicine are focused on drug delivery. Magnetic nanoparticles have properties which would render them useful in biomedicine. The magnetic nature of the particles implies that they could be manipulated from an external magnetic field gradient. This almost "remote control" action means that they could deliver a package such as an anticancer drug to a targeted region of the body. The nanoparticle could also be heated through transfer of energy from the exciting field to the nanoparticle thereby making them useful as hyperthermia agents, delivering toxic amounts of thermal energy to tumors or as chemotherapy and radiotherapy enhancement agents.

Recently a variety of magnetic nanoparticles have been developed to deliver drugs to specific sites in *vivo*. The magnetic component of the particle is coated by a biocompatible polymer such as PVA (polyvinyl alcohol) or dextran. The coatings protect the magnetic particle from the surrounding environment. Functional groups such as carboxyl groups, biotin, avidin, carbodi-imide could also be attached. These molecules could then be used as attachment points for the coupling of cytotoxic drugs or target antibodies to the carrier complex. This advancement overcomes a major disadvantage for impreciseness of most chemotherapies, in which intravenous administration of the drug results in side effects as the drug attacks healthy cells in addition to the target tumor cells. Another breakthrough has been the transportation of

drugs bound to nanoparticles across the blood brain barrier (BBB). The nanoparticle/drug systems are coated with a surfactant. The drugs are attached to the surface of the nanoparticles and/or incorporated into poly(butylcyanoacrylate) particles (PBCA). This almost "Trojan horse" drug delivery mechanism allows for efficient delivery of the drug specifically into the Central Nervous System (CNS).

1.5.2 Energy Storage

Energy storage is needed to store electricity, heat and cold, after it is produced at times of low demand and low cost and from intermittent energy sources such as wind and solar power. Reliable and affordable energy storage is a prerequisite for using renewable energy in remote locations, for integration into the energy system and the development in a future decentralized energy supply system. Energy storage therefore has a pivotal role to play in the effort to combine a future, sustainable energy supply with the standard of technical services and products that we are accustomed to and need. Moreover, due to increased global consumption of energy owing to industrialisation, alternative sources of energy may be essential, in which case renewable energy sources such as hydro energy, combustible renewables, solar and wind may play an increasing role in total energy consumption. Novelty will be a driver of the uptake of renewable energy sources and there are forecasts in cost reductions in some renewable energy technologies.

Nanotechnology is making a significant contribution in innovation in the area of solar photovoltaic electricity production. The enormous amount of solar energy radiated

towards the earth has not been optimally converted into electricity. It is very clear that in order for solar cells to become an attractive and commercially successful source of energy, there has to be an increase in efficiency and decrease in cost of manufacturing and maintenance of a solar conversion system. Nanotechnology is currently being used to address this dilemma, since semiconductor nanoparticles exhibit the properties of being potentially ideal for increasing the efficiency of the solar cells. The engineering of the band gap through size tuning renders them useful in optimizing the single junction solar cells. The maximum attainable thermodynamic conversion efficiency of solar photon conversion of about 66 % could be potentially achieved by utilizing hot photogenerated carriers to produce higher photovoltages or higher photocurrents or by creating multiple junction cells. The synthesis of nanoparticles in solution makes it easy for them to be processed in semiconductor polymers or porous sol-gel films. This low temperature liquid phase processing allows for the creation of junctions on inexpensive substrates such as coated glass, metal sheets etc. thereby reducing the cost of manufacture.

The fundamental pathways for enhancing the conversion efficiency can be accessed through photovoltaic cells composed of nanocrystal arrays, through the dispersion of nanoparticles in organic semiconductor polymer matrices or through nanocrystal-sensitized TiO_2 solar cells also known as Gratzel cells (Fig. 1.3).[96-98] The Gratzel cell consists of photoelectrode made up of 10-20 micron film of porous TiO_2 particles that are 20 nm in diameter. Organic dye molecules are adsorbed in the pores between the TiO_2 particles surrounded by an electrolyte fluid. The cell is completed by two

transparent electricity conducting electrodes and a catalyst. The Gratzel cell effectively separates light collection and charge separation with dye and Titania respectively, unlike conventional solar cells which perform both functions at a single junction.[96-98]

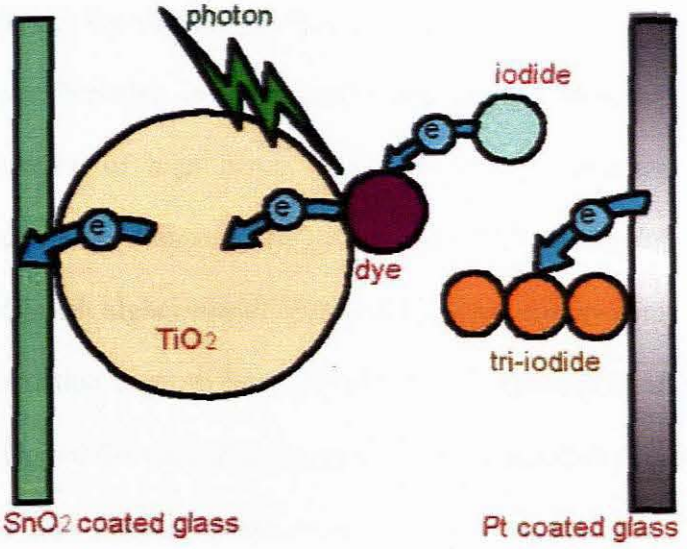

Figure 1.4: *The schematic diagram of the TiO_2 Gratzel cell.*[96]

For the nanocrystal-sensitized cell, the dye molecules are substituted by nanoparticles such as InP, CdSe, CdS and PbS. The use of nanoparticles enhances efficiency and lengthens operational lifespan. Unlike organic dyes that absorb over a narrow region, nanoparticles absorb strongly all light greater than the band gap thereby converting a higher proportion of light into energy. Another advantage is the relative stability of nanoparticles compared to organic dyes which tend to photobleach over a short period of time. A recent breakthrough has been the attainment of photoelectric conversion efficiencies of up to 11 %. Some start-up companies are already producing Gratzel cells for niche markets.

Energy storage devices may be broadly characterized by their energy density (energy stored per unit volume or mass) and by their power, i.e. how fast that energy can be delivered from the device. At one end of the scale, conventional capacitors have enormous power but store only tiny amounts of energy. At the other end, batteries can store lots of energy but take a long time to be charged up or discharged. That is, they have low power. Relative to these established technologies, supercapacitors offer a unique combination of high power and high-energy performance parameters with commercial relevance. Nanotechnology is being used to develop smaller and faster supercapacitors, with higher-power density and higher energy density. Nanotechnology will allow production costs to be lowered with an expectation of 50% cost reduction year-on-year. One of the enabling materials of supercapacitors is carbon, and it is in the engineering of this material where nanotechnology is utilized. Based on activated carbon an increase of the surface area is looked for by working down the particle size from 50 nm to 2 nm. Also the pore size is tailored for the particular power and amount of energy store required.

1.5.3 Fuel Cells

There is a lot of discussion at the moment about the Hydrogen Economy, where hydrogen will be the dominant fuel, converted into electricity in fuel cells, leaving only water as waste product. Hydrogen is not freely available in nature in large quantities, so it must be produced by conversion of other energy sources, including fossil fuels and renewables. Only renewables-based hydrogen production can contribute to CO_2 emission reduction. Current renewable production methods of hydrogen include H_2 production from biomass, microorganisms and algaes, from water by electrolysis

(where the electricity has been produced by wind, solar or hydro-energy). Metal-organic 'nanocubes' for storing hydrogen in portable fuel cells is currently being developed for laptop computers and other portable devices. The nanocubes consist of a periodic lattice of terephthalic acid and zinc oxide molecules connected through carboxylate bonds, with pores in the nanometre range. They can store hydrogen in the pores at 10x the atmospheric pressure. They can release the hydrogen to a fuel cell, which can work for 10 hours. The material is about twice as porous as carbon nanotubes. At the moment kilograms of the nanocubes with a controlled size are being produced. This production still needs to be scaled up for mass production.

Hydrogen can be stored in different kinds of materials, in gaseous, liquid or solid form. Early forms of solid storage were the use of conventional hydride materials. This was followed by the shift to amorphous hydrides. In the 1990s the focus has been on nanostructured hydrides including carbon nanotubes, nanomagnesium-based hydrides, metal hydride-carbon nanocomposites, nanochemical hydrides and alanates. SOFC (Solid Oxide Fuel Cell) fuel cells could be used for the electrochemical oxygen production in manned space stations, or for the in-situ resource production on other planets. Nanotechnology offers different possibilities to increase the conversion efficiencies of fuel cells, in particular, within the ranges of catalysts, membranes and hydrogen storage, which in many cases is critical for the employment of fuel cell technology in space.

Precious metal nanoparticles improve the high-efficient production of hydrogen in direct methanol fuel cells. This type of fuel cell needs liquid methanol as fuel, from which the hydrogen is generated by a catalyst. The main obstacle here is the poisoning of the catalysts through by-products like carbon monoxide. Improved nanotechnological catalysts, which are more insensitive against carbon-containing gases, could contribute to a solution of this problem. One of the main obstacles to the implementation of fuel cells for mobile application is, at present, still the technologically and economically reasonable storage of the fuel (especially hydrogen). Nanomaterials, due to their increased active surface area, basically possess potential to be lightweight high-efficient storage media for hydrogen. With regard to operating conditions (temperature, pressure), different material types should be taken into consideration. Nanocrystalline light metal hydride particles from magnesium-nickel alloys are suitable for operating temperatures up to 300 °C, and $LaNi_5$ alloys for low temperature hydrogen storage up to 80 °C. Also, for carbon nanotube materials or alkali metal-doped graphite nanofibers, high hydrogen absorption capacities are reported, but were partly not reproducible.

1.5.4 Computing

The technologies in this area are at the forefront of nanotechnology's commercialisation. Nanotechnology has the potential for smaller and faster computers

with larger memories than current processes of making transistors and other components permit. These will reach their limits in miniaturisation within the next decade or two, creating the demand for new methods of manufacturing, nanotechnology being one of them. Techniques such as soft lithography and bottom-up approaches to forming nanoscale components by self-assembly could produce cheap and effective microscale circuits. Molecular electronics, with molecular switches and circuits only a few atoms wide, offers the possibility of using molecular components in electronic devices, greatly reducing their size, although there are many practical issues to be addressed before this technique can be fully developed. However, new defect tolerant architectures for computing make highly integrated molecular electronics a possibility.

Numerous organic and inorganic materials have already been analysed for non-volatile memory applications. Organic memories offer the potential of simple integration and simple cell concepts with very small cell sizes. In comparison to inorganic materials, the properties of the organic memory layers can be tailored by a selective change of the molecular structure. Furthermore, organic materials are often suitable for vacuum deposition as well as for low-cost spin coating processes. Researchers described the cell concepts and requirements for non-volatile memories based on novel organic memory materials. Memory cells built with this technology have already shown promising reliability data. For the first time, retention data of more than a year are shown for an organic memory material exhibiting conductance switching. Further investigations show the potential for scaling the material down to feature sizes of less than 20nm. This organic storage material is an attractive candidate for non-volatile memories.

Intel has claimed to have produced fully functional 65 nm SRAM (Static Random Access Memory) chips using 12-inch (300mm) silicon wafers, which are expected to go into market this year (2005). The chips use a second generation version of Intel's strained silicon, copper interconnections, and low-k dielectrics. The 4Mbit SRAM cells are only .57μ^2 in size which means that 10 million chips could fit inside the tip of a ball point pen.

1.5.5 Lubricants

In mechanical systems much of the energy is required to overcome friction between surfaces. The use of nanoscale lubricants and high-precision surface engineering on a nanometer scale should substantially reduce the energy requirements. Reduction of the material content of products is a key issue for sustainability.

1.5.6 The design of lighter stronger materials

The design of lighter, stronger materials can also lead to savings in energy and raw materials, especially in the transport sector. Nanotechnology will impact on the industrial use of energy by reducing component size and thus using less resources and developing new materials that are cheaper to produce. Nanotechnology contributes to material design by altering the types of materials that can be produced.

1.5.7 Visual Displays

Visual displays can be made more efficient by using carbon nanotubes and band-gap engineering using nanostructured materials that optimise the emission spectrum of Light Emitting Diodes. Also nanolayered organic light emitting diodes (OLEDs) are now coming to the market.

1.5.8 Plastic and Colloids

Nanoparticles are highly effective catalysts, due to the increased surface area at such a small scale, and are being tested for use in plastics manufacturing to improve the properties and versatility of the resulting materials. Nanoparticles are also used in colloids, which in turn are being used in sunscreens, printer ink, and paints. Zinc and titanium oxide sunscreens, for instance, use nanoparticles that are so small they do not scatter light, leaving the end product clear instead of white.

1.5.9 Other applications

In the area of life sciences, for example, several start-ups are addressing the challenges posed by bioterrorism by developing sensors that use nanoparticles of CdSe QDs or Au

that are functionalized with strands of DNA. Others are exploring nanoparticles of iron metal or iron oxide as magnetic delivery systems for drugs. Security devices based on nanomaterials are also very fashionable. Nanophosphors made of rare-earth phosphates are being developed for security printing, and invisible nanorods of Au and Ag can be used as sophisticated bar codes. In the catalysis area, cerium dioxide (CeO_2) nanocrystals are being used as fuel additives for diesel engines, where they improve fuel efficiency and reduce emissions, while nanofoils of MoS_2 are of interest for hydrodesulfurization catalysis. Some of the applications for nanomaterials are more prosaic. For example, nanocrystals of Al react explosively with molybdenum trioxide (MoO_3) – the thermite reaction – and are available for military ordinance applications; they also oxidize very rapidly and are being developed for rocket fuels.

Other inorganic nanoparticles, especially clays, are being incorporated into polymer composites, where they confer better flame resistance, mechanical properties, or gas permeability. In the case of dental fillings, the use of rare earth-containing nanoparticles gives rise to better contrast in X-ray imaging. The fields of bio- and organic nanoparticles are also mushrooming. Block copolymers can self-assemble to form nanostructures that create excellent templates for laying down other materials.[99] Similarly, surfactants and lipids, which are well-known to form submicron-sized vesicles, can also be used as the basis for creating nanocapsules, which are of interest for targeting and delivery systems in pharmaceutical and personal care products. Encapsulation can also be achieved by using nanoemulsions, dendrimers,[100] or crosslinking micelles.[101]

Chapter 2

Synthesis of Cadmium and Lead Thiosemicarbazide complexes

2.1 General introduction

This chapter presents a detailed discussion, including the bonding status and the coordination of the metal thiosemicarbazide complexes synthesized and the related ones reported in the literature, in both the crystalline and non-crystalline form. The crystal structures of these complexes are reported in this section.

2.1.1 Cadmium Complexes

Cadmium(II) complexes have been extensively studied from a chemical and structural point of view, mainly due to the capability of cadmium(II) to adopt different modes of coordination (shared by most d^{10} metal ions) determined by consideration of size, as well as electrostatic and bonding forces.[49] Amongst these complexes are thiosemicarbazides, a class of metal complexes that have been shown to exhibit a wide range of biological activities, which is considered to be related to their ability to chelate metals.[50] Some complexes of thiosemicarbazide derivatives are potential anti-tumor and hypertensive agents and others are active against influenza, protozoa and small pox.[51]

A number of complexes of transition metals with thiosemicarbazide-based ligands have found extensive application in medicine, technology and analytical chemistry.[52] Interest in the crystal engineering of metal complexes has stimulated investigation of means of thiosemicarbazide-based metal complexes in supramolecular structures.[53] The relatively rigid structure of metal thiosemicarbazide chelate rings and the capacity of the ligand for hydrogen bonding make these molecules potentially important for stabilization of

supramolecular structures. In its complexes, thiosemicarbazide behaves as a chelating bidentate ligand coordinated through the terminal hydrazine N atom and S atom. Upon alkylation of the S atom, the manner of coordination of thiosemicarbazide changes, so that it coordinates through the thioamide N atom instead of S.[54,55]

Complexes of the d^{10} metal ions of mixed diimine and thiolate ligands have also been shown to exhibit an interesting type of intra-ligand charge transfer transition in the visible region without the involvement of the metal ion.[53] These kinds of non-linear optical (NLO) complexes are characterized with a central metal ion surrounded by a number of organic and/or inorganic ligands.[55,56] The organic ligand is usually more dominant in the NLO effect. Much focus has been on the IIB (Zn, Cd, Hg) group metal complexes, as these metals have a high transparency in the UV region because of their closed d^{10} shell. Half-filled metals with a d^5 electronic configuration is also good for such applications.[56]

This has stimulated research on the excited state electronic properties of thiolato-complexes of these metal ions. A comparison of the previously reported structures of Ni(II) and Cu(II) complexes with S-methylisothiosemicarbazide and the corresponding thiosemicarbazide analogues shows that in both types of compound, the geometry of the coordination polyhedron is similar.[52,57,58] In order to investigate the influence of a different coordination mode on the geometry of the coordination polyhedron in the absence of ligand field stabilization energy, and also the packing characteristics of the

corresponding compound, Novacović, *et al.*[52] determined the crystal structure of $[ZnCl(C_2H_7N_3S)_2]Cl$.

In spite of the frequent use of the thiosemicarbazides as ligands, mainly with transition metals, only six complexes of the thiosemicarbazide ligand have been fully identified by X-Ray diffraction: namely five adducts of cadmium with neutral thiosemicarbazide and halide ligands and the complex $[Cd(TSC)_2]$ (TSC^- = pyridine-2-carbaldehyde thiosemicarbazonate). The six compounds exhibit a surprising range of coordination numbers (4, 5, 6, 7) and coordination polyhedra (tetrahedral, trigonal bipyramidal, highly distorted octahedral and distorted trigonal bipyramidal pentagonal).[54,59,60] It could be expected that the design of the IIB metal complexes derived from thiosemicarbazones might be a possible way to obtain applicable non-linear optical materials.[50,54-56] This characteristic could be exploited by using these complexes, of course employing their bonding status (metal-chalcogen bond), to make a new class of materials with tunable properties through varying their sizes and shapes. These materials are embodied within the size of the nanometer range.

2.1.2 Lead Complexes

Lead(II) has a particular fascination for coordination chemists almost of all p-block elements, as it can adopt many different geometries in its complexes. This allows a degree of tolerance for ligand configurations, which is not seen in elements fromother

groups, particularly d-block elements. Lead is coupled with the ability to bind well to both hard and soft donor atoms, which makes it an interesting metal to study, forming complexes which are different from those which might be conventionally expected. This is in any case quite often for lead(II). Subsequent to its many applications in technology, the toxic nature of lead(II) and its widespread occurrence in the environment adds a focus to search for powerful and selective lead binding materials and ligand systems.[61]

With regard to the coordination and stereo-activity of the valence lone electron pairs, details of the coordination chemistry of lead(II) compounds are frequently discussed.[62] Recently, Shimoni-Livny, *et al.*[62,63] has recently discussed the possible stereo-chemical activity of the lone pair in divalent lead compounds, based on a thorough review of the crystal data available in the Cambridge structural database. They classify lead coordination as holodirected, which refers to complexes in which the bonds to ligands atoms are directed throughout the surface of the encompassing sphere, while hemidirected refers to those cases in which the bond to ligand atoms are directed throughout only part of the coordination sphere, leaving a gap in the distribution of bonds to the ligand.[62]

The latter, present in all Pb(II) compounds with coordination number 2-5, is quite common in Pb(II) compounds with coordination numbers 6, 7 and 8, but does not exist in lead complexes with higher coordination numbers (9 and 10), where holodirected geometry is the rule. For divalent lead, relatively few structures with high coordination

numbers (9 and 10) were identified and with these high coordination numbers, all Pb(II) compounds have holodirected geometry.[63-65] Extensive recent structural studies of lead(II) compounds in particular have provided a basis for rather detailed analysis of the evidence for coordination sphere distortions which may be a consequence of the presence of lone-electron pairs.[63] However, since the presence of the lone pair is not directly detected but recognized on the basis of the atoms assumed to be donors to the central ion, the identification of these donor atoms is fundamental to the analysis of any system.[65]

There is an increasing interest in the study of magnetic, electronic and optoelectronic properties of low-dimensional organic-inorganic hybrid compounds including lead compounds. Studies suggest that complex systems consisting of inorganic and organic components have great potential for the creation of functional materials utilizing the wide variety of properties associated with each component.[65-72] Hence the synthesis of low-dimensional organic inorganic hybrid compounds giving materials with novel physical properties is motivated by this notion. Consequently, quite a remarkable interest has been focused on lead containing materials developed for industrial applications, such as lead containing thin films and nanoparticles.[72-75] PbS is a particular case of such materials.

2.2 Experimental

2.2.1 Instrumentation

2.2.1.1 CHN elemental analysis

The elemental analyses of the samples were performed by the University of Manchester micro-analytical laboratory

2.2.1.2 Infrared spectroscopy

Infrared measurements were performed using a Perkin Elmer Paragon 1000 FT-IR spectrometer. The samples were measured as KBr pellets and as Nujol mulls.

2.2.1.3 Crystal data collection

The crystal data was collected using Bruker Smart Apex CCD Diffractometer. The low temperature apparatus used was Oxford Cryosystems 700 Series Cryostream Cooler, at 100 K as a collection temperature. Mo radiation was applied at the potential/current of 50 kV, 40 mA, over 0.3 degrees rotation per frame, and the exposure time per frame was 10 seconds. The crystal mounting was done using a drop of fomblin (perfluoropolymethylisopropyl ether) oil in a Hamilton Cryoloop. X-ray crystal structure analysis takes advantage of state-of-the-art diffractometer facilities. Computing and molecular graphics display is based on a suite of high performance Silicon Graphics computers and PCs and a wide range of software.

2.2.2 Synthesis of the metal complexes

2.2.2.1 Synthesis of non-crystalline $Cd(NH_2CSNHNH_2)_2Cl_2$

Cadmium chloride ($CdCl_2$), 2.1 g (10 mmol) was dissolved in 100 mL ethanol. A solution of thiosemicarbazide, 1.82 g (20 mmol), in 100 mL was added and the mixture was refluxed for ca. 8 h. The solution was allowed to evaporate to deposit white solid, which was filtered, washed with ethanol and dried. C, H, N, S analyses (%) *experimental: Found: C, 6.8; H, 2.5; N, 23.6, S, 17.2. Calculated: C, 6.6; H, 2.7; N,* 23.1; S, 17.6. Yield: 85 %. Significant IR bands (cm^{-1}): ν(N—H) 2355, 3167, 3448; ν(C—N) 1592; ν(N—N) 1380; ν(C=S) 1039; ν(Cd—Cl) 257; ν(Cd—S) 201.

2.2.2.2 Synthesis of crystalline complex A, $[Cd(NH_2CSNHNH_2)Cl_2]_n$

Cadmium chloride (1.1 g, 6 mmol) and thiosemicarbazide (1.1 g, 12 mmol) were each dissolved in hot ethanol 50 mL in a 1:2 mole ratio, and mixed. A white precipitate (formed on mixing two solutions) was collected and re-dissolved in hot methanol (100 ml). The solution was quickly filtered through suction whilst hot, which enhances the fast cooling rate. The supernatant was formed a cream white precipitate, which was re-crystallised in 100 ml of water, and left for about 2 days to crystallise. Cream white prismatic crystals of $[Cd(NH_2CSNHNH_2)Cl_2]_n$ (1.5 g, 85 %) were obtained by re-crystallisation from hot water. Micro Analysis: Expected: C, 4.11; H, 1.72; N, 14.37. Found: C,4.32; H, 2.35; N, 14.37.

Significant IR bands (cm^{-1}): ν(N—H) 2347, 3165, 3441; ν(C—N) 1589; ν(N—N) 1371; ν(C=S) 1049; ν(Cd—Cl) 250; ν(Cd—S) 198.

2.2.2.3 Synthesis of crystalline complex B, $[Cd(NH_2CSNHNH_2)_2Cl_2]_n$

Cadmium chloride ($CdCl_2$) (2.5 g, 13 mmol) and thiosemicarbazide (2.5 g, 26 mmol) were each dissolved in 70 mL ethanol. Here, the white precipitate formed was re-dissolved in hot methanol (100 mL), and left to cool slowly at room temperature. The cream white flakes were obtained and re-crystallised in hot water (100 ml). The mixture of light brown flat crystals and of different shapes, and some cream white prismatic crystals (showed to be complex A) were obtained after *ca.* 3 days. The crystals filtered through, and light brown flat crystals of $[Cd(NH_2CSNHNH2)_2Cl_2]_n$ (3.1 g) were taken for analysis.

Micro: Expected: C 6.3, H 2.2, N 21.9; Found, C 6.17, H 2.21, N 21.0 Yield: 62 %

Significant IR bands (cm^{-1}): ν(N—H) 2355, 3167, 3448; ν(C—N) 1592; ν(N—N) 1380; ν(C=S) 1039; ν(Cd—Cl) 257; ν(Cd—S) 201.

2.2.2.4 Synthesis of $[Pb(NH_2CSNHNH_2)(NO_3)_2]$

Lead nitrate was reacted with thiosemicarbazide in a 1:2 (10 mmol) ratio, 1 g of $NH_2CSNHNH_2$ and 1.53 g of $Pb(NO_3)_2$, each dissolved separately in hot water (200 mL) before mixing. The solution turned clear brown in color, which was left open for evaporation. After two days, brown crystals of the complex were collected, filtered and taken for analysed. Yield: 1.10 g (86 %) Found: C, 2.51; H, 1.73, N, 16.45. Calculated: C, 2.84; H, 1.20; N; 16.58. Significant IR bands (cm^{-1}): ν(N—H) 2040, 3033; ν(C—N) 1590; ν(C=S) 1010; ν(Pb—S) 735; ν(Pb—N) 1385.

2.3 Results and Discussions

One of the new methods for synthesis of metal sulfides is based on decomposition (or combustion) of single-molecular precursors with sulfur-containing organic ligands coordinated with formation of metal sulfur bonds.[76] It therefore remains to be of great interest to use pure and crystalline precursor complexes and to investigate the structure of the complexes by X-ray diffraction analysis. However, in the case of metal thiosemicarbazide complexes with cadmium, crystallinity was not as easy to achieve since the final crystals formed were polymeric. The crystals were not as good for the X-ray diffraction, which made it a little difficult to pick a crystal and this can be attributed to the semi-crystallinity of the crystals.

The most common state of molecular order in polymers is the crystalline state, with full three dimensional positional order. However, in contrast to the situation in elemental solids and small molecules, very few polymer systems can attain a state of complete crystallinity. Instead, almost all polymers are semi-crystalline, consisting of a composite of very small crystals in a matrix of much less ordered material. The reasons for this partial crystallinity are:

• **Slow kinetics**- Polymers are entangled, so it takes a long time for the molecules to arrange themselves in perfect crystals. Even quite modest cooling rates allow one to produce a glass.

• **Quenched disorder**- Polymers may have disorder built into the polymer chain. This can take the form of randomness in the sterochemistry or tacticity (polystyrene for

example is usually atactic and does not readily crystallise at all), or a random sequence of monomers in a random copolymer.

• **Branching**- If the polymer chains have many branches, this makes it more difficult to pack the chains into regular crystals. This is why low density polyethylene, which is branched, is less crystalline than high density polyethylene, which is strictly linear.[77]

2.3.1 Cadmium Complexes

2.3.1.1 $[Cd(NH_2CSNHNH_2)Cl_2]_n$ (A)

This complex is similar to the one reported by Woode, *et al.*[51] The thiosemicarbazide ligand bonds to Cd through S and N. The complex (Figure 2.1) is polymeric with the metal octahedrally coordinated to the ligand. There are three Cl atoms bonded to the Cd with one of them along with S forming a bridge with the adjacent Cd. The unit cell dimensions are: Monoclinic, *Cc*, a = 10.136(2) Å, 13.893(3) Å, c = 6.8116(14) Å. There is a water molecule (excluded in the structure with H atoms) in the complex. However, this water molecule is of hydration and is not part of the coordination sphere, but is involved with it in five separate hydrogen bonds, acting as an acceptor from N(2) and N(3) in two adjacent thiosemicarbazide, as a single donor to one Cl atom and as shared donor to two other Cl.

There also is a weak hydrogen bond between the chains acting through the N(2)H(2A) group and the Cl(2) atom. Within the chains the bridging of the chloride is almost symmetrical (2.648(3) Å vs 2.629(3) Å) with a significantly shorter bond length than the apical Cl (Cd(1)—Cl(1) 2.648(3) Å *cf* Cd(1) —Cl(2) 2.511(2) Å). However, the sulfur

bridge shows a bias towards the cadmium ion to which the rest of the thiosemicarbazide molecule is attached (Cd(1)—S(1) 2.585(3) Å *cf* Cd'(1) —S(1) (S(1)—Cd(1)#1) 2.860(3) Å. This may be rationalised by considering the orientation of the atoms. The thiosemicarbazide ligand lies almost in the plane of the Cd(1) ion and therefore allows the possibility of electron delocalisation through the NH—C=S—Cd system. However, the adjacent cadmium ion lies orthogonal to the plane of the ligand resulting in an unfavourable orientation for orbital overlap. The polymeric complex has epical positions on Cd occupied by a Cl atom from the layer below and the S atom from the layer above. Figure 2.2 shows the packing diagram of the crystal complex and its unit cell.

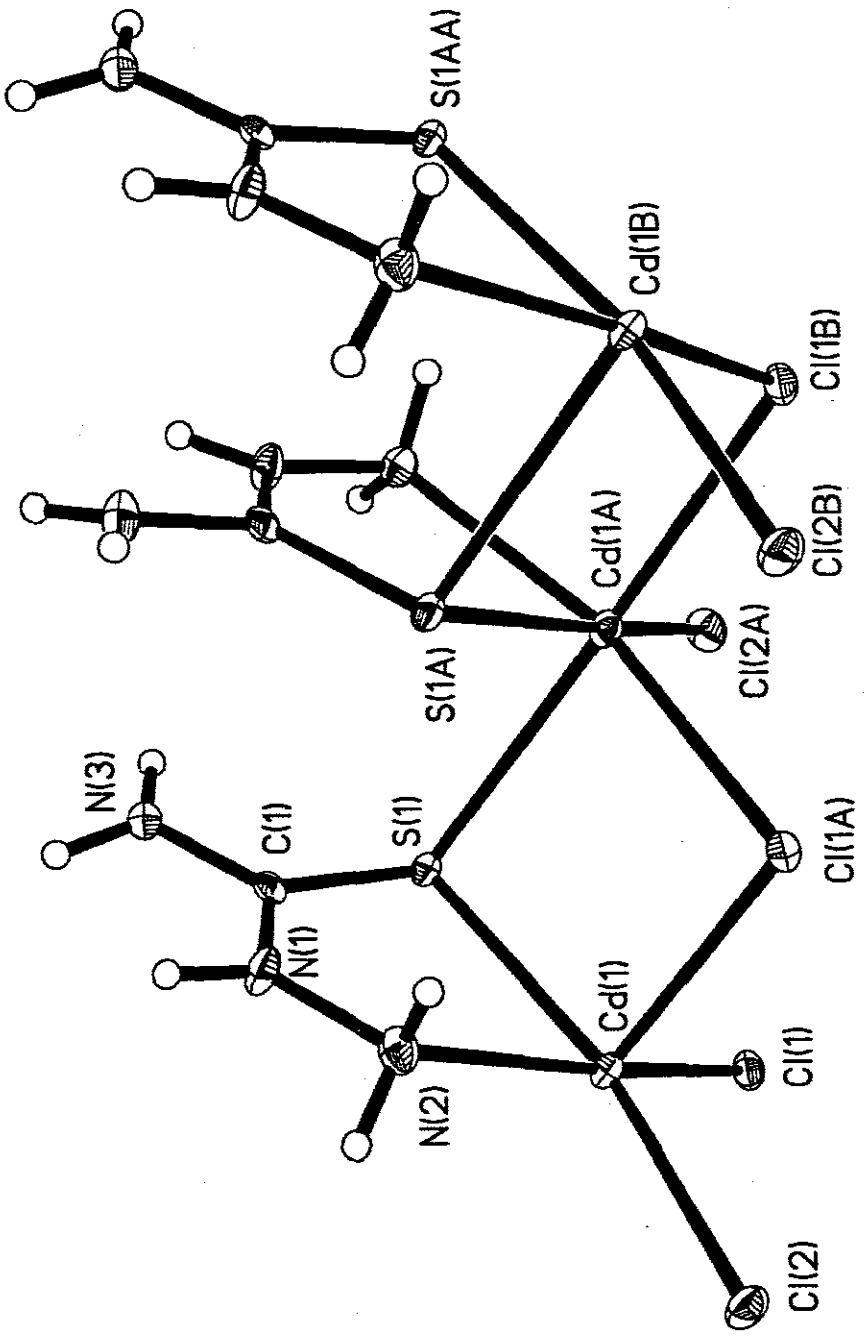

***Figure 2.1**: The single crystal X-Ray structure of $[Cd(NH_2CSNHNH_2)Cl_2]_n$*

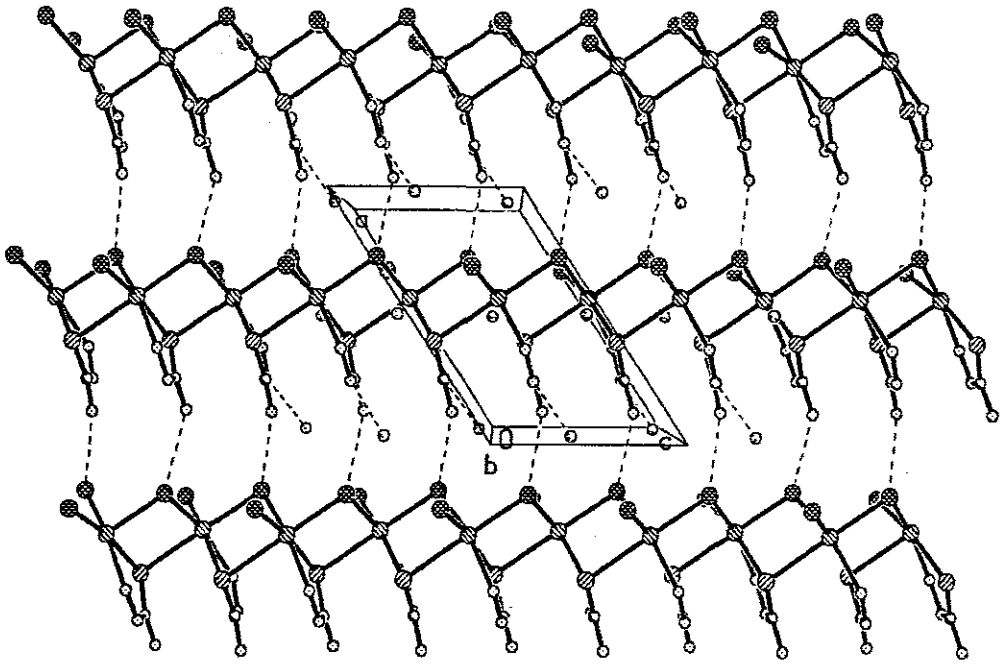

***Figure 2.2**: The packing of the $[Cd(NH_2CSNHNH_2)_2Cl]_n$ complex and its unit cell.*

The water molecule stabilizes the crystal structure; however, by participation in five separate hydrogen bonds. It acts as an acceptor in a hydrogen bond from N(2) in the parent ligand, and from N(3) of an adjacent thiosemicarbazide. One of the H atoms of the water participates in a single donor bond to Cl(1) and Cl(2) of two other neighbors. The crystal data for this complex is shown below.

Table 1: Crystal data and structure refinement for $[Cd(NH_2CSNHNH_2)Cl_2]_n$

Identification code	S2081abs
Empirical Formula	C H7 Cd Cl2 N3 O S
Formula weight	292.46
Temperature	100(2) K
Wavelength	0.71073 A
Crystal system, space group	Monoclinic, Cc
Unit cell dimensions	a = 10.136(2) A alpha = 90 deg.
	b = 13.893(3) A beta = 124.655(3) deg.
	c = 6.8116(14) A gamma = 90 deg.
Volume	789.1(3) A^3
Z, calculated density	4, 2.462 Mg/m^3
Absorption coefficient	3.637 mm^{-1}
F(000)	560
Crystal size	0.20 x 0.20 x 0.10 mm
Theta range for data collection	2.85 to 26.34 deg.
Limiting indices	-11<=h<=12, -17<=k<=15, -8<=l<=6
Reflections collected / unique	2229 / 1118, [R(int) = 0.0267]
Completeness to theta=26.34	99.1 %
Absorption correction	Semi-empirical from equivalents
Max. and min. transmission	0.7124 and 0.5299
Refinement method	Full-matrix least-squares on F^2
Data / restrains / parameters	1118 / 7 / 104
Goodness-of-fit on F^2	1.095
Final R indices [I>2sigma(I)]	R1 = 0.0417, WR2 = 0.1163
R indices (all data)	R1 = 0.0420, WR2 = 0.1167
Absolute structure parameter	0.14(6)
Largest diff. peak and hole	2.172 and -1.328 $e.A^{-3}$

Table 2: Atomic coordinates (x 10^4) and equivalent isotropic parameters (A^2 x 10^3). U (eq) is defined as one third of the trace of the orthogonalized U_{ij} sensor.

	x	y	z	U(eq)
Cd(1)	10832(1)	9362(1)	10259(1)	10(1)
S(1)	8976(4)	10666(2)	10158(6)	9(1)
Cl(1)	12547(4)	10704(2)	9979(6)	12(1)
Cl(2)	12100(3)	7881(2)	9899(4)	14(1)
N(1)	7301(9)	9010(6)	9183(14)	13(1)
N(2)	8675(9)	8458(5)	9889(14)	14(1)
N(3)	5965(10)	10423(6)	8599(15)	14(1)
C(1)	7372(10)	9969(6)	9278(14)	11(2)
O(1)	5102(8)	7814(4)	9293(15)	17(1)

Table 3: Bond lengths [A] and angles [deg] for $[Cd(NH_2CSNHNH_2)Cl_2]_n$

Cd(1)—N(2)	2.407(8)
Cd(1)—Cl(2)	2.511(2)
Cd(1)—S(1)	2.585(3)
Cd(1)—Cl(1)	2.629(3)
Cd(1)—Cl(1) #1	2.648(3)
Cd(1)—S(1) #2	2.860(3)
S(1) —Cd(1)	1.718(9)
S(1)—Cd(1) #1	2.860(3)
C1(1)—Cd(1) #2	2.648(3)
N(1)—C(1)	1.333(12)
N(1)—N(2)	1.413(10)
N(1)—H(1)	0.87(2)
N(2)—H(2A)	0.87(2)
N(2)—H(2B)	0.87(2)
N(3)—C(1)	1.338(12)
N(3)—H(3A)	0.87(2)
N(3)—H(3B)	0.86(2)
O(1)—H(10)	0.88(13)
O(1)—H(20)	0.83(13)
N(2)—Cd(1)—Cl(2)	92.71(19)
N(2)—Cd(1)—S(1)	76.03(18)
Cl(2)—Cd(1)—S(1)	167.73(7)
N(2)—Cd(1)—Cl(1)	163.94(16)
Cl(2)—Cd(1)—Cl(1)	100.27(8)
S(1)—Cd(1)—Cl(1)	90.11(7)
N(2)—Cd(1)—Cl(1) #1	92.2(2)

Cl(2)—Cd(1)—Cl(1) #1	94.08(8)
S(1)—Cd(1)—Cl(1) #1	91.25(10)
Cl(1)—Cd(1)—Cl(1) #1	96.21(10)
N(2)—Cd(1)—S(1) #2	86.3(2)
Cl(2)—Cd(1)—S(1) #2	83.68(8)
S(1)—Cd(1)—S(1) #2	90.64(10)
Cl(1)—Cd(1)—S(1) #2	85.82(9)
Cl(1)#1—Cd(1)—S(1) #2	177.22(5)
C(1)—S(1)—Cd(1)	99.4(3)
C(1)—S(1)—Cd(1) #1	104.7(3)
Cd(1)—S(1)—Cd(1) #1	89.55(9)
Cd(1)—S(1)—Cd(1) #2	93.37(9)
C(1)—N(1)—N(2)	122.5(7)
C(1)—N(1)—H(1)	113(7)
N(2)—N(1)—H(1)	125(7)
N(1)—N(2)—Cd(1)	114.4(5)
N(1)—N(2)—H(2A)	100(8)
Cd(1)—N(2)—H(2A)	112(8)
N(1)—N(2)—H(2B)	104(8)
Cd(1)—N(2)—H(2B)	110(8)
H(2A)—N(2)—H(2B)	115(10)
C(1)—N(3)—H(3A)	119(9)
C(1)—N(3)—H(3B)	118(7)
H(3A)—N(3)—H(3B)	121(10)
N(1)—C(1)—N(3)	117.8(7)
N(1)—C(1)—S(1)	124.6(6)
N(3)—C(1)—S(1)	117.6(7)
H(10)—O(1)—H(20)	153(10)

Symmetry transformations used to generate equivalent atoms: #1 x, -y+2, z+1/2
#2 x, -y+2, z-1/2

Table 4: Anisotropic displacement parameters ($A^2 \times 10^3$). The anisotropic displacement factor exponent takes the form $-2\,pi^2\,[h^2\,a^{*2}\,U11 + \ldots\ldots + h\;\; k\,a^*\,b^*\,U12]$

	U11	U22	U33	U23	U13	U12
Cd(1)	8(1)	11(1)	12(1)	0(1)	7(1)	2(1)
S(1)	8(1)	11(1)	11(2)	0(1)	6(1)	0(1)
Cl(1)	9(1)	16(1)	10(1)	1(1)	4(1)	0(1)
Cl(2)	14(1)	14(1)	15(1)	1(1)	8(1)	6(1)
N(1)	8(3)	12(3)	20(4)	2(3)	8(3)	2(3)
N(2)	12(3)	15(3)	15(4)	0(3)	7(3)	-3(3)
N(3)	9(3)	18(3)	14(4)	-5(3)	6(3)	-1(3)
C(1)	8(3)	19(4)	5(3)	-1(3)	2(3)	0(3)
O(1)	13(3)	18(3)	17(3)	2(2)	7(3)	-1(2)

Table 5: Hydrogen coordinates (x 10^4) and anisotropic displacement parameters (A^2 x 10^3).

	x	y	z	U(eq)
H(1)	6360(60)	8770(70)	8620(180)	10(20)
H(2A)	8250(130)	8050(60)	8720(130)	21
H(2B)	8980(140)	8220(80)	11270(100)	21
H(3A)	5980(160)	11040(20)	8800(200)	22
H(3B)	5070(70)	101110(70)	7700(190)	22
H(10)	5620(160)	7630(90)	10800(200)	26
H(20)	4820(140)	7740(90)	7900(200)	26

Table 6: Hydrogen bonds for $[Cd(NH_2CSNHNH_2)Cl_2]_n$ [A and deg.]

D-H...A	d(D-H)	D(H...A)	d(D...A)	<(DHA)
O(1)—H(20)...Cl(2) #3	0.83(13)	2.37(12)	3.047(11)	139(11)
O(1)—H(10)...Cl(2) #4	0.88(13)	2.41(14)	3.289(8)	178(11)
N(3)—H(3B)...Cl(1) #5	0.86(2)	2.43(2)	3.289(9)	176(11)
N(3)—H(3A)...Cl(2) #6	0.87(2)	2.73(5)	3.552(8)	160(11)
N(2)—H(2B)...O(1) #7	0.87(2)	2.22(5)	3.047(11)	158(11)
N(2)—H(2A)...Cl(2) #3	0.87(2)	2.52(3)	3.375(8)	169(10)
N(1)—H(1)...O(1)	0.87(2)	2.07(6)	2.815(10)	144(9)

Symmetry transformation used to generate equivalent atoms: #1 x, -y+2, z+1/2 #2 x, -y+2, z-1/2 #3 x-1/2,-y+3/2,z-1/2 #4 x-1/2,-y+3/2,z+1/2 #5 x-1,-y+2,z-1/2 #6 x-1/2,y+1/2,z #7 x+1/2,-y+3/2,z+1/2

2.3.1.2 $[Cd(NH_2CSNHNH_2)_2Cl_2]_n$ (B)

In this complex, Cd is coordinated to two thiosemicarbazide ligands. Each ligand bonds through S and N. The Cd(1)—S(1) bond length for complex A is 2.585 Å shorter than that for the Cd (1)—S(1), 2.735 Å for complex (B); the Cd(1)—N(5) bond length, 2.407 Å in complex (A) is slightly longer than the corresponding Cd(2)—N(5) bond, 2.343 Å, in complex B. The space group for the crystal system is monoclinic *C2/c*, and the unit cell dimensions are: a = 16.103(6) Å, $\alpha = 90°$; b = 8.074(3) Å, $\beta = 95.011(6)°$; c = 16.483(6), $\gamma = 90°$. The lattice consists of infinite chains of $CdCl_4$ units linked to CdL_2 units *via* a Cd—S—Cd bridge (L is thiosemicarbazide). The chloride ions lie almost symmetrically around the cadmium centre in the $CdCl_4$ moiety in a square planar geometry. The sulfur bridge is generated though a thiosemicarbazide ligand which lies fractionally closer to the $CdCl_4$ moiety then the CdL_2 (*cf* 2.735(1) Å vs 2.862(1)Å). This is probably a result of the thiosemicarbazide molecules tilted orientation toward the $CdCl_4$ moiety (N(1)—S(1)—Cd(1)) 86° *cf* 98° for Cd(2)). The CdL_2 units have the two thiosemicarbazide ligands lying in a square planar arrangement bound through both the sulfur and the nitrogen. This results in a considerably shorter Cd-S bond for the chelating ligand than for the bridging (Cd(2)—S(1) 2.862(1) Å *cf* Cd(2)—S(1) 2.589(1) Å). There are significant inter-chain and intra-chain bonding through NH—S and NH—Cl interactions (e.g. Cl(1)—N′(2), 3.400(3) Å; Cl(2)—N'(1), 3.234(3) Å; S(2)—N'(3), 3.582(3) Å; S(2)—N′(2), 3.395 Å). It is interesting to note the significance of the chelation of the thiosemicarbazide ligand on the length of the Cd—S bond. In both structures the chelate results in a Cd—S bond length of 2.585(3) Å whereas the non-

chelating results in a bond length of 2.860(3) Å. Figure 2.4 (a-c) shows the packing of the crystal and its unit cell from different view angles.

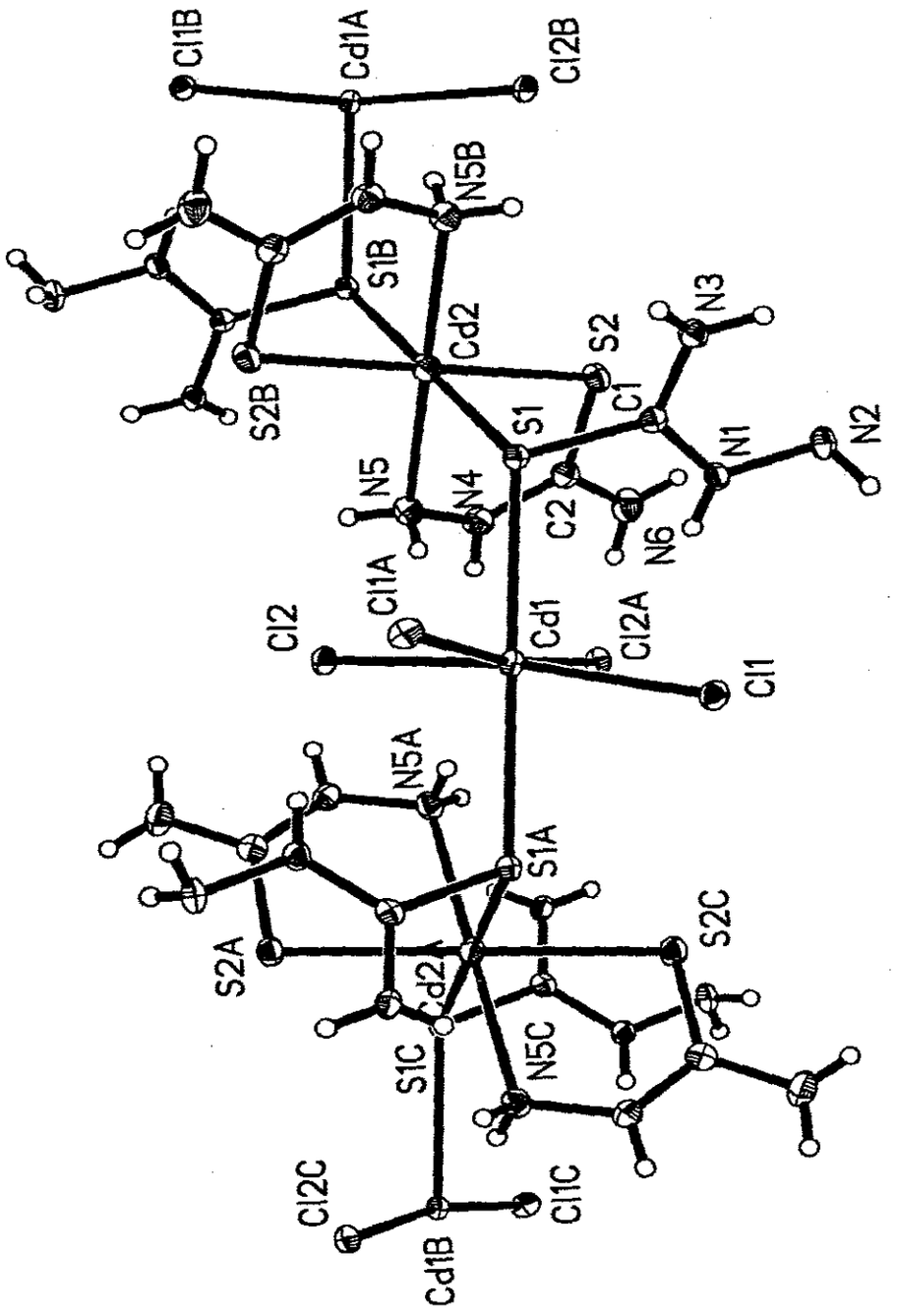

***Figure 2.3**: The single X-Ray crystal structure of $[Cd(NH_2CSNHNH_2)_2Cl_2]_n$*

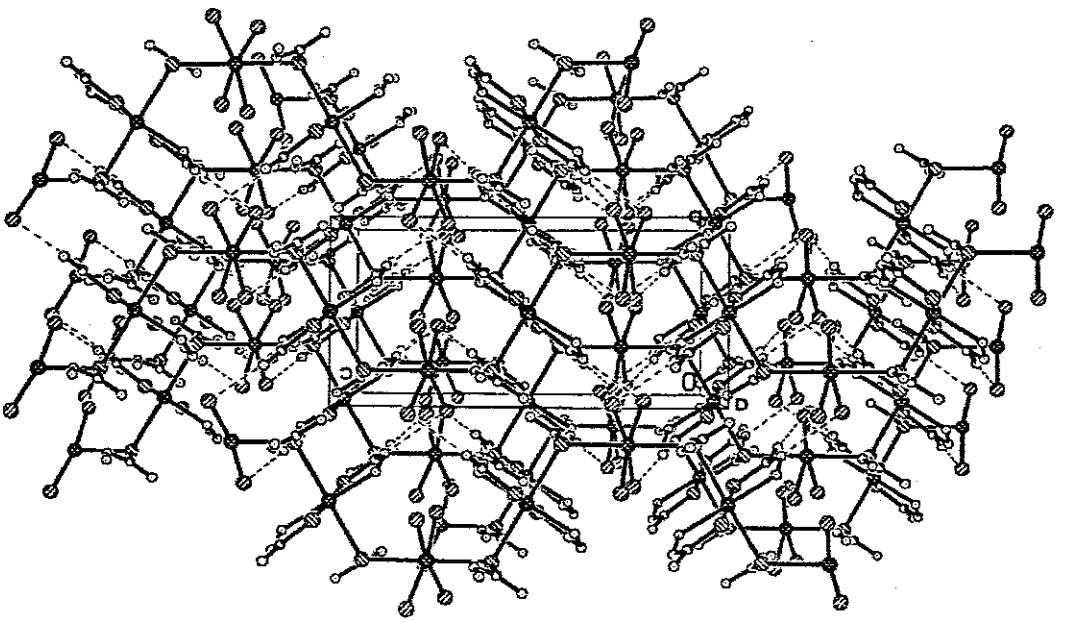

***Figure 2.4(a)**: The crystal structure's packing diagram of $[Cd(NH_2CSNHNH_2)_2Cl_2]_n$ and its unit cell (view angle a)*

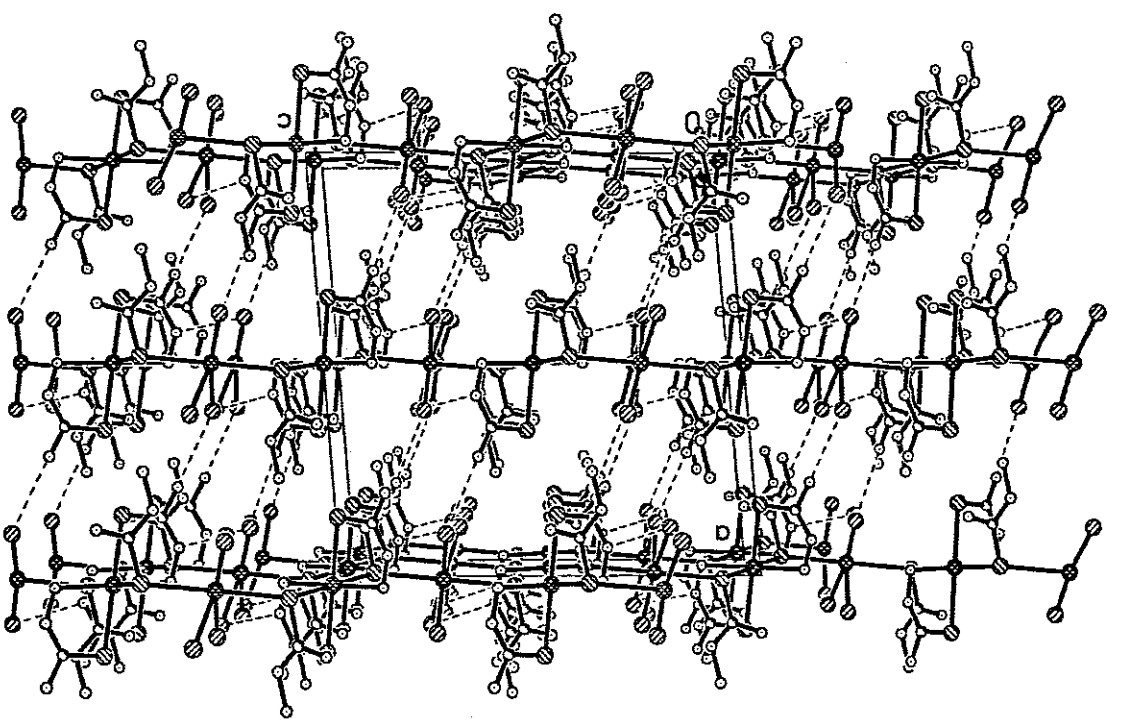

***Figure 2.4(b)**: The crystal structure's packing diagram of $[Cd(NH_2CSNHNH_2)_2Cl_2]_n$ and its unit cell (view angle b)*

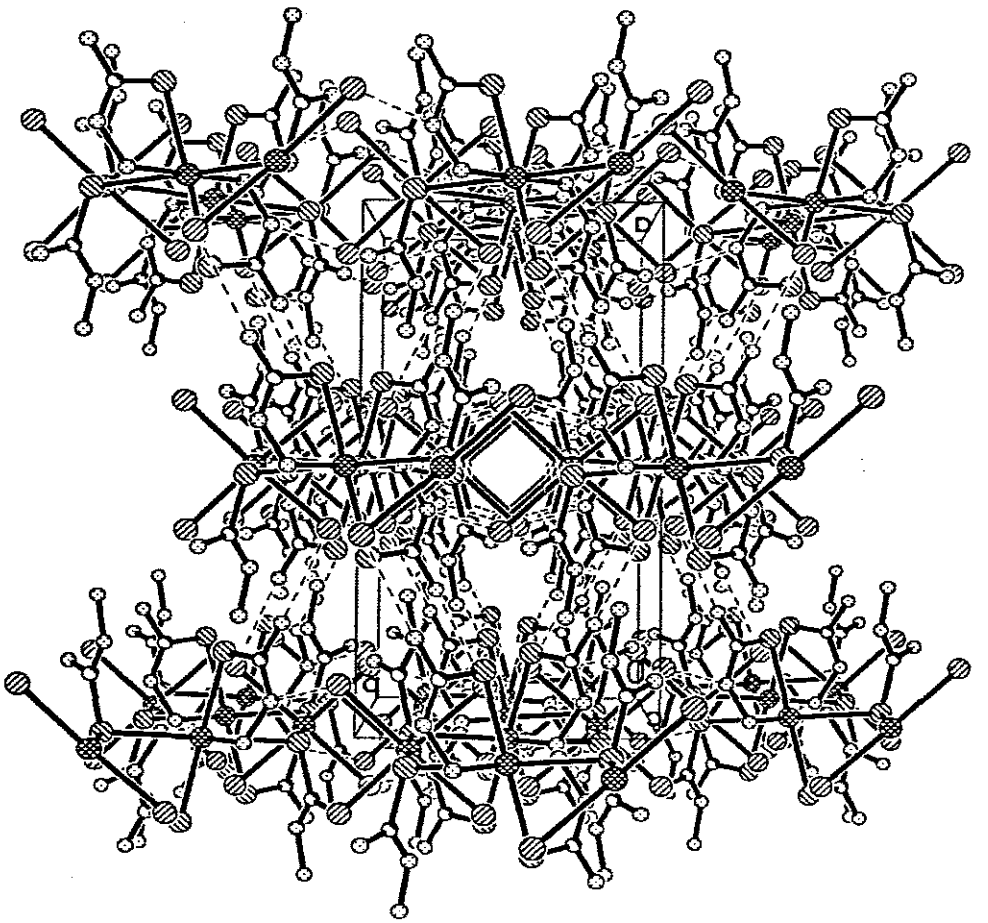

***Figure 2.4(c)**: Packing structure of $[Cd(NH_2CSNHNH_2)_2Cl_2]_n$ complex.*

The difference between the complex structure (A) and (B) could be attributed to the different conditions during the synthesis of the two. Complex B was obtained through slow cooling, whereas fast cooling was employed in A to achieve crystallization (Figure 2.5). Complex B crystals were too thin and unstable compared to A. This could be due to unfavorable energy from their fold surfaces, leading to smaller thermodynamic driving forces for the growth of the crystal. However, B forms over a much longer time, which could be attributed to the fact that this polymer is more entangled, so it takes a longer time for the molecules to arrange themselves in perfect

crystals. This (B) polymer chains have many branches, and this makes it more difficult to pack the chains into regular crystals.[77] This could also account for the complexity and branching of B compared to A. The crystal data for the complex B is presented below.

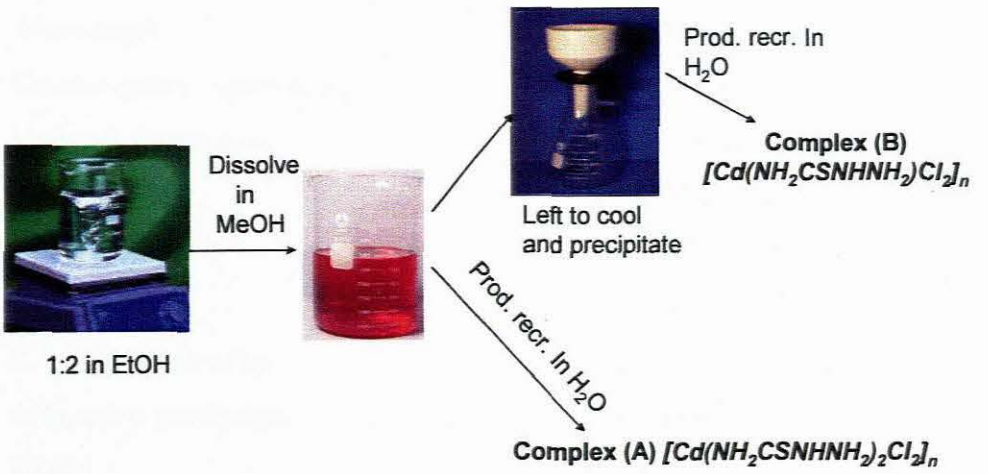

Figure 2.5: *Reaction route for the synthesis of complex (A) and complex (B)*

Table 1: Crystal data and structure refinement for $[Cd(NH_2CSNHNH_2)_2Cl_2]_n$

Identification code	S2089abs
Empirical Formula	C2 H10 Cd Cl2 N6 S2
Formula weight	365.58
Temperature	100(2) K
Wavelength	0.71073 A
Crystal system, space group	Monoclinic, C2/c
Unit cell dimensions	a = 16.103(6) A alpha = 90 deg.
	b = 8.074(3) A beta = 95.011(6) deg.
	c = 16.483(6) A gamma = 90 deg.
Volume	2134.9(14) A^3
Z, calculated density	8, 2.275 Mg/m^3
Absorption coefficient	2.903 mm^{-1}
F(000)	1424
Crystal size	0.20 x 0.20 x 0.20 mm
Theta range for data collection	2.48 to 26.39 deg.
Limiting indices	-19<=h<=20, -10<=k<=10, -20<=l<=20
Reflections collected / unique	8100 / 2187, [R(int) = 0.0239]
Completeness to theta=26.34	99.8%
Absorption correction	Semi-empirical from equivalents
Max. and min. transmission	0.5944 and 0.5944
Refinement method	Full-matrix least-squares on F^2
Data / restrains / parameters	2187 / 0 / 160
Goodness-of-fit on F^2	1.162
Final R indices [I>2sigma(I))]	R1 = 0.0206, WR2 = 0.0538
R indices (all data)	R1 = 0.0213, WR2 = 0.0544
Largest diff. peak and hole	0.726 and -0.729 $e.A^{-3}$

Table 2: Atomic coordinates (x 10^4) and equivalent isotropic parameters (A^2 x 10^3). U (eq) is defined as one third of the trace of the orthogonalized U_{ij} tensor.

	x	y	z	U(eq)
Cd(1)	0	8074(1)	2500	10(1)
Cd(2)	0	5000	0	17(1)
Cl(1)	1153(1)	10289(1)	2935(1)	14(1)
Cl(2)	-1128(1)	5727(1)	2307(1)	12(1)
S(1)	154(1)	8079(1)	860(1)	12(1)
S(2)	1564(1)	4264(1)	274(1)	16(1)
N(1)	1778(1)	7988(3)	1258(1)	13(1)
N(2)	2621(1)	8266(3)	1122(2)	15(2)
N(3)	1380(2)	9395(3)	87(1)	14(1)
N(4)	752(1)	2552(3)	1386(2)	16(1)
N(5)	6(1)	3430(3)	1196(1)	15(1)
N(6)	2145(2)	2254(3)	1449(2)	21(1)
C(1)	1184(2)	8540(3)	724(2)	11(1)
C(2)	1427(2)	2973(3)	1086(2)	14(1)

Table 3: Bond lengths [A] and angles [deg] for $[Cd(NH_2CSNHNH_2)_2Cl_2]_n$

Cd(1)—Cl(2)	2.6252(9)
Cd(1)—Cl(2) #1	2.6252(9)
Cd(1)—Cl(1)	2.6318(9)
Cd(1)—Cl(1) #1	2.6318(9)
Cd(1)—S(1) #1	2.7351(12)
Cd(1)—S(1)	2.7351(12)
Cd(2)—N(5) #2	2.343(2)
Cd(2)—N(5)	2.343(2)
Cd(2)—S(2) #2	2.5886(11)
Cd(2)—S(2)	2.5886(11)
Cd(2)—S(1)	2.8621(10)
Cd(2)—S(1) #2	2.8621(10)
S(1)—C(1)	1.735(3)
S(2)—C(2)	1.713(3)
N(1)—C(1)	1.319(3)
N(1)—N(2)	1.413(3)
N(1)—H(1)	0.82(4)
N(2)—H(2A)	0.78(4)
N(2)—H(2B)	0.88(4)
N(3)—C(1)	1.319(3)

N(3)—H(3A)	0.71(4)
N(3)—H(3B)	0.87(4)
N(4)—C(2)	1.343(4)
N(4)—N(5)	1.406(3)
N(4)—H(4)	0.79(3)
N(5)—H(5A)	0.90(4)
N(5)—H(5B)	0.84(4)
N(6)—C(2)	1.325(4)
N(6)—H(6A)	0.83(4)
N(6)—H(6B)	0.81(4)
Cl(2)—Cd(1)—Cl(2)#1	87.59(4)
Cl(2)—Cd(1)—Cl(1)	171.058(19)
Cl(2)#1—Cd(1)—Cl(1)	89.60(3)
Cl(2)—Cd(1)—Cl(1)#1	89.60(4)
Cl(2)#1—Cd(1)—Cl(1) #1	171.058(19)
Cl(1)—Cd(1)—Cl(1)#1	94.40(4)
Cl(2)—Cd(1)—S(1)#1	89.99(2)
Cl(2)#1—Cd(1)—S(1) #1	90.13(2)
Cl(1)—Cd(1)—S(1) #1	81.53(2)
Cl(1)#1—Cd(1)—S(1) #1	98.36(2)
Cl(2)—Cd(1)—S(1)	90.13(2)
Cl(2)#1—Cd(1)—S(1)	89.99(2)
Cl(1)—Cd(1)—S(1)	98.36(2)
Cl(1)#1—Cd(1)—S(1)	81.53(2)
S(1)#1—Cd(1)—S(1)	179.84(3)
N(5)#2—Cd(2)—N(5)	180.0
N(5)#2—Cd(2)—S(2)#2	78.24(6)
N(5)—Cd(2)—S(2)#2	101.76(6)
N(5)#2—Cd(2)—S(2)	101.76(6)
N(5)—Cd(2)—S(2)	78.24(6)
S(2)#2—Cd(2)—S(2)	180.0
N(5)#2—Cd(2)—S(1)	86.62(7)
N(5)—Cd(2)—S(1)	93.37(7)
S(2)#2—Cd(2)—S(1)	85.86(2)
S(2)—Cd(2)—S(1)	94.14(2)
N(5)#2—Cd(2)—S(1)#2	93.38(7)
N(5)—Cd(2)—S(1)#2	86.63(7)
S(2)#2—Cd(2)—S(1)#2	94.14(2)
S(2)—Cd(2)—S(1)#2	85.86(2)
S(1)—Cd(2)—S(1)	180.00(2)
C(1)—S(1)—Cd(1)	107.36(9)
C(1)—S(1)—Cd(2)	99.46(8)
Cd(1)—S(1)—Cd(2)	118.50(3)
C(2)—S(2)—Cd(2)	97.32(10)
C(1)—N(1)—N(2)	119.4(2)

C(1)—N(1)—H(1)	121(2)
N(2)—N(1) —H(1)	120(2)
N(1)—N(2)—H(2A)	108(3)
N(1)—N(2)—H(2B)	107(2)
C(1)—N(3)—H(3A)	111(3)
C(1)—N(3)—H(3B)	114(3)
H(3A)—N(3)—H(3B)	121(2)
C(2)—N(4)—N(5)	122(4)
C(2)—N(4)—H(4)	122.6(2)
N(5)—N(4)—H(4)	119(2)
N(4)—N(5)—Cd(2)	114(2)
N(4)—N(5)—H(5A)	113.62(16)
Cd(2)—N(5)—H(5A)	105(2)
N(4)—N(5)—H(5B)	113(2)
Cd(2)—N(5)—H(5B)	111(2)
H(5A)—N(5)—H(5B)	100(3)
C(2)—N(6)—H(6B)	114(3)
H(6A)—N(6)—H(6B)	114(2)
N(3)—C(1)—N(1)	120(2)
N(3)—C(1)—S(1)	125(3)
N(1)—C(1)—S(1)	119.1(2)
N(6)—C(2)—N(4)	115.0(3)
N(6)—C(2)—S(2)	119.8(2)
N(4)—C(2)—S(2)	125.2(2)

Symmetry transformations used to generate equivalent atoms: #1 x, -y+2, z+1/2
#2 x, -y+2, z-1/2

Table 4: Anisotropic displacement parameters (A^2 x 10^3). The anisotropic displacement factor exponent takes the form -2 pi^2 [h^2 a^{*2} U11 +..... + h k a* b* U12]

	U11	U22	U33	U23	U13	U12
Cd(1)	10(1)	9(1)	12(1)	0	0(1)	0
Cd(2)	12(1)	22(1)	17(1)	6(1)	1(1)	3(1)
Cl(1)	16(1)	13(1)	14(1)	1(1)	-1(1)	-4(1)
Cl(2)	11(1)	11(1)	15(1)	-2(1)	1(1)	-1(1)
S(1)	10(1)	14(1)	12(1)	1(1)	1(1)	0(1)
S(2)	12(1)	17(1)	19(1)	4(1)	2(1)	1(1)
N(1)	10(1)	15(1)	15(1)	3(1)	2(1)	-1(1)
N(2)	9(1)	14(1)	21(1)	0(1)	1(1)	1(1)
N(3)	10(1)	18(1)	15(1)	4(1)	1(1)	1(1)
N(4)	16(1)	15(1)	15(1)	3(1)	0(1)	2(1)
N(5)	14(1)	15(1)	17(1)	0(1)	3(1)	2(1)
N(6)	16(1)	21(1)	25(1)	5(1)	-2(1)	2(1)

C(1)	12(1)	9(1)	12(1)	-5(1)	2(1)	-1(1)
C(2)	16(1)	12(1)	15(1)	-2(1)	1(1)	-1(1)

Table 5: Hydrogen coordinates (x 10^4) and anisotropic displacement parameters (A^2 x 10^3).

	x	y	z	U(eq)
H(1)	1660(20)	7440(50)	1650(20)	21(9)
H(2A)	2840(20)	7410(50)	1120(20)	21(9)
H(2B)	2840(20)	8890(40)	1520(20)	21(8)
H(3A)	1040(20)	9800(40)	-130(20)	20(10)
H(3B)	1900(20)	9650(40)	20(20)	27(9)
H(4)	769(19)	2070(40)	1800(20)	10(8)
H(5A)	-400(20)	2650(50)	1180(20)	32(10)
H(5B)	-50(20)	4190(50)	1530(20)	25(9)
H(6A)	2070(20	1840(40)	1900(20)	17(8)
H(6B)	2590(20)	2370(40)	1270(20)	17(8)

Table 6: Hydrogen bonds [A and deg.] for $[Cd(NH_2CSNHNH_2)_2Cl_2]_n$

D—H...A	d(D—H)	D(H...A)	d(D...A)	<(DHA)
N(6)—H(6A)...Cl(1) #3	0.83(4)	2.67(4)	3.427(3)	153(3)
N(5)—H(5B)...Cl(2) #1	0.84(4)	2.86(4)	3.466(3)	131(3)
N(5)—H(5B)...Cl(2)	0.84(4)	2.56(4)	3.273(3)	143(3)
N(5)—H(5A)...Cl(1) #4	0.90(4)	2.75(3)	3.527(3)	145(3)
N(4)—H(4)...S(2) #3	0.79(3)	2.39(3)	3.160(3)	164(3)
N(3)—H(3B)...S(2) #5	0.87(4)	2.71(4)	3.582(3)	174(3)
N(3)—H(3A)...S(1) #6	0.71(4)	2.77(4)	3.467(3)	169(3)
N(2)—H(2B)...Cl(2) #7	0.88(4)	2.51(4)	3.337(3)	158(3)
N(2)—H(2A)...Cl(1) #8	0.78(4)	2.75(4)	3.400(3)	143(3)
N(1)—H(1)...Cl(2) #1	0.82(4)	2.42(4)	3.234(3)	173(3)

Symmetry transformation used to generate equivalent atoms: #1 –x,y,-z+1/2 #2 -x, -y+1,-z #3 x,y-1,z #4 -x,y-1,-z+1/2 #5 -x+1/2,-y+3/2,-z #6 -x,-y+2,-z #7 x+1/2,y+1/2,z #8 -x+1/2,y-1/2,-z+1/2

2.3.1.3 $[Pb(NH_2CSNHNH_2)(NO_3)_2]$

A novel single X-ray crystal structure, for the $Pb(NH_2CSNHNH_2)(NO_3)_2$ complex is reported (Figure 2.6). The lead thiosemicarbazide complex is four coordinate, tetrahedral. The bond angles O(5)#2—Pb(1)—O(2), 139.20(12) °; N(2)—Pb(1)—O(2), 77.32(14)° and N(2)—Pb(1)—S(1), 69.67(10)°, suggest, with reference to the literature,[62,64,65] that the coordination geometry around the lead atom is hemidirected, with the chelating thiosemicarbazide. The complex clearly shows that the lone pair of the Pb(II) atom is stereochemically active, which also accounts for the geometry, of the complex. As the formal oxidation state of lead is +2, the 6s orbital is populated by a pair of non-bonding electrons. The presence of the lone pair generally results in a non-spherical charge distribution around lead cations in solids, and furthermore, to a lowering of the symmetry of the coordination of the negative ions around them.[62-65]

The bond lengths Pb(1)—S(1), 2.7017 Å; Pb(1)—N(2), 2.551 Å; Pb(1)—O(5), 2.663(4) Å and Pb(1)—O(2), 2.700(4) are comparable with the ones reported for the related lead complexes in the literature.[62,64,65,78,79] It has been previously suggested that metal-ligand distances are shorter in lead complexes where the lone pair is stereochemically active.[62,64,65] The unit cell dimensions are: a = 5.2292 (5) Å, alpha = 75.3400(10) °; b = 7.1519(6) Å, beta = 88.8810(10) °; c =12.4064(11) Å, gamma = 79.6350(10) °. The space group of the crystal system is triclinic, P-1. Figure 2.7 shows the packing diagram of the crystal and its unit cell, showing the π-π stacking

interactions charge transfer arrays between the parallel thiosemicarbazide rings. The rest of the crystal data is shown at the end of this section.

A simple model to describe the nature of π–π interactions has been developed by Hunter et al.[62] This model predicts that face-to-face p-stacked interactions will be disfavored due to the dominance of π–π repulsion. However, in offset π-stacked, and edge-on or T-shaped geometries, favorable π-σ attractions dominate. The polarization of aromatic systems, through the introduction of heteroatoms, electron-withdrawing groups or electron-donating groups, alters the nature of any π–π interactions.[62,64,65]

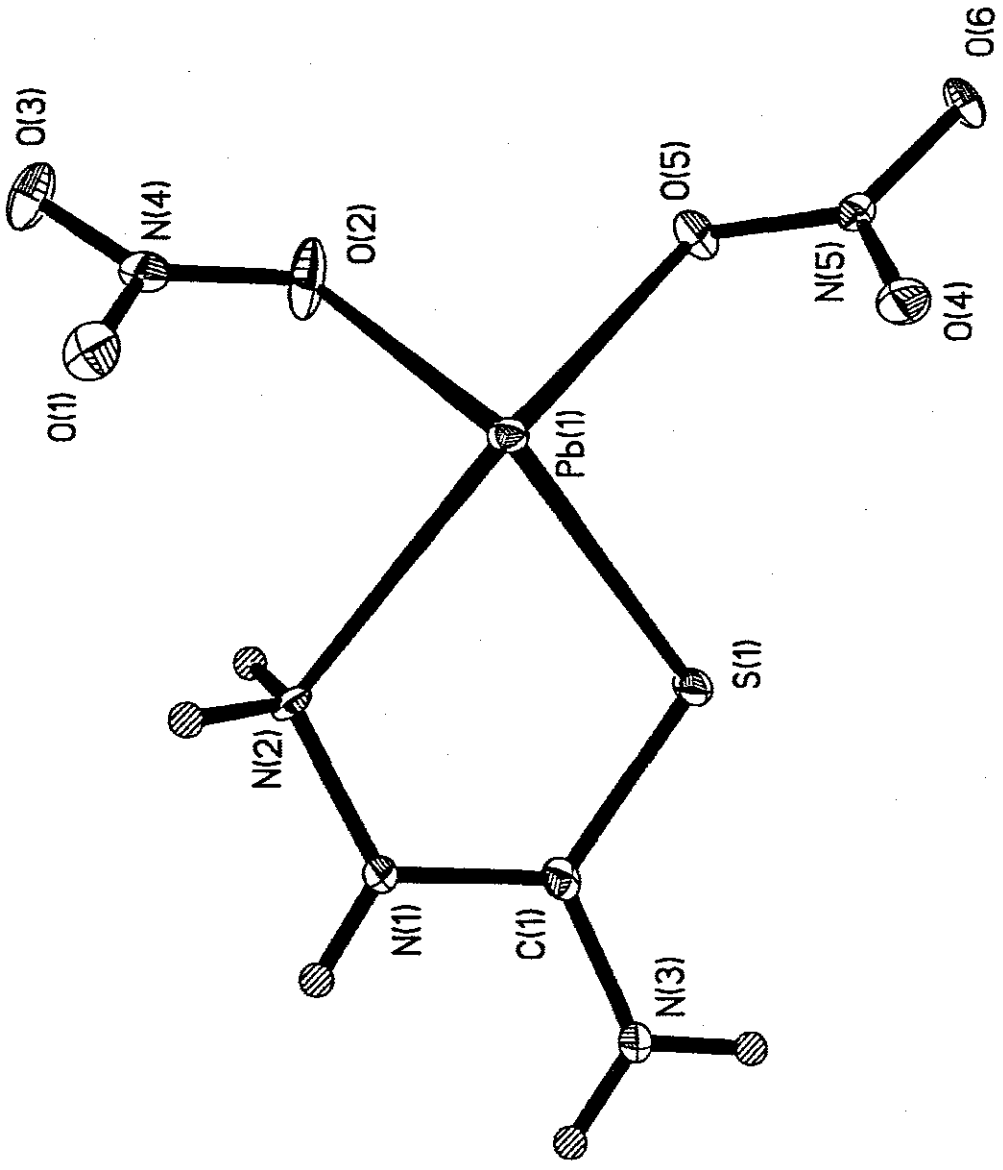

Figure 2.6: *The single crystal structure of* $[Pb(NH_2CSNHNH_2)(NO_3)_2]$

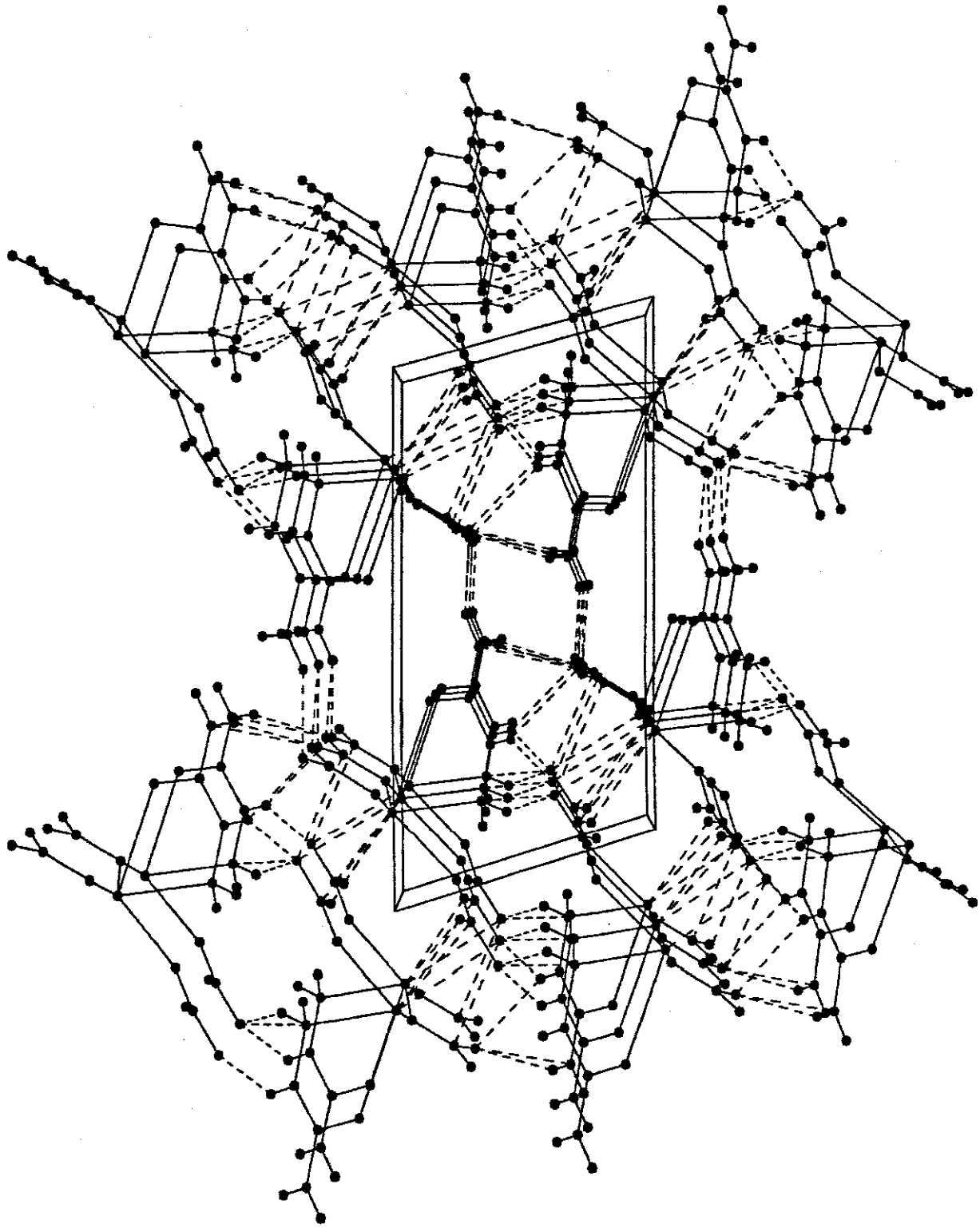

***Figure 2.7**: The crystal packing of [Pb($NH_2CSNHNH_2$)(NO_3)$_2$] and its unit cell*

Table 1: Crystal data and structure refinement for $[Pb(NH_2CSNHNH_2)(NO_3)_2]$

Identification code	S2092na
Empirical Formula	C H5 N5 O6 Pb S
Formula weight	422.35
Temperature	100(2) K
Wavelength	0.71073 A
Crystal system, space group	Triclinic, Cc
Unit cell dimensions	a = 5.2292(5) A alpha = 75.3400(10) deg. b = 7.1519(6) A beta = 124.655(3) deg. c = 12.4064(11) A gamma = 79.6350(10) deg.
Volume	441.39(7) A^3
Z, calculated density	2, 3.178 Mg/m^3
Absorption coefficient	19.366 mm^{-1}
F(000)	384
Crystal size	0.20 x 0.15 x 0.15 mm
Theta range for data collection	2.99 to 28.68 deg.
Limiting indices	-6<=h<=6, -9<=k<=9, -15<=l<=15
Reflections collected / unique	3832 / 2016, [R(int) = 0.0293]
Completeness to theta=26.34	92.6 %
Absorption correction	Semi-empirical from equivalents
Max. and min. transmission	0.1592 and 0.1128
Refinement method	Full-matrix least-squares on F^2
Data / restrains / parameters	2016 / 0 / 127
Goodness-of-fit on F^2	1.082
Final R indices [I>2sigma(I)]	R1 = 0.0238, WR2 = 0.0550
R indices (all data)	R1 = 0.0251, WR2 = 0.0555
Largest diff. peak and hole	1.023 and -1.730 $e.A^{-3}$

Table 2: Atomic coordinates (x 10^4) and equivalent isotropic parameters (A^2 x 10^3). U (eq) is defined as one third of the trace of the orthogonalized U_{ij} sensor.

	x	y	z	U(eq)
C(1)	10004(10)	2865(7)	3510(4)	9(1)
N(1)	10897(9)	3680(6)	2516(4)	10(1)
N(2)	9992(8)	3299(6)	1544(4)	8(1)
N(3)	1097(4)	3234(7)	4397(4)	11(1)
N(4)	6101(9)	2926(7)	-481(4)	12(1)
N(5)	3942(7)	-2075(6)	3115(4)	9(1)
O(1)	8521(7)	2468(6)	-465(3)	14(1)
O(2)	4882(8)	2417(7)	397(3)	22(1)
O(3)	4903(8)	3932(6)	-1360(6)	18(1)
O(4)	6152(7)	-2807(6)	3498(6)	14(1)
O(5)	3535(7)	-416(5)	2383(6)	12(1)
O(6)	2010(7)	-2899(6)	3414(3)	12(1)
Pb(1)	8510(1)	-4(1)	1870(1)	7(1)
S(1)	7635(3)	1435(2)	3685(1)	10(1)

Table 3: Bond lengths [A] and angles [deg] for $[Pb(NH_2CSNHNH_2)(NO_3)_2]$

C(1)—N(3)	1.324(7)
C(1)—N(1)	1.339(7)
C(1)—S(1)	1.720(5)
N(1)—N(2)	1.409(6)
N(1)—H(1)	0.8800
N(2)—Pb(1)	2.551(4)
N(2)—H(2A)	0.9200
N(2)—H(2B)	0.9200
N(3)—H(3A)	0.8800
N(3)—H(3B)	0.8800
N(4)—O(1)	1.248(6)
N(4)—O(3)	1.251(6)
N(4)—O(2)	1.258(6)
N(5)—O(4)	1.230(6)
N(5)—O(6)	1.263(6)
N(5)—O(5)	1.284(6)
O(2)—Pb(1)	2.700(4)
O(5)—Pb(1)#1	2.662(4)
O(5)—Pb(1)	2.716(4)
Pb(1)—O(5)#2	2.663(4)
Pb(1)—S(1)	2.7017(13)

N(3)—C(1)—N(1)	117.3(5)
N(3)—C(1)—S(1)	119.1(4)
N(1)—C(1)—S(1)	123.6(4)
C(1)—N(1)—N(2)	120.0(4)
C(1)—N(1)—H(1)	120.0
N(2)—N(1)—H(1)	120.0
N(1)—N(2)—Pb(1)	114.1(3)
N(1)—N(2)—H(2A)	108.7
Pb(1)—N(2)—H(2A)	108.7
N(1)—N(2)—H(2B)	108.7
Pb(1)—N(2)—H(2B)	108.7
H(2A)—N(2)—H(2B)	107.6
C(1)—N(3)—H(3A)	120.0
Cl(1)—N(3)—H(3B)	120.0
H(3A)—N(3)—H(3B)	120.0
O(1)—N(4)—O(3)	120.1(5)
O(1)—N(4)—O(2)	119.7(5)
O(3)—N(4)—O(2)	120.2(5)
O(4)—N(5)—O(6)	122.3(4)
O(4)—N(5)—O(5)	120.1(4)
O(6)—N(5)—O(5)	117.6(4)
N(4)—O(2)—Pb(1)	104.7(3)
N(5)—O(5)—Pb(1)#1	101.9(3)
N(5)—O(5)—Pb(1)	100.2(3)
Pb(1)#1—O(5)—Pb(1)	152.96(16)
N(2)—Pb(1)—O(5)#2	67.87(12)
N(2)—Pb(1)—O(2)	77.32(14)
O(5)#—Pb(1)—O(2)	139.20(12)
N(2)—Pb(1)—S(1)	69.67(10)
O(5)#2—Pb(1)—S(1)	85.64(9)
O(2)—Pb(1)—S(1)	101.99(10)
N(2)—Pb(1)—O(5)	122.05(120
O(5)#2—Pb(1)—O(5)	152.96(16)
O(2)—Pb(1)—O(5)	65.54(12)
S(1)—Pb(1)—O(5)	76.30(9)
C(1)—S(1)—Pb(1)	99.00(19)

Symmetry transformations used to generate equivalent atoms: #1 x, -y+2, z+1/2
#2 x, -y+2, z-1/2

Table 4: Anisotropic displacement parameters (A^2 x 10^3). The anisotropic displacement factor exponent takes the form -2 pi^2 [h^2 a^{*2} U11 +..... + h k a* b* U12]

	U11	U22	U33	U23	U13	U12
C(1)	10(2)	5(2)	11(3)	1(2)	-1(2)	-1(1)
N(1)	13(2)	11(2)	7(2)	-2(2)	1(2)	-6(2)
N(2)	8(2)	11(2)	5(2)	-3(2)	-2(2)	-1(2)
N(3)	16(2)	13(2)	7(2)	-1(2)	1(2)	-8(2)
N(4)	12(2)	11(2)	14(2)	-5(2)	0(2)	-3(2)
N(5)	11(2)	11(2)	7(2)	-3(2)	1(2)	-4(2)
O(1)	8(2)	21(2)	15(2)	-8(2)	3(2)	0(2)
O(2)	13(2)	32(2)	12(2)	5(2)	6(2)	0(2)
O(3)	18(2)	19(2)	8(2)	2(2)	-2(2)	5(2)
O(4)	12(2)	14(2)	14(2)	-2(2)	-4(2)	-3(2)
O(5)	11(2)	9(2)	16(2)	-1(2)	1(1)	-3(1)
O(6)	10(2)	13(2)	15(2)	-1(2)	5(2)	-8(2)
Pb(1)	6(1)	9(1)	7(1)	-3(1)	1(1)	-2(1)
S(1)	12(1)	14(1)	8(1)	-5(1)	4(1)	-8(1)

Table 5: Hydrogen coordinates (x 10^4) and anisotropic displacement parameters (A^2 x 10^3).

	x	y	z	U(eq)
H(1)	12048	4453	2468	12
H(2A)	11300	3339	1037	9
H(2B)	8623	4282	1236	9
H(3A)	12156	3989	4317	14
H(3B)	10436	2725	5065	14

Table 6: Torsion angles [deg.] for [$Pb(NH_2CSNHNH_2)(NO_3)_2$]

N(3)—C(1)—N(1)—N(2)	178.3(4)
S(1)—C(1)—N(1)—N(2)	-3.4(7)
C(1)—N(1)—N(2)—Pb(1)	-27.4(6)
O(1)—N(4)—O(2)—Pb(1)	-8.0(6)
O(3)—N(4)—O(2)—Pb(1)	173.9(4)
O(4)—N(5)—O(5)—Pb(1)#1	175.6(4)
O(6)—N(5)—O(5)—Pb(1)#1	-4.4(5)
O(4)—N(5)—O(5)—Pb(1)	11.3(5)
O(6)—N(5)—O(5)—Pb(1)	-168.7(4)
N(1)—N(2)—Pb(1)—O(5)#2	-62.2(3)
N(1)—N(2)—Pb(1)—O(2)	139.5(3)
N(1)—N(2)—Pb(1)—S(1)	31.4(3)

N(1)—N(2)—Pb(1)—O(5)	89.4(3)
N(4)—O(2)—Pb(1)—N(2)	66.1(3)
N(4)—O(2)—Pb(1)—O(5)#2	34.4(3)
N(4)—O(2)—Pb(1)—S(1)	131.7(3)
N(4)—O(2)—Pb(1)—O(5)	-159.5(4)
N(5)—O(5)—Pb(1)—N(2)	-140.1(3)
Pb(1)#1—O(5)—Pb(1)—N(2)	75.6(4)
N(5)—O(5)—Pb(1)—O(5)#2	-35.7(6)
Pb(1)#1—O(5)—Pb(1)—O(5)#2	180.0
N(5)—O(5)—Pb(1)—O(2)	164.6(3)
Pb(1)#1—O(5)—Pb(1)—O(2)	20.3(3)
N(5)—O(5)—Pb(1)—S(1)	-85.2(3)
Pb(1)#1—O(5)—Pb(1)—S(1)	130.5(3)
N(3)—C(1)—S(1)—Pb(1)	-153.6(4)
N(1)—C(1)—S(1)—Pb(1)	28.2(5)
N(2)—Pb(1)—S(1)—C(1)	-26.2(2)
O(5)#2—Pb(1)—S(1)—C(1)	41.77(19)
O(2)—Pb(1)—S(1)—C(1)	-97.7(2)
O(5)—Pb(1)—S(1)—C(1)	-158.5(2)

Symmetry transformations used to generate equivalent atoms: #1 x-1,y,z #2 x+1,y,z

Table 6: Hydrogen bonds [A and deg.]

D—H...A	d(D—H)	D(H...A)	d(D...A)	<(DHA)
N(1)—H(1)...O(3) #3	0.88	2.35	3.128(6)	146.9
N(1)—H(1)...O(6) #4	0.88	2.46	3.080(6)	127.5
N(2)—H(2A)...O(2) #2	0.92	2.08	3.948(6)	156.4
N(2)—H(2B)...O(3) #5	0.92	2.07	3.915(6)	151.5
N(3)—H(3A)...O(6) #4	0.88	2.21	3.870(6)	131.2
N(3)—H(3B)...Cl(2) #6	0.88	2.28	3.084(6)	152.6
N(3)—H(3B)...S(1)#7	0.88	2.99	2.538(6)	122.5

Symmetry transformation used to generate equivalent atoms: #1 x-1, y, z #2 x+1, y, z #3 -x+2, -y+1, -z #4 x+1, y+1, z #5 –x+1,-y+1,z #6 –x+1,-y,-z+1 #7 -x+2, -y,-z+1

2.4 Conclusions

The cadmium complexes crystallize in two forms A and B, which exhibit the distorted octahedral geometry, with the coordination number of six. The distortion of the coordination octahedron could be mainly caused by the relatively small bite of the bidentate thiosemicarbazide ligand and its rigid planar configuration which is almost perpendicular to the chain direction. Both complexes are polymeric, with the water molecule acting as a transverse intermolecular weak bridge between adjacent polymeric chains on the corresponding thiosemicarbazide. In all the complexes, the bonds, confirmed by the IR bands (experimental section) gave ν(C=S) 1010-1050cm^{-1} and ν(N—H) 2340-2360 cm^{-1} suggesting N,S-coordination. This renders the complexes perfectly suitable for the use as single-source precursors for metal chalcogenides. The lead complex was also found to be a suitable single-source precursor for the synthesis of PbS nanoparticles through its Pb—S bond, letting aside its poor results on shape-control (see later). It was found that there are two factors that principally control the coordination sphere of this complex, and thus the geometry of the entire complex, which are the lone pair activity and π-π stacking.

Chapter 3

Synthesis and shape control of CdS nanorods and PbS nanoparticles

3.1 Shape Control of Nanoparticles

3.1.1 General Introduction

The dependence of optical properties of semiconductor nanoparticles on their size and shape makes shape control fundamentally important.[80,81] This has led to shape control being the topic of substantial interest to nanomaterials chemists in the attempt to prepare nanomaterials of desired electronic properties for specific applications. Metal chalcogenides, such as CdSe, CdS and PbS remain materials of considerable interest in shape control thus far, due to their wide variation in one dimensional morphology which occur with changes in reaction conditions during synthesis. These materials also offer interesting properties for applications e.g. solar cells (CdS & CdSe) and near IR communications (PbS).

For a given solution system used in the synthesis of nanocrystals, one could get a variety of shapes e.g. dots, rice "grains", rods, or branched structures depending on the preferred growth regime within the system.[82,83] As the size of the nanoparticles decreases to a size comparable to the Bohr radius (Figure 1.2, page 5) around few nanometers, all bulk electronic properties start to change and, equally important, become dependent on size. At the nanoscale a semiconductor-nanoparticle transition occurs in which electrons are confined beyond their natural Bohr radius. The properties become dependent not only on size regime but also on shape of the nanocrystal. For example if an electron-hole pair (exciton) is formed in a sphere and in a place equal to or smaller than its natural separation, there is no room for exciton to move. This system

is referred to as a quantum 'dot' and as its exciton has zero degrees of freedom for its motion, in other words, the exciton is confined in all three dimensions (x, y, z) or a, b, c). If the particle is elongated, for example along the *c*-axis, the exciton formed will still be confined in the x and y direction (a and b) but can be transported along the z, exhibiting the rod-like structure. This suggests an exciton is confined in one in two directions, but can move in the third direction. If on the other hand the original sphere (dot) is compressed along the z-axis and equally extended in x and y (e.g. nanodisks), the exciton's motion is confined in one direction but has a room to move along x and y, i.e., in two dimensions and therefore referred to as 2D structures.[24,82,83]

In quantum dot structures, like CdS dots, some optical properties are the aspect ratio (length to breadth) dependence of the polarized emission and the ensemble Stokes shift (the shift between the first exciton absorption peak and the emission peak). Since a nanorods lie in the size regime that is between that of zero dimensional dots and one dimensional wires, the ability to finely control the degree of confinement (diameter and length) of the rods independently provides a unique system with which to study the shape-dependent properties. Because of the small dimensions (2-10 nm) of the rod diameter, there is still lateral confinement of carriers in the nanocrystal. The ability to control the length of the nanorods allows fine tuning of the degree of confinement along the c-axis.

In CdS the atoms are tetrahedrally bonded with alternating layers of Cd and S atoms stacked to yield wurtzite-like crystal structures. Since the nanocrystals are in a quantum

confinement regime, there is a very large dependence of the band gap on the size of the crystals. Excitation of an electron from the highest occupied electron state (which has high contribution from 3p atomic orbitals) to the lowest unoccupied electronic state (which has a high contribution from Cd 5s orbitals) results in the excited electronic structure of CdS. This theory could be linked with empirical pseudopotential calculations for spherical nanocrystals by Hu, *et al.*[84,85] for CdSe. According to these calculations, the electronic states with predominantly Se $4p_x$, $4p_y$ components have higher energy than that of states with mainly $4p_z$ components. The energy levels of all these increase with increasing size of the nanoparticle. When changing from spherical nanocrystals to nanorods, we are in fact changing the size of the nanocrystal along the *c*-axis, increasing the aspect ratio without changing its diameter. The aspect ratio only reduces confinement along the *c*-direction, as highlighted earlier on. The $4p_z$ orbital has greater momentum projection onto the c-axis of the nanocrystal than $4p_x$ and $4p_y$ orbitals have. Therefore the energy levels with more $4p_z$ components are much more sensitive to the rod length than others, and level crossing occurs. Pseudopotential calculations performed on this system as a function of the aspect ratio show that there is a crossover of the two highest occupied electronic states at an aspect ratio of *ca.* 1.5:1 around this band crossover, the energy levels with predominantly Se $4p_z$ components. The same could be assumed and applied to S $3p_{x, y, z}$ orbitals in the case of the CdS nanocrystals.[85]

3.1.2 Critical parameters for shape guiding process of nanocrystals

The final morphology of nanocrystals in any solution system for the synthesis is determined by the growth regime the reaction prefers, which in turn depends on the variation of critical parameters for the shape controlling process. The reaction can proceed in either the kinetic growth or thermodynamic growth control regime. After the determination of the preferred crystalline phase of the seed during the initial nucleation stage, the subsequent growth stage strongly governs the final architecture of the nanocrystals through a delicate balance between the kinetic growth and the thermodynamic growth regimes. The thermodynamic growth regime is driven by sufficient supply of thermal energy and low flux of monomers (low monomer concentration), yielding isotropic shaped, the most stable form of nanocrystals (e.g. cubes, spheres). In contrast under non-equilibrium, kinetic conditions with a relatively high flux of monomers, selective anisotropic growth (e.g. rod-like structures) between different crystallographic surfaces is facilitated.[82,83,85,86]

In general, there are four different parameters which influence the growth pattern of nanocrystals and hence their morphology (Figure 3.1): The intrinsic surface energy of the crystallographic face of the seed is important, since the kinetic energy barrier $\Delta G^{\ddagger}$ is inversely proportional to the surface energy of the crystal. These surface properties can be tailored by the types and the amounts of adsorbing organic capping molecules present (see later). The growth process should be quenched at appropriate times, since longer growth times can result in thermodynamically stable shapes of nanocrystals. The

molecular precursor which can decompose under mild conditions (e. g low temperatures) is critical for kinetic growth processes.[86]

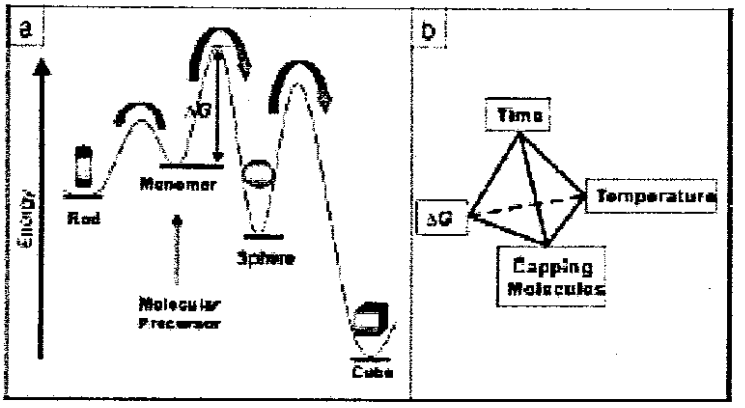

Figure 3.1: *(a) Schematic energy diagram for the formation of different nanocrystal morphologies. (b) Important parameters influencing growth and hence the morphology of the nanocrystals.*[89]

By using surfactants that bind differently to the crystallographic faces, one can control the shape of the nanocrystal.[88] At high temperatures (200-400 °C) the surfactant molecules are dynamically adsorbed to the surface of the growing crystal. The good surfactant molecules must be: mobile enough to provide access for the addition of the monomer units, while stable enough to prevent aggregation of the nanocrystals. The surface molecule must be stable at the high temperature required for the growth. The choice of surfactants varies from case to case: a molecule that binds too strongly to the surface of the crystal is not suitable, as it would not allow the crystal to grow. On the other hand, weakly coordinating molecule would yield large particles, or aggregates. At low temperatures, the surfactants are strongly bound to the surface of the nanocrystals

and provide appreciable solubility in organic solvents.[85,87,88] For example, HDA adsorbs selectively (with its amine) on the surface of the CdS favoring the formation of anisotropic morphology and appreciable solubility, compared with TOPO.[86]

Some examples of the good choice of surfactants include alkyl phosphines, phosphine oxides, phosphates, phosphonates, amides or amines, and nitrogen containing aromatics. In the case of mixed surfactant media used during the synthesis of the nanocrystals, ratios of surfactants (in case of surfactant mixtures) also affect the resulting phase and shape of nanocrystals. Another way to control branching might be to add surfactants during the growth, in order to change the energies of different faces relative to each other. In this way it would be possible to promote growth of zinc-blende CdSe phase by increasing the concentration of one surfactant. Another surfactant could then be added to bring the surfactant ratio back to conditions favoring rod growth to generate a new set of arms.[85]

Principally, the two conditions that influence whether a reaction undergoes kinetic or thermodynamic growth are the temperature of growth and the concentration of monomers. In the case of CdSe nanocrystals grown in a mixture of surfactants, conditions can be set to promote the formation of cubic (zinc blende) nuclei. Suppose now that, after this nucleation stage, one wants to control the phase in which the crystals will continue to grow, if we set conditions that still favour the cubic phase, then large spherical or tetrahedral nanocrystals will be obtained. One way of achieving this would be to keep the system at low temperature. On the other hand, if we want to

promote the hexagonal (wurtzite-like) growth, we have to keep the system in the high temperature kinetic regime, or we have to increase the concentration of monomers. In this situation, wurtzite-like rods (or arms) will form out of the (111) faces of the original zinc blende nucleus (Figure 3.2). [82-89]

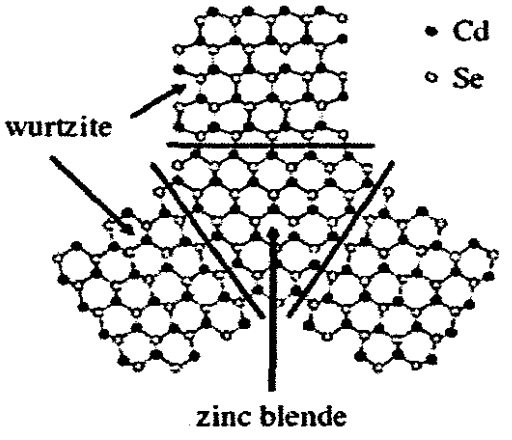

Figure 3.2: *A two dimensional presentation showing the structure of a tetrapod. The nucleus is zinc-blende with wurtzite arms growing out of each of the four (111)-equivalent faces.*[85]

Suppose now that, after the arms of the nanocrystal have reached a desired length, we want to re-enter the thermodynamic growth regime so that zinc-blende phase is favored again. This can be achieved by lowering the temperature, or by lowering the monomer concentration, or both, since any of these changes will push the system closer to equilibrium conditions. In this case, zinc blende tetrahedra will form on the ends of the wurtzite-like arms. We could yet again increase the concentration of monomers by means of an additional injection, or alternatively we could increase the temperature of the growth medium, again pushing the system into the kinetic growth regime: three new hexagonal CdSe arms will then grow out of the end of each previously existing arm

(forming "multipods"). In principle this process could be cycled to produce even more complex dendrimers.[82-89]

If the remaining monomer concentration in the growth solution is kept extremely high, the solution can supply a sufficient amount of monomers for each seed to fully grow arms on the four (111) facets of the zinc blende structure of the tetrahedral seed, which yields tetrapoles. A moderately high monomer concentration can only support the growth of a single arm in its 1D growth stage (Figure 3.3), which generates rod shaped nanocrystals. A median monomer concentration can only support those existing seeds in the 3D growths stage (see Figure 3.3), as a result, the nanocrystals are developed to the rice shape. The entire of those elongated nanocrystals are unable to co-exist with the low chemical potential environment at low monomer concentrations, as a result of the system generating only dots.[82,83]

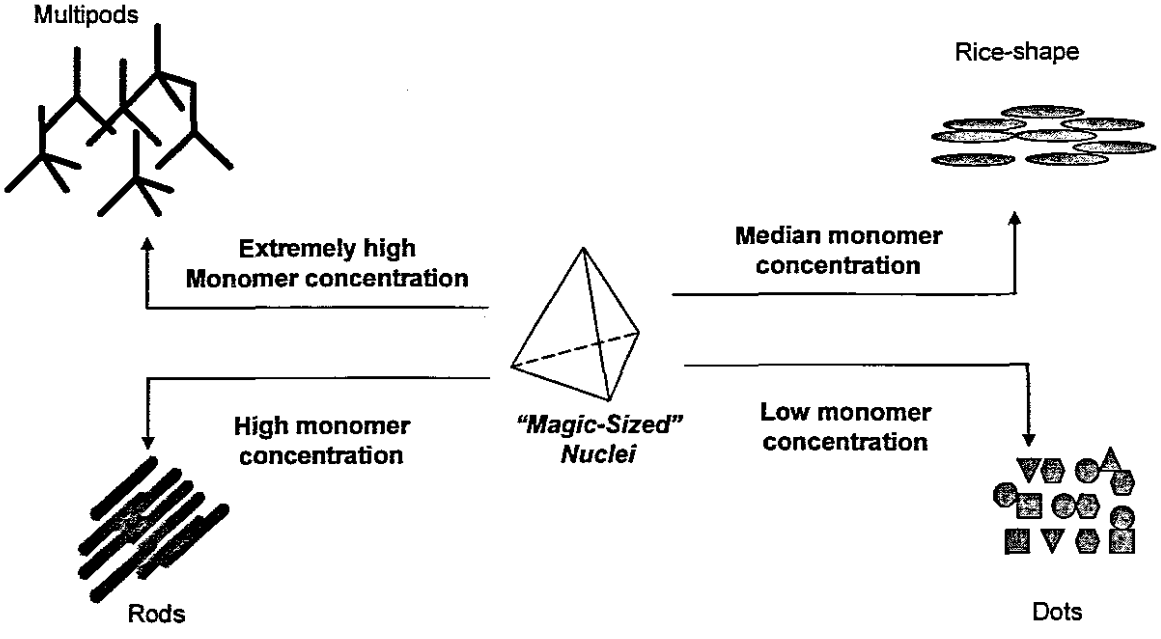

Figure 3.3: *Monomer – concentration dependent growth paths influencing the shape of the nanocrystals.*

The majority of synthetic reactions for the growth of elongated semiconductor nanocrystals in solution have been initiated by introducing certain amounts of monomers into the reaction systems. Consequently, the remaining concentration of monomers after nucleation process is reliant on the number of nuclei formed. In general, a relatively small number of nuclei are desirable for the growth of elongated nanocrystals because the change of the monomer concentration in the solution caused by the nucleation process and the subsequent growth process should be relatively small. Such conditions should result in a relatively stable monomer concentration in the solution and be suited for the growth of a given shape. Based on this principle, a relatively more stable precursor should promote the formation of nanocrystals with monodisperse size and shape.

3.1.3 Theoretical Aspects of Shape Control

The high monomer concentration impacts the formation of the nuclei as a consequence of the growth of rods in the 1D-growth mode or the 3D-growth mode. However, for further understanding of the relationship between the nucleation of the growth of shape controlled nanocrystals, necessary theoretical aspects should be understood. The Gibbs-Thompson equation is the basis of classic crystallization theory. Although it may not be regarded accurate enough for a quantitative description of a crystallization process in the nanometer regime, it should provide us with the starting point.

$$S_r = S_b \exp(2\sigma V_m / rRT) \qquad (2)$$

where r is the radius of the crystal, σ is the specific surface energy, V_m is the molar volume of the material, S_b and S_r are the solubility of bulk crystals and crystals with a radius r, R is the gas constant, and T is the absolute temperature.

The Gibbs-Thompson equation tells us that the solubility of a particular sized crystal is strongly dependent on its size. However, the solubility of a crystal with its size in nanometer regime is a relative term, since it is impossible to reach an ultimate chemical equilibrium between the nanocrystal and the monomers at the concentration of S_r determined from eq. 2. This is so because nanocrystals are thermodynamically mesostable species. Therefore, it should be more thermodynamically relevant to consider S_r determined from eq. 2 as being a measure of the chemical potential of nanocrystals. Therefore, the chemical meaning of the Gibbs-Thompson equation is that the chemical potential of a collection of nanocrystals with a given radius r is the same as that of the monomers at the concentration S_r. A simple mathematic treatment can change eq 2 to eq 3:

$$RT \ln S_r = RT \ln S_b + 2\sigma V_m / rRT \qquad (3)$$

If μr and μb, respectively, represent the chemical potentials of the crystals with a radius r and with an infinite size, eq 3 can be converted into eq 4:

$$\mu_r = \mu_b + 2\sigma V_m / rRT \qquad (4)$$

Here, we assume that crystals with different sizes share the same standard state.

For spherical crystals, the number of the surface atoms and the total atoms should be proportional to the surface area and the volume, respectively. If we define the surface atom ratio as δ, then

$$\delta = (k_1 4\pi r^2) / (k_2 4\pi r^3/3) = k_3 1/r \qquad (5)$$

and k_1, k_2, and k_3 are all proportional constants. Combining eqs 4 and 5 and setting the chemical potential of infinite sized crystals as the relative standard, the relative chemical potential of a crystal with a finite size should then be proportional to the surface atom ratio, δ.

$$\mu_r \propto \delta \qquad (6)$$

Equation 5 indicates that the relative chemical potential of crystals is simply proportional to their surface atom ratio. This is understandable from a structural point of view. The difference between bulk crystals with an infinite size and crystals with a finite size is the surface atoms, which possess some dangling bonds. The average dangling bonds per atom over the entire crystal will thus determine the relative chemical potential of the crystal. As a result, the relative chemical potential of the crystal with a finite size should be proportional to the surface atom ratio, if we assume each surface atom of the crystal possesses the same number of dangling bonds. Notice that this assumption is actually one of the basic assumptions of the Gibbs Thompson equation. It should be pointed out that the structural argument suggests that eq. 6 should be also applicable to crystals with different shapes. [82,83]

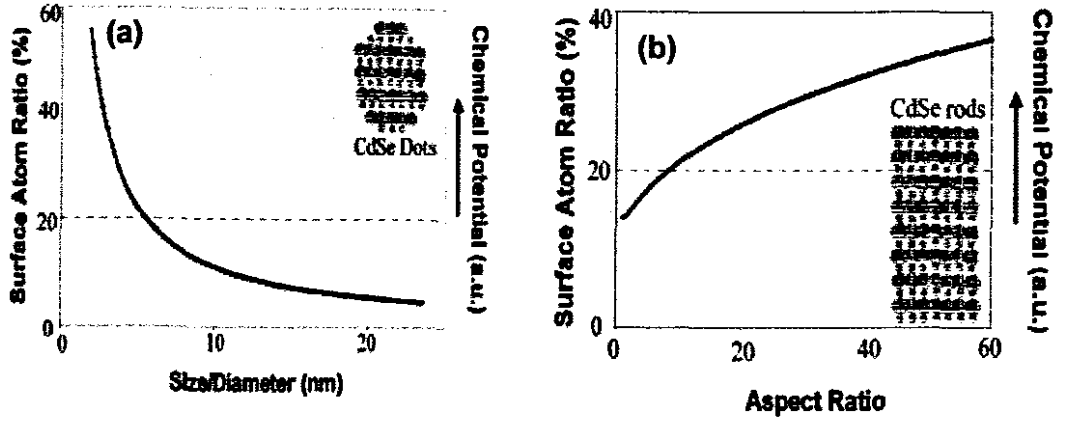

Figure 3.4:*(a) Size dependence of the size atom ratio and the relative chemical potential of CdSe nanocrystals, assuming a spherical shape.*[82,83]
(b) Shape dependent chemical potential of CdSe quantum rods. The volume of all nanocrystals is set to the same value of an 8 nm CdSe dot.[82,83]

For dot-shaped crystals, their relative chemical potential is plotted in Figure 3.4, (a), which indicates a very strong size-dependence of the relative chemical potential in the nanometer regime. The shape effect on the relative chemical potential of nanocrystals with different aspect ratios is plotted in Figure 3.4, (b). The volume of all the nanocrystals in Figure 3.4, (b), is set to the value of an 8 nm CdSe dot. The plot reveals the strong shape dependence of the relative chemical potential of crystals. For instance, the chemical potential doubled when the CdSe crystal is elongated from an 8 nm dot to a rod with its aspect ratio equal to about 30. The related solubility change would be much more pronounced, since the factor of 2 will apply to the exponential function (eq 2). [82,83]

However, there are two basic assumptions on which the theoretical treatment of this section, like the Gibbs-Thompson equation, is based, by Peng, *et al.*:[82,83,35]

- All surface atoms bear the same amount of surface free energy independent of the position of the atoms, and the size or the shape of the crystals, which is equivalent to the specific surface energy argument in eq 2.
- Secondly, the relative chemical potential discussed in this section is an average value over all the atoms in a crystal. A quantitative thermodynamic consideration of crystallization in nanometer regime based on the structural argument described above is in development, which aims to remove these two assumptions.

As far as 1D shape controlled synthesis is concerned, CdSe nanocrystals constitute the most extensively investigated II-VI semiconductors.[82] CdS is one of the II-VI semiconductors, but the independent theoretical and practical aspects of the 1D shape control of its nanocrystals have rarely been reported, and so CdSe has almost always been used as a model to further provide some insight for understanding the phenomenon of shape control for CdS nanocrystals. In this section, CdSe has been majorly used to clarify some and most of the theoretical aspects for the understanding of the CdS shape evolution at large.

3.1.4 Brief background to the current work

The use of the single source molecular precursor method is an efficient route to high quality nanoparticles. Various single source precursors for the preparation of respective nanoparticles have been developed and reported in the literature. O'Brien, *et al.*[93-95] first reported the use of these compounds, as a way to high quality nanoparticles whilst avoiding the need for volatile precursors and working under extremely harsh conditions. The single molecular approach provides both elements within a molecule, which allows the preparation of semiconductor nanocrystals in a one-step process by the thermal decomposition of the molecular precursor in a convenient dispersing medium.[91] This method makes use of various metal complexes such as dithio-/diseleno-carbamato complexes of cadmium/zinc containing asymmetrical alkyl groups. These precursors are non-air sensitive, stable for a period of months, easy to synthesize and most of all pyrolyse cleanly to give the highest yield. Revaprasadu, *et al.*[45] and Malik, *et al.* [93] reported the use of the single source precursor method in preparing the nanoparticles, using the similar metal thio- and seleno- precursors to prepare nanoparticles along with ethyl-hexyl-seleno analog, for the production of the respective II-IV nanoparticles.

Nair *et al.*[48] has recently reported the synthesis of CdS nanoparticles from the complex of cadmium with dithiobiurea. The precursor was decomposed in tri-*n*-octylphosphine oxide to give CdS nanoparticles that show quantum confinement effects with characteristic close to band edge luminescence. Anisotropic shaped CdS nanocrystals were also prepared by Nair, *et al.*[22] using $[Cd(NH_2NHNH_2)_2Cl_2]$ as a single-source

precursor. The as-prepared rods exhibited a very slight blue shift in relation to bulk CdS. In this work, the ultimate shape control parameters are employed to synthesize CdS nanorods and, PbS nanoparticles, using the respective thiosemicarbazide complexes of cadmium and lead described in chapter 2. The nanoparticles are prepared at different monomer concentrations and temperatures to vary their effect in the growth and final morphologies. The method used involves dissolving the precursor in TOP, which is then injected into hot TOPO at high temperatures. The temperature is maintained for a specified amount of time, with the size of the resulting particles depending on the reaction time, temperature and the precursor concentration. The resulting precipitate is cooled (to ~70°C) followed by the addition of the excess methanol to flocculate the particles. The resulting solid is then separated by centrifugation and dispersed in toluene. The optical properties are investigated using UV-Vis and photoluminescence, whereas structural analysis is achieved by the use of X-ray and electron microscopy. In this work, the effect of the growth temperature, monomer concentration and the precursor on the final morphology of CdS nanoparticles in studied.

3.2 Experimental

3.2.1 Instrumentation

3.2.1.1 UV-Vis spectroscopy

A Perkin Elmer Lambda 20 UV-Vis spectrophotometer was used to perform the optical measurements. The samples were measured in quartz cells (1 cm path length) using toluene as the reference.

3.2.1.2 Photoluminescence

The photoluminescence of the samples was collected using the Perkin Elmer LS 55 spectrometer. The samples were run with toluene as the reference solvent.

3.2.1.3 X-Ray diffraction

The materials research Bruker Axis, D8 Advance, X-ray diffractometer was used to measure the crystallinity of the nanoparticles. The samples were radiated using secondary graphite monochromated Cu Kα ($\lambda = 1.54060$ Å) at 40 kV/50 mA. The samples were supported on silicon slits.

3.2.1.4 Electron microscopy

The TEM (transmission electron microscopy) and HRTEM (higher resolution transmission electron microscopy) patterns were taken using a Phillips CM 200 computage electron microscopy operated at 200 kV with an EDS analyzer. The samples were prepared by placing a drop of dilute solution of the sample in toluene on a copper grid (400 mesh, Agar). The samples were dried completely at room temperature.

3.2.2 Synthesis of Nanoparticles

3.2.2.1 Synthesis of CdS nanoparticles using non-crystalline $[Cd(NH_2CSNHNH_2)_2Cl_2]$: Variation of temperature

For the study of the concentration dependence of the growth of nanoparticles, 0.35 g of precursor was suspended in 4 mL (tri-*n*-octylphosphine) TOP. The suspension was then injected into 4 g hot HDA (hexadecylamine) at temperatures specific for each determination (120 °C, 160 °C and 180 °C). The amount of the precursor, TOP and TOPO (tri-*n*-octylphosphine oxide) was kept constant throughout. The reaction was carried on for one hour after the injection of the precursor. After cooling to 70 °C, methanol was added to flocculate the nanoparticles. The resultant precipitate was separated by centrifugation, followed by a further washing with methanol. The particles were finally suspended in toluene to determine the optical properties.

3.2.2.2 Synthesis of CdS nanoparticles using non-crystalline $[Cd(NH_2CSNHNH_2)_2Cl_2]$: Variation of concentration at 200 °C

For the study of concentration-dependence of the growth, a certain amount of precursor specific for the determination was dissolved in 4 mL TOP. The suspension was then injected into 4 g hot HDA at 200 °C. The amounts of precursor varied for growth in each determination are 1.0 g, 0.75 g and 0.35 g. The temperature parameter was kept constant. The precursor was injected and the reaction proceeded for one hour, after which methanol was added to the cooled solution. The flocculated nanoparticles were then separated by centrifugation. The particles were then washed with methanol and finely dissolved in toluene for their optical measurements.

3.2.2.3 Synthesis of CdS nanoparticles using non-crystalline $[Cd(NH_2CSNHNH_2)_2Cl_2]$ precursor material: Variation of concentration at 120 °C

A certain amount of precursor specific for the determination was dissolved in 4 mL TOP. In this series, the suspension was injected into 4 g hot HDA at 120 °C. The amounts of precursor varied for growth in each determination were 1.0 g, 0.75 g and 0.35 g, varying the effect of the precursor concentration while keeping the temperature parameter constant. The temperature parameter was kept constant. The precursor was injected and the reaction proceeded for one hour, after which methanol was added to the cooled (to *ca.* 70 °C) solution. The flocculated nanoparticles were then separated by centrifugation. The particles were then washed with methanol and finely dissolved in toluene for their optical measurements.

3.2.2.4 Synthesis of CdS nanoparticles using crystalline complex A, $[Cd(NH_2CSNHNH_2)Cl_2]_n$ precursor material: Variation of the nature of the precursor

Hexadecylamine (4 g) was degassed at 120 °C for 30 min. The HDA was then heated to 140 °C under nitrogen. Complex B (0.25 g, 0.684 mmol) was suspended in tri-*n*-octylphosphine (4 mL) and injected into the hot HDA. The reaction was allowed to proceed for 30 min and then the yellow suspension was cooled to 70 °C and the product isolated by washing with methanol (2x50 mL) and centrifuging.

3.2.2.5 Synthesis of CdS nanoparticles using crystalline complex B, $[Cd(NH_2CSNHNH_2)_2Cl_2]_n$ precursor material: Variation of the nature of the precursor

Hexadecylamine (4 g) was degassed at 120 °C for 30 min. The HDA was then heated to 140 °C under nitrogen. Complex B (0.25 g, 0.684 mmol) was suspended in tri-*n*-octylphosphine (4 ml) and injected into the hot HDA. The reaction was allowed to proceed for 30 min and then the yellow suspension was cooled to 70 °C and the product isolated by washing with methanol (2x50 mL) and centrifuging.

3.2.2.6 Synthesis of the PbS nanoparticles using $[Pb(NH_2CSNHNH_2)(NO_3)_2]$

0.25 g of $[Pb(NH_2CSNHNH_2)(NO_3)_2]_n$ was suspended in 6 mL TOP and injected into 10 g of TOPO at 240 °C. The reaction was allowed to proceed for 1 hr. Methanol was added to give a grey precipitate, which was dried and re-dispersed in chloroform.

3.3 Results and discussions

3.3.1 Synthesis of CdS nanoparticles using non-crystalline $[Cd(NH_2CSNHNH_2)_2Cl_2]$ precursor material: Variation of temperature

3.3.1.1 Optical properties

For the temperature dependence on the growth of nanoparticles, the determinations were carried out at the constant precursor concentration (0.35 g in 4 mL TOP injected into 4 g TOPO) at 120 °C, 160 °C and 180 °C. The onset UV/visible light absorption of semiconductor nanoparticles is attributed to the band gap absorption, and this will be blue shifted (shift to shorter wavelengths) relative to the absorption of their bulk materials due to quantum size confinement effects. Thus Figure 3.5(a) shows that the UV/visible thresholds of all the samples for this determination are blue shifted relative to the bulk CdS nanoparticles (E_g = 515 nm, 2.41 eV), suggesting the formation of the nanoparticles. The samples exhibit band edges at 450 nm (2.76 eV), 470 nm (2.63 eV) and 510 nm (2.43 eV), respectively, with the increase in growth temperature (from 120 - 180 °C). At 120 °C, the absorption spectrum shows a sharp excitonic peak at 410 nm due to strong quantum confinement. The shift from the blue to the red region (as the temperature increase from 120 - 180 °C) could be attributed to the decreasing degree of confinement of the charge carriers within the excitonic Bohr radius, as a result of the increase in size with the increasing temperature. Consequently, the broadened band edge of the particles at 180 °C is at 510 nm (2.43 eV), suggesting a weaker confinement due to larger particle sizes. The peaks for the particles made at 120 and 140 °C show excitonic shoulders in their absorptions owing to the monodispersity of the particles.

The variation of the CdS nanoparticles in the fluorescence spectrum of the nanoparticles with temperature is shown in Figure 3.5 (b). The peak with the maximum intensity at 473 nm for CdS made at 120 °C is sharp and locates near the absorption edge, suggesting the occurrence of an excitonic emission. As the reaction temperature is elevated to 160 °C and 180 °C the longer wavelength emission loses intensity and thus their quantum yield. The emission for the sample at 180 °C can be assigned to deeply trapping surface states (trapped charge carriers on the nanocrystals surface because of surface defects) because it occurs at lower energy relative to the absorption band edge. However as we move to the higher temperatures the process becomes out of control and the particles aggregate, also forming surface irregularities as a result of trapped luminescence. The surface states result from defects, dangling (coordination) bonds, and polar adsorbates. Higher growth temperatures lead to faster growth rates and therefore the surface roughening and degradation compete with the surface ordering. Higher temperatures induce surface degradation, which reduces the luminescence shortly after the maximum efficiency has been reached.[81]

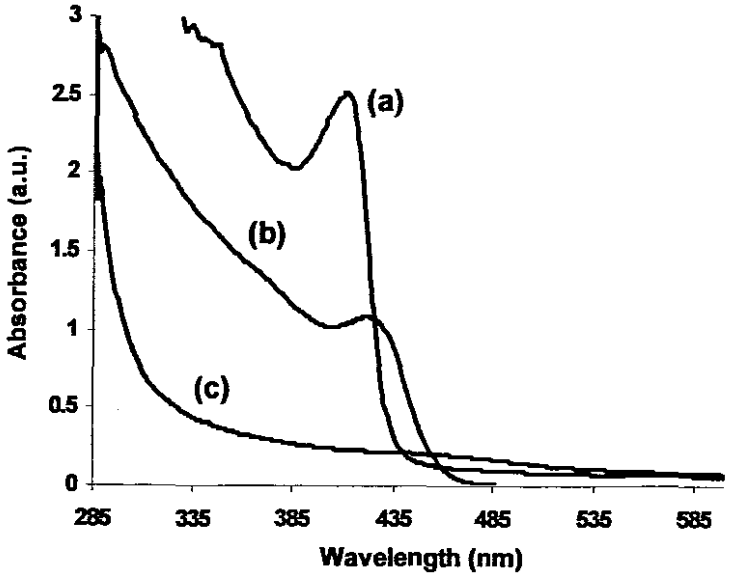

Figure 3.5: *The optical absorption spectra of CdS nanoparticles at (a)120 °C, (b) 160 °C and (c) 180 °C, from 0.35 g of* $Cd(NH_2CSNHNH_2)_2Cl_2$.

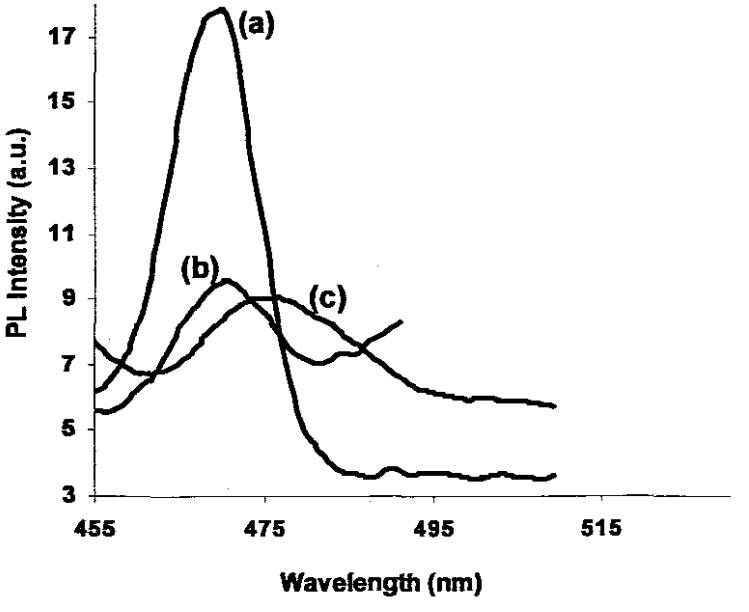

Figure 3.6 : *The photoluminescence spectra of CdS nanoparticles at (a) 120 °C, (b) 160 °C and (c)180 °C, from 0.35 g of* $Cd(NH_2CSNHNH_2)_2Cl_2$.

3.3.1.1 Structural properties

The Transmission Electron Microscopy (TEM) image of the CdS nanocrystals prepared at different temperatures is presented in Figure 3.6. This picture shows how significantly the reaction temperature affects the growth and shape of the nanocrystals. In this series the temperature determines whether the reaction would either undergo a kinetic or a thermodynamic growth regime. Very long rods with *ca.* 40 nm in length and 6 nm in breadth are formed at 120 °C (Figure 3.7 A). These nanorods have an average aspect ratio of 6.7. Since this determination was done at a median monomer concentration and moderate reaction time, there is a very low consumption of the monomers at this temperature, which keeps the reaction at kinetic growth regime, enhancing the seeds of the anisotropically-shaped CdS nanocrystals.

As the temperature is increased to 160 °C, shorter and more monodispersed rods, with an average length of 25 nm and a breadth of 5 nm formed. Relative to the rods obtained at 120 °C (A), the rods in this determination are shorter and thus their average aspect ratios decrease to *ca.* 5. At 180 °C (C), the evolution to very short and irregular shaped rods and dots occur, with particle sizes of *ca.* 16 nm in length and 10 nm in breadth. The average aspect ratio decreases significantly to 3.5 on average (Figure 3.8). At this temperature there is a high consumption of the monomers and the thermodynamic growth regime takes over the kinetic growth, as a result of the coexistence of the two regimes. Consequently, one-dimension to two dimension inter-particle ripening (or 1D/2D-ripening) occurs, in which case the rod shape particle changes to dot shape

particles. The micrograph shown in (Figure 3.7 C) could be attributed to the consequence of this effect. These particles (Figure 3.7 C) are somewhat bulky, which could be attributed to uncontrollable growth at higher temperatures. The size distribution histograms for the as prepared nanorods are shown in Figure 3.8 (a), (b) and (c) for nanorods made at 120, 160, and 180 °C, respectively.

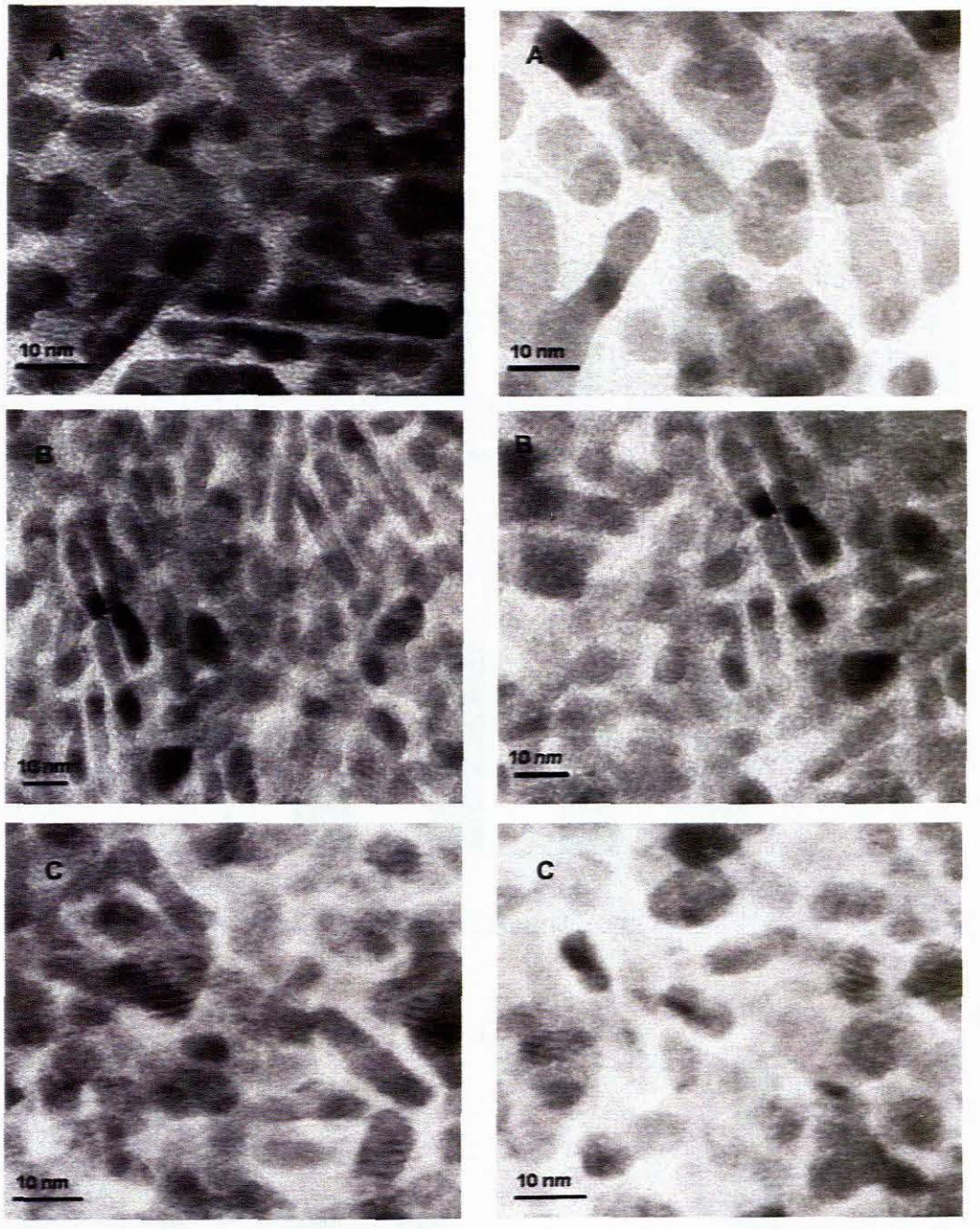

***Figure 3.7**: TEM images of CdS nanoparticles synthesized at A, 120 °C; B, 160 °C; and C, 180 °C; each at two different regions of the sample, from 0.35 g of $[Cd(NH_2CSNHNH_2)Cl_2]_n$.*

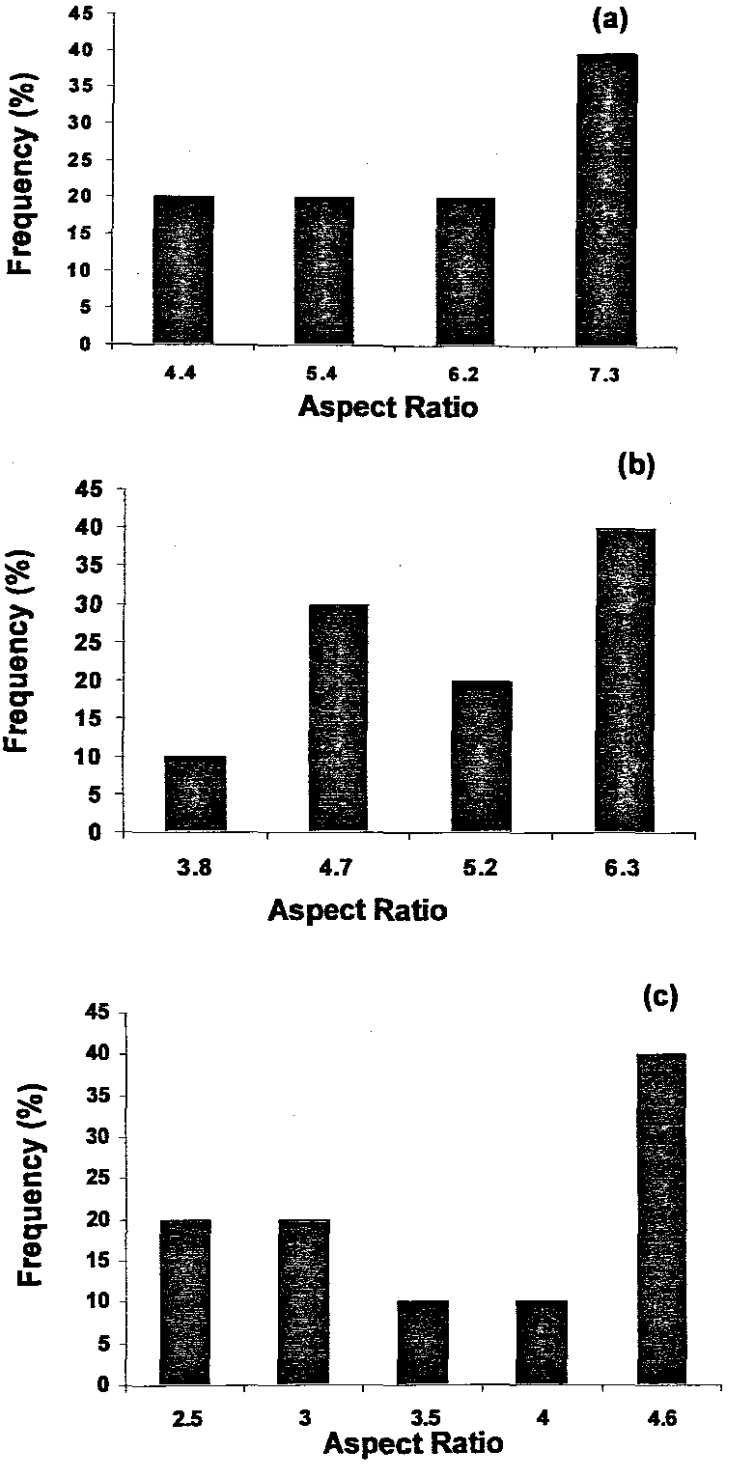

***Figure 3.8**: Aspect ratio histograms for the CdS nanorods synthesized at (a) 120 °C, (b)160 °C and (c) 180 °C, with 0.35 g of $[Cd(NH_2CSNHNH_2)Cl_2]_n$.*

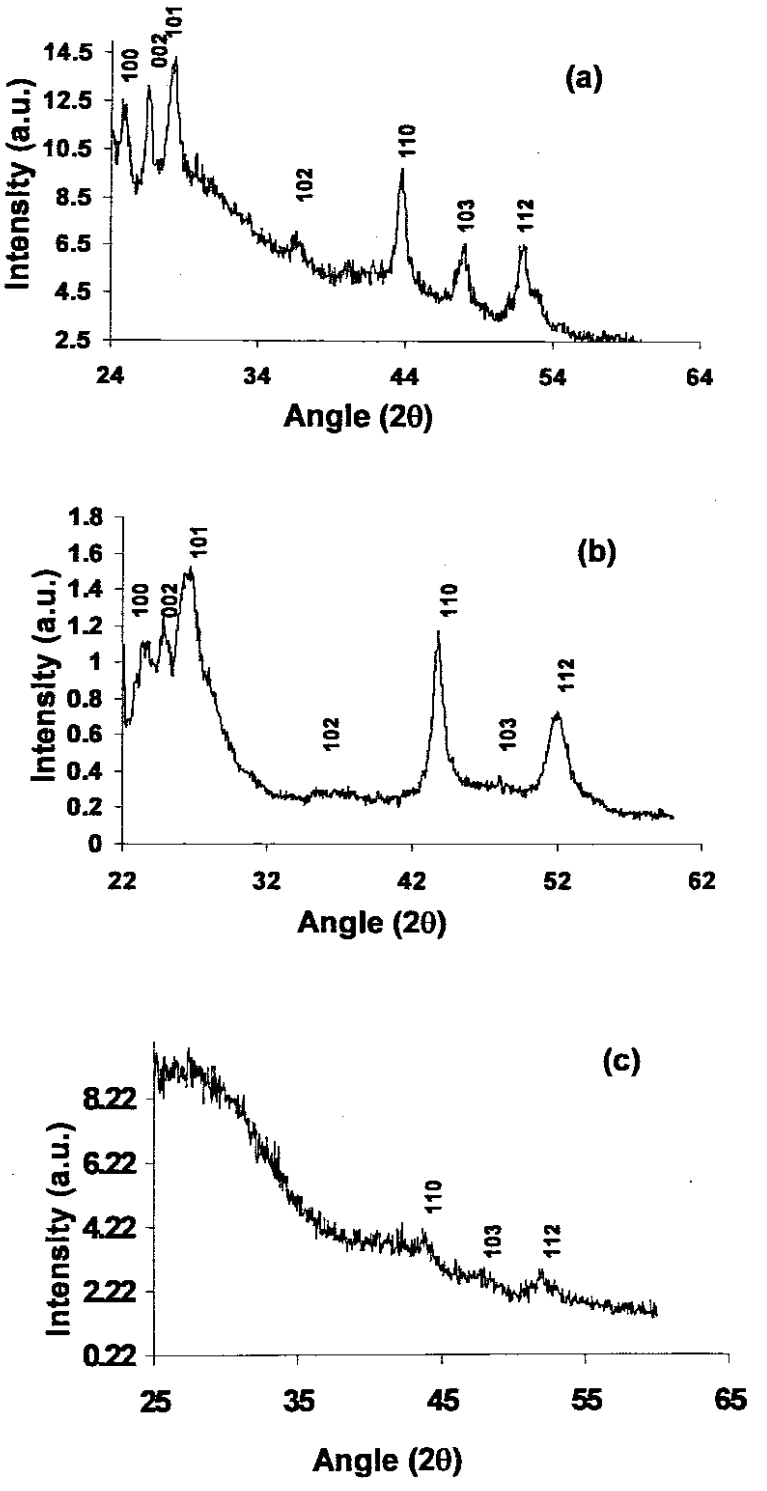

***Figure 3.9**: XRD patterns of CdS nanoparticles synthesized at (a) 120 °C, (b) 160 °C and (c) 180 °C, with 0.35 g of $[Cd(NH_2CSNHNH_2)Cl_2]_n$*

The XRD of the respective nanocrystals are shown in Figure 3.9 (a), (b) and (c). In all three samples, the patterns can be indexed to wurtzite-phase CdS confirmed by the peaks indexed at (110), (103) and (112). The (110), (002) and (101) peaks observed at diffraction patterns (a) and (b) suggest the elongation of the hexagonal phase along the *c*-axis, forming rod-shaped particles. The XRD in Figure 3.9 (c) suggests the formation of the simple hexagonal shape, since the (110), (002) and (101) peaks are merged into one broad peak. It is, however, observed that the higher the reaction temperature, the weaker and broader the diffraction peaks of the resultant CdS nanocrystals. This observation is contrary to the report by Li, *et al.*[86] in which the mean size of the nanocrystals increased with increasing reaction temperature using ethyl xanthate precursor. This suggests that there is amorphous mass of particles which do not yield adequate XRD patterns, as confirmed to the micrographs in Figure 3.7 (C).

3.3.2 Synthesis of CdS nanoparticles using non-crystalline $[Cd(NH_2CSNHNH_2)_2Cl_2]$: Variation of concentration at 200 °C

3.3.2.1 Optical properties

For this synthesis, the reaction temperature was kept at 200 °C and the amount of precursor was varied from 1.0 g, 0.70 g to 0.35 g. This (200 °C) is at a very high reaction temperature and it was chosen to compensate for higher precursor concentrations enhancing the quantitative conversion of the magic nuclei into particles of defined shapes and sizes. Figure 3.10 shows the UV/visible spectra of CdS nanocrystals at varied conditions. The CdS nanoparticles synthesized using 1.0, 0.70

and 0.35 g of the precursor exhibit band edges at 512 nm (2.42 eV), 507 nm (2.45 eV) and 500 nm (2.48 eV).

It is noted that the increase in the particle size is pronounced as the absorption edge shifts from the blue to the red region of the UV/Visible spectrum, which also results on the tailing of the spectra towards the red region. The band edges of these samples are blue-shifted with respect to bulk CdS (E_g =515 nm, 2.41 eV), confirming the existence of the quantum confinement effects in the samples. However, it is observed that the confinement (band edges in relation to the bulk) is rather weak, which could be attributed to the larger particle size.

Since the precursors were injected and the growth was carried out at 200 °C it could be concluded that irrespective of precursor concentration, high temperatures favor the formation of large and aggregated particles. As a result of very weak quantum confinement is observed in the UV/Visible light absorption spectrum. The samples exhibit emission (Figure 3.11) assigned to deep trap surface states because the emissions occurs at higher energies relative to the absorption band edge. At the wavelengths expected for the emission of the normal surface ordered CdS, the spectra flattens. The emission maximum peaks in the photoluminescence spectra is observed at 451 nm (2.75 eV), 457 nm (2.71 eV) and 470 nm (2.63 eV) for the 0.35, 0.7, and 1.0 g samples, respectively(Figure 3.11).

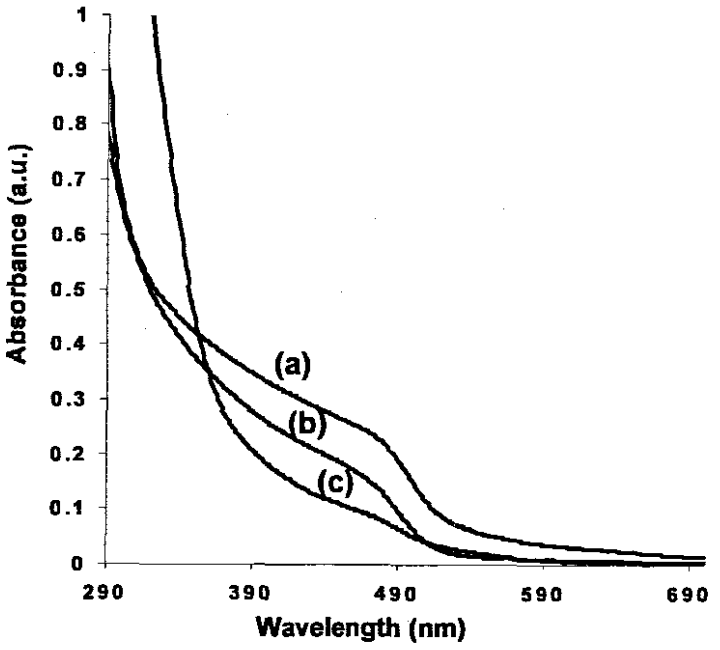

Figure 3.10: *The optical absorption spectra of CdS nanoparticles from (a) 0.35 g, (b) 0.70 g, and (c) 1.0 g of* $Cd(NH_2CSNHNH_2)_2Cl_2$ *at 200 °C.*

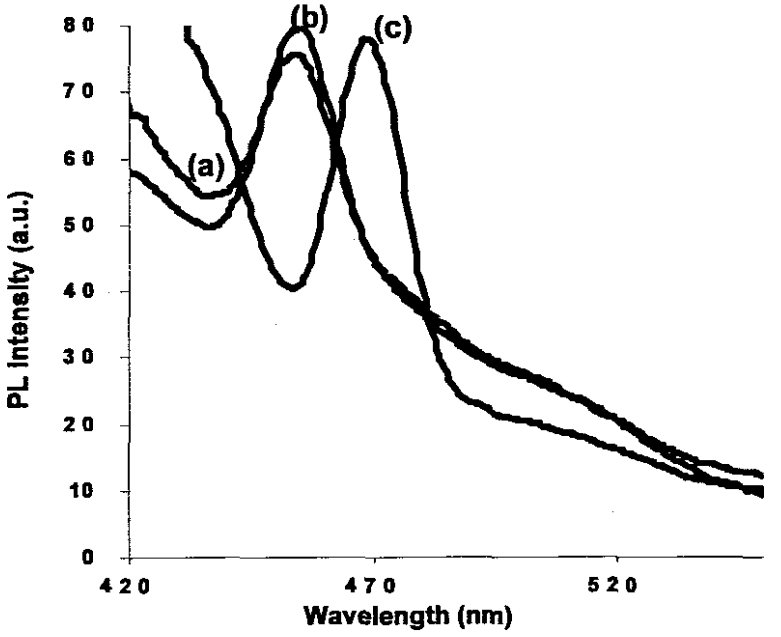

Figure 3.11: *The photoluminescence spectra of CdS nanocrystals from (a) 0.35 g, (b) 0.70 g, and (c) 1.0 g of* $Cd(NH_2CSNHNH_2)_2Cl_2$ *at 200 °C.*

3.3.2.2 Structural properties

When the temperature of the system is fixed, the chemical potential of the reaction environment in the synthesis of the nanoparticles is mainly determined by the monomer concentration.[82-86] In this concentration effect determination system, the reaction is driven at 200 °C, which supplies the high thermal energy. Injecting 1.0 g (high monomer concentration) into this system causes the system to be highly kinetically driven in a growth regime extremely far away from a thermodynamic equilibrium. Under these conditions, a fast reaction rate would be expected, as a result of the system becoming completely out of control, thereby worsening the monodispersity. This accounts for the aggregated shapes observed in the TEM images shown in Figure 3.12 (A) with average particle sizes of *ca.* 40 nm. The mean particle size distribution is shown in Figure 3.13. In this image, hexagonal shapes are observed, which suggests kinetically driven reaction procedure. However, the hexagonal shape is used as an advantage to grow elongated anisotropic shapes (rod shape is the result of the elongation of the hexagonal shape along the *c*-axis).

At 0.7 g, the monomer concentration was high enough to grow the nanocrystals in the one-dimensional mode. At sufficiently high monomer concentrations, the incoming monomers which diffuse into the diffusion sphere are mainly consumed by the facets perpendicular to the c-axis of the nanocrystals, which results into the one dimensional growth stage.[82,83,86] Figure 3.12 B shows the TEM images (taken at various regions of the sample) at this determination.

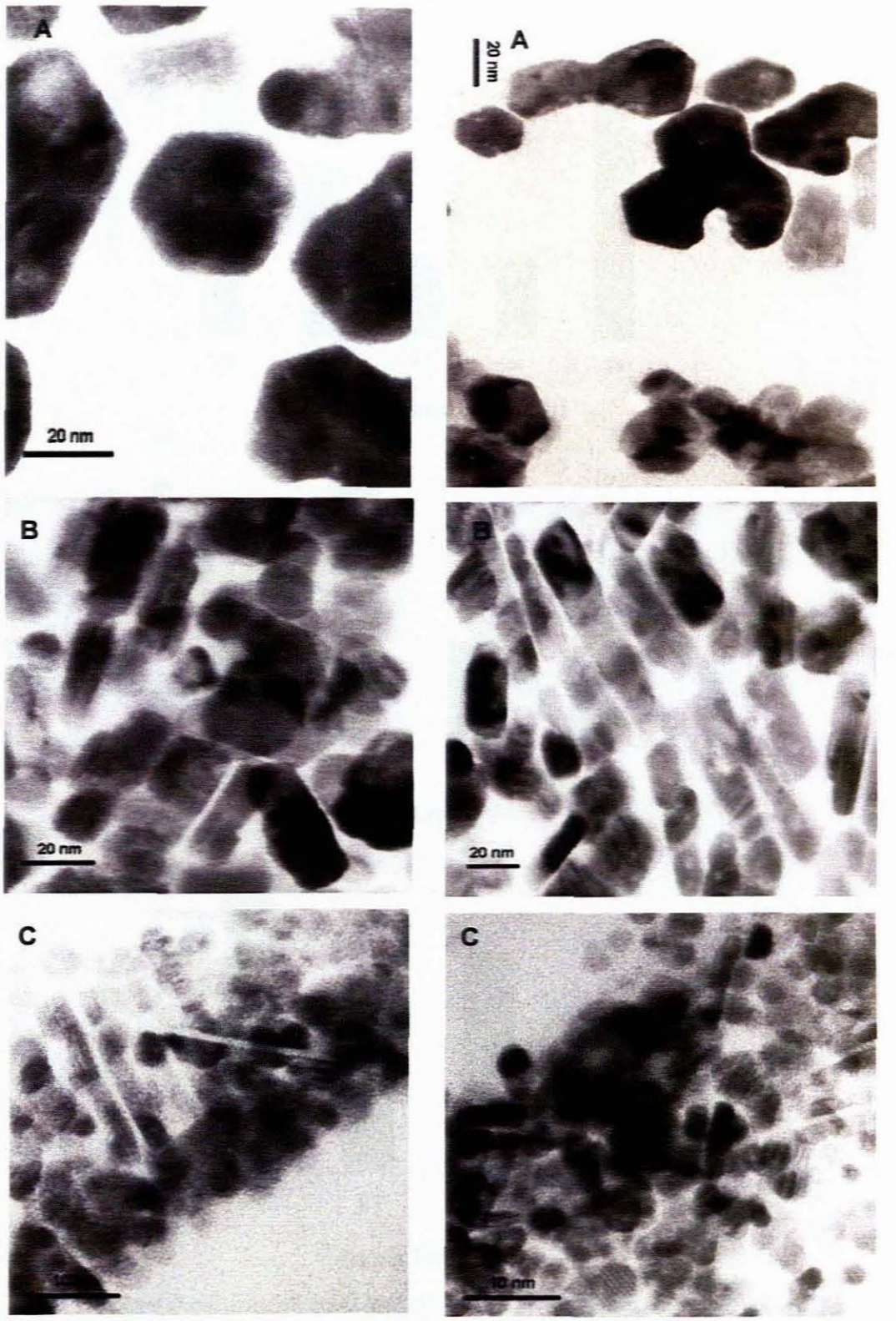

Figure 3.12: *TEM images of CdS nanoparticles synthesized from A, 1.0 g; B, 0.70 g; and C, 0.35 g C of* $Cd(NH_2CSNHNH_2)_2Cl_2$ *at 200 °C.*

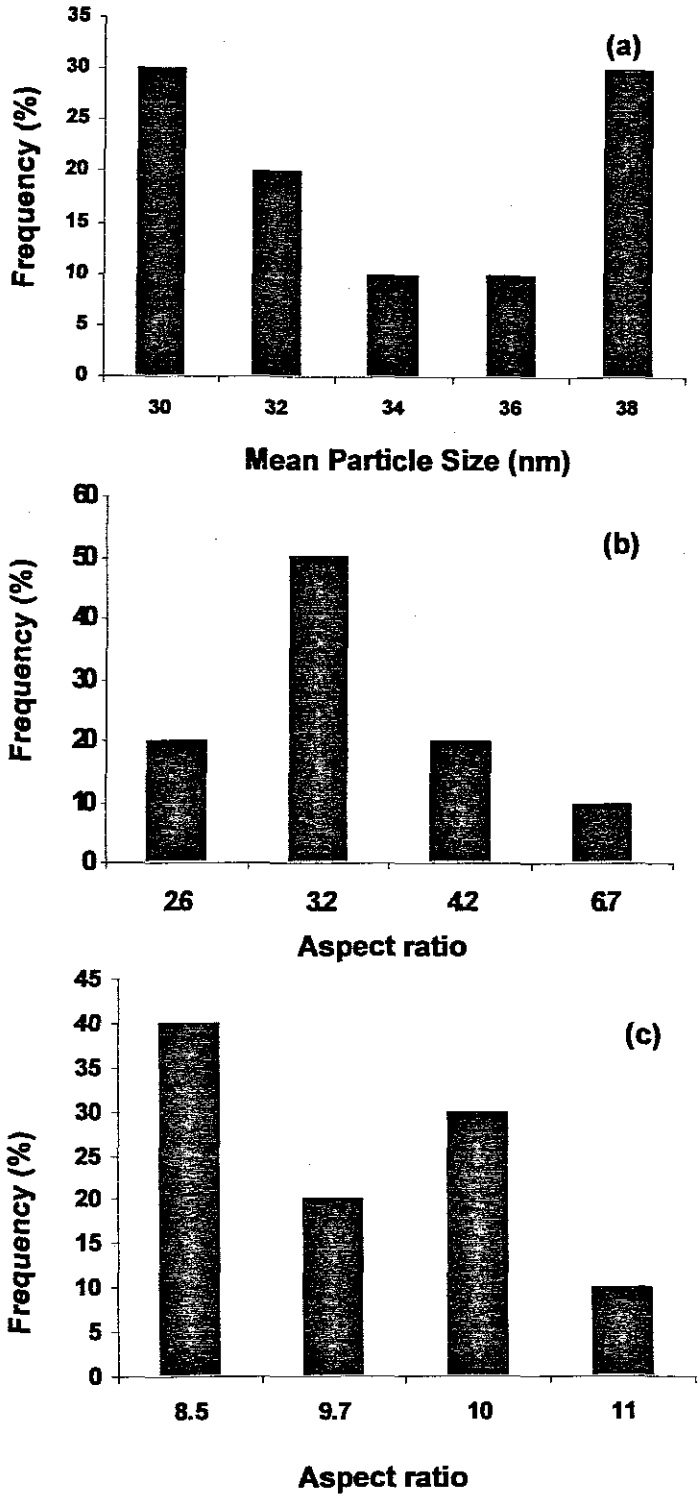

***Figure 3.13**: Aspect ratio histograms of CdS nanorods synthesized from (a) 1.0 g, (b) 0.70 g and (c) 0.35 g of $Cd(NH_2CSNHNH_2)_2Cl_2$ at 200 °C.*

The rods have relatively large diameters, which show that the reaction was at kinetic growth regime, with the reaction completely out of control due to higher concentration and reaction temperature, as a result of non-uniform rods consisting of poorly or undefined shapes (Figure 3.12 B). The rods are ca. 45 nm in length and 15 nm in breadth. Figure 3.12 (C) shows perfect uniform rods compared to the latter (Figure 3.12 B) . Here the rods are *ca.* 50 nm long and 6 nm across, which clearly shows that the reaction was in a rather more ordered procedure. It also shows that this monomer could perfectly compensate for the extremely high temperature to push the reaction to a considerable reaction drive. The average aspect ratio of the rods increase as we move from higher to the lower monomer concentration, giving rods with more defined shapes (Figure 3.13 B-C) and aspect ratios as the reaction gets in control. The size distribution histograms are shown as the frequency versus aspect ratio histograms in Figure 3.13 for the nanoparticles made with 1.0 g (a), 0.70 g (b) and 0.35 g (c).

The powder diffraction patterns of CdS nanocrystals are shown at Figure 3.14 (a), (b) and (c). All diffraction spectra show the presence of (110), (103) and (112) planes indexed to the hexagonal phase of CdS. The narrow peaks at (100), (002) and (101) at (b) and (c) suggest that these nanocrystals are elongated towards the *c*-axis. However, these peaks are broadened, relative to the ones for bulk CdS, showing the presence of the quantum confinement effects at the crystals as a result of finite sized crystallites. Normally, for the elongated hexagonal shapes, the three narrow peaks would be expected (at $2\theta = 25\text{-}35°$), but these peaks merge to form one broad peak in case of non-elongated, faceted CdS. This is observed in the XRD pattern in Figure 3.14 A.

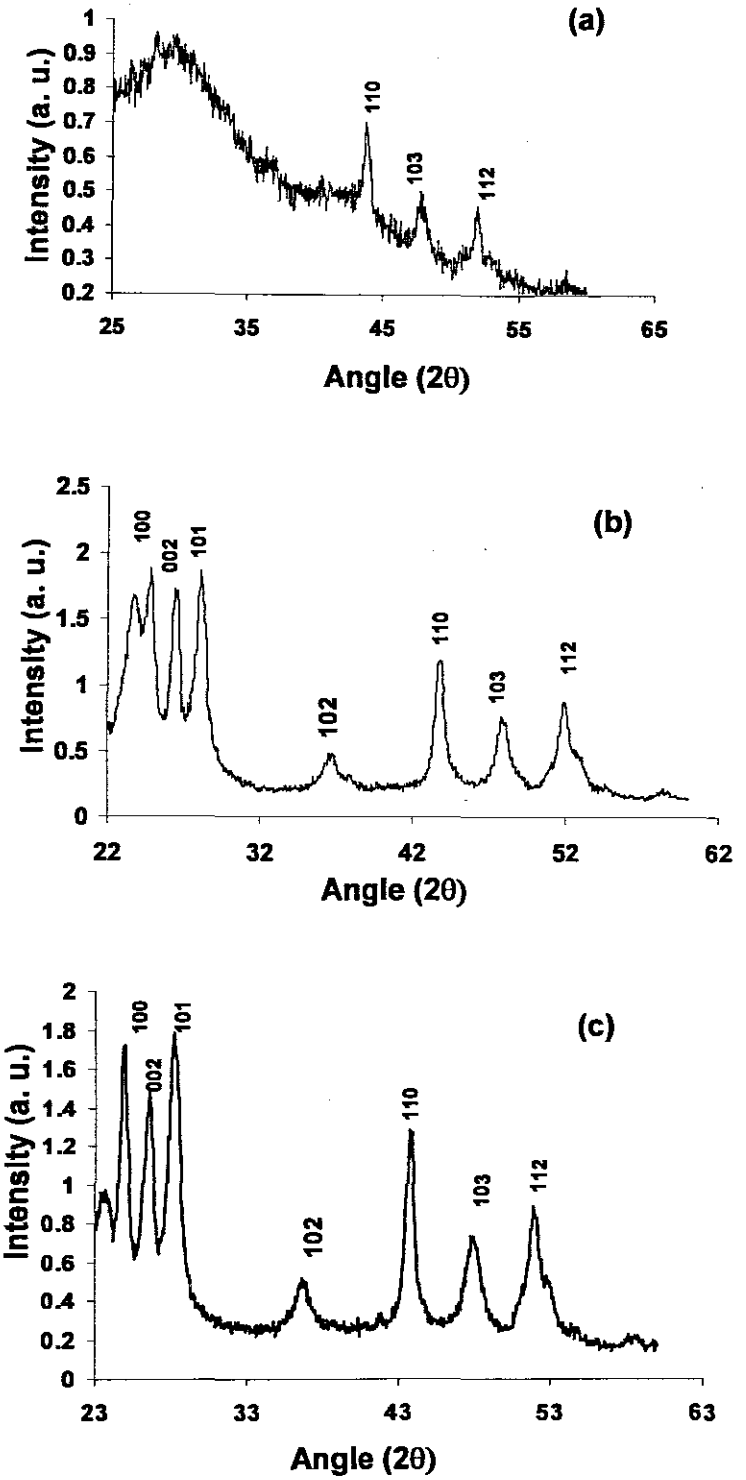

Figure 3.14: *Powder diffraction patterns of CdS nanocrystals made with (a) 1.0 g, (b) 0.70 g and (c) 0.35 g of* $Cd(NH_2CSNHNH_2)_2Cl_2$ *at 200 °C.*

3.3.3 Synthesis of CdS nanoparticles using non-crystalline $[Cd(NH_2CSNHNH_2)_2Cl_2]$: Variation of concentration at 120 °C.

3.3.3.1 Optical Properties

The effect of the precursor concentration on the growth was further varied at a lower temperature. This was done to target the monodispersity of the nanoparticles, since it was poorly achieved at higher temperature (200 °C). The amounts of precursor used were 0.35 g, 0.7 g and 1.0 g. The UV/Visible spectra of these determinations are shown in Figure 3.15. The absorption edge shifts towards the blue region as the concentration of the precursor is decreased, exhibiting the band edges at 485 nm (2.56 eV), 473 nm (621 eV) and 452 nm (2.74 eV).

All these spectra exhibit an excitonic shoulder, which suggests that the nanoparticles are monodisperse. For the nanoparticles prepared with 0.35 g, this argument is supported by the narrow emission peak on the photoluminescence spectrum (Figure 3.16). This peak is very narrow (*ca.* 20 nm) and the relative intensity shows good quantum yields of the sample, peaking at 470 nm (emission maximum), which is a very small shift (3 nm) from its absorption edge.

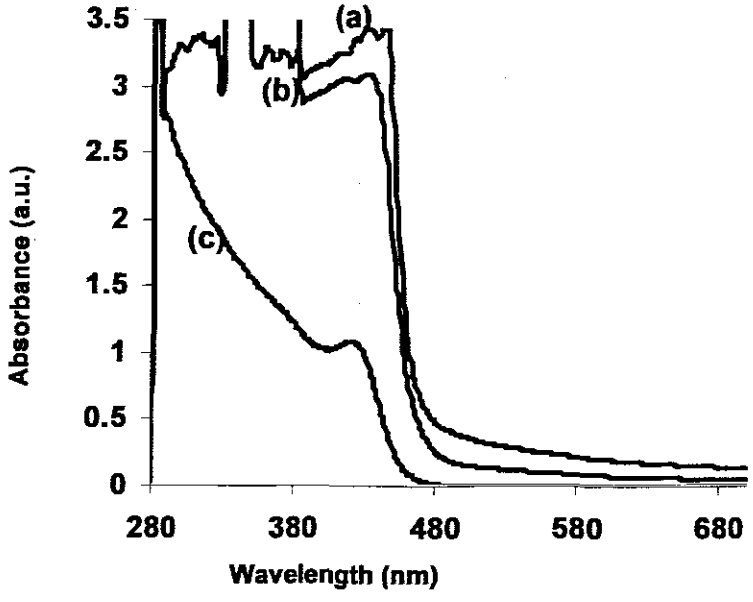

***Figure 3.15**: Optical absorption spectra of CdS nanoparticles from (a) 0.35 g, (b) 0.70 g, (c) 1.0 g of $Cd(NH_2CSNHNH_2)_2Cl_2$ at 120 °C.*

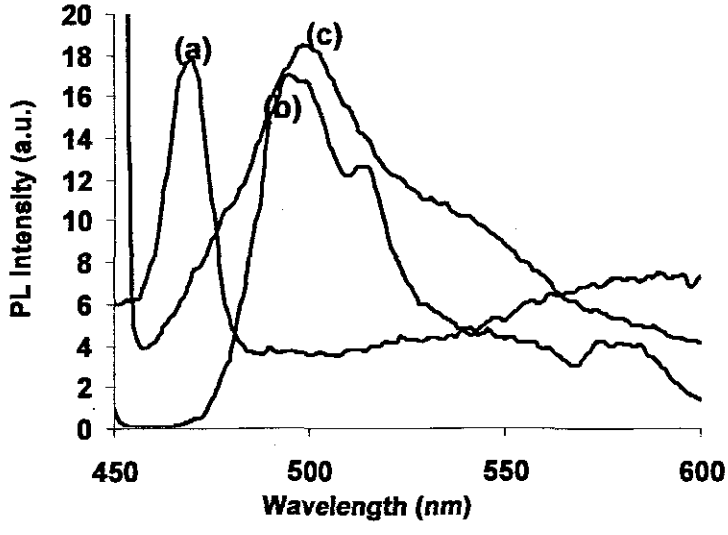

***Figure 3.16**: Photoluminescence spectra of CdS nanoparticles from (a) 0.35 g, (b) 0.70 g, (c) 1.0 g of $Cd(NH_2CSNHNH_2)_2Cl_2$ at 120 °C.*

The photoluminescence peak of the sample at 1.0 g with the emission maximum at 501 nm (2.48 eV) is very broad and Stokes-shifted undergoing spectral diffusion. Spectral diffusion can be explained as the trapping of photogenerated excess charge carriers in the surface defects of the nanocrystal.[24] The local electric field created by these charges presumably disturbs the energy levels of the nanocrystal causing a shift in the emission energy. The energy band bending, caused by the increase of electric field inside the nanoparticle, tends to separate a confined electron and a hole thus reducing their overlap of wave functions and reducing the effective band gap, which leads to reduced oscillator strength. So the quantum confined stark effect manifests itself as a decrease of the intensity of the emission peak, concomitantly with its red shift, as well as its broadening. However, with the release of the trapped charge carrier, the induced local electric field decreases, the emission energy increases and its intensity increases.[24] The sample where 0.70 g is used shows luminescence at 470 nm (2.64 eV) with the major peak at 490 nm (2.53 eV) with a minor peak linked to it at 515 nm (2.41 eV). The first major peak can be attributed to the sample's luminescence and the second minor peak attributed to the trapping of the charge carriers due to the surface irregularities in the sample.

3.3.3.2 Structural properties

When the reaction temperature for the above determination was decreased to 120 °C and repeated, the shape evolution was different from that one observed for the determination at 200 °C. In principle, the higher the monomer concentration at lower

temperatures, the smaller the critical nuclei, facilitating the nucleation process.[82,83,86] Figure 3.17 A shows the formation of long rods with high aspect ratios (6 in average) of 50 nm average length and 7.3 nm average breadth. If the monomer concentration is decreased to 0.70 g (Figure 3.17 B), the average aspect ratio of the nanorods is decreased to ca 6.2.

If the chemical potential of the monomers in the bulk solution is comparable to the overall chemical potential of the entire crystal, there is no net diffusion flux between the bulk solution and the diffusion sphere. The monomers on the surface of the nanocrystal adjust their positions to minimize the total surface energy of a given crystal, resulting in a change from a rod-shape to a dot shape, when the reaction reaches the thermodynamic growth regime. This effect is observed in the TEM image in Figure 3.17 C, which shows particles with average particle sizes of *ca.* 13 as the concentration is decreased to 0.35 g. It was interesting to find out that the complete shape evolution from high aspect ratio rods to the shorter rods, and eventually dots could be related to the one reported by Li, *et al.*[86] for CdS nanocrystals and Peng, *et al.*[82,83] for CdSe nanocrystals. The aspect ratio histograms are shown in Figure 3.18 (a), (b) and (c) for nanoparticles made from 1.0, 0.70 and 0.35 g of precursor, respectively.

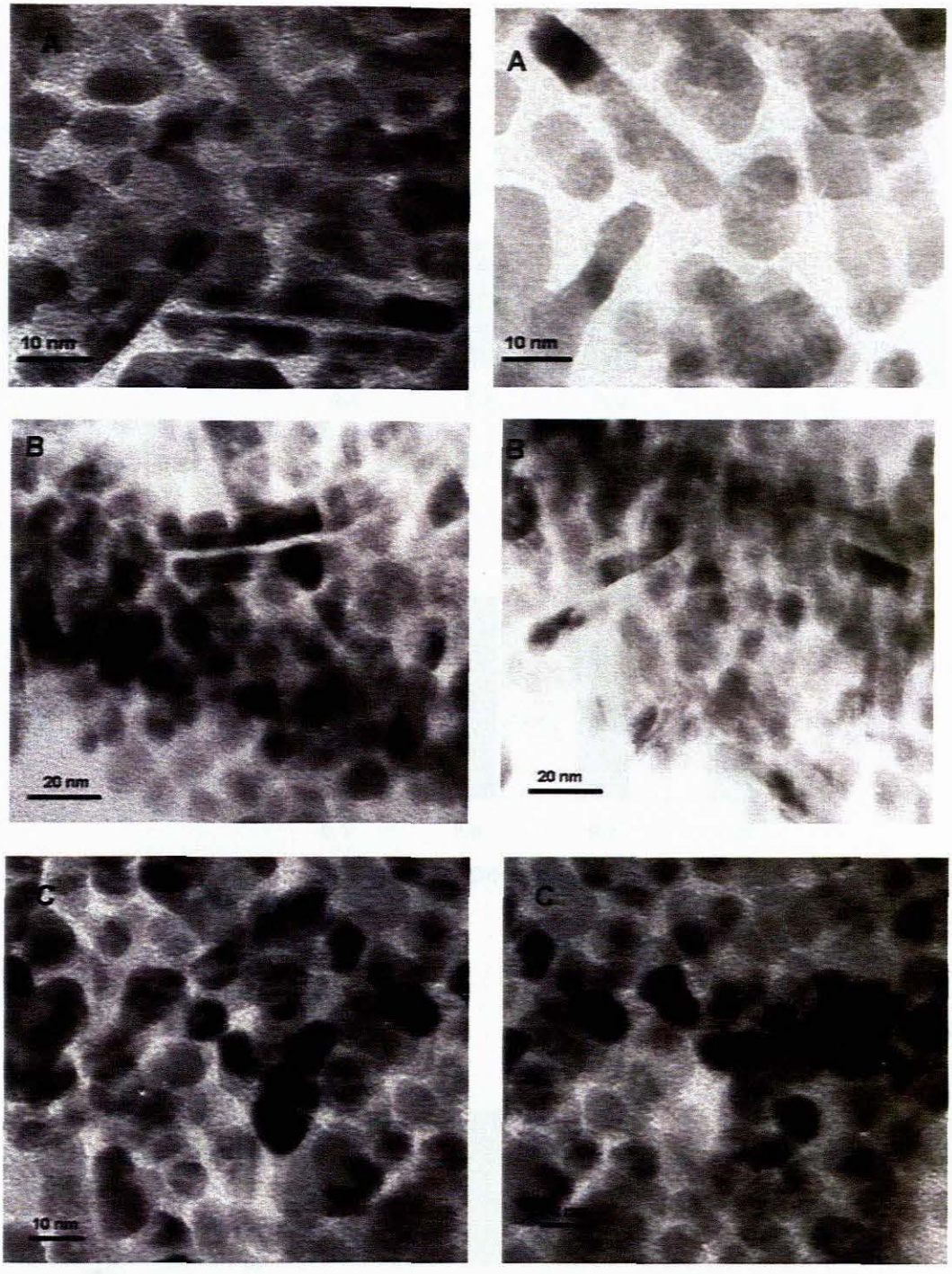

***Figure 3.17**: TEM images of CdS nanocrystals showing variation of morphology with different precursor amounts concentrations synthesized from A, 1.0 g; B, 0.70 g; and C, 0.35 g at 120 °C using $Cd(NH_2CSNHNH_2)_nCl_2$.*

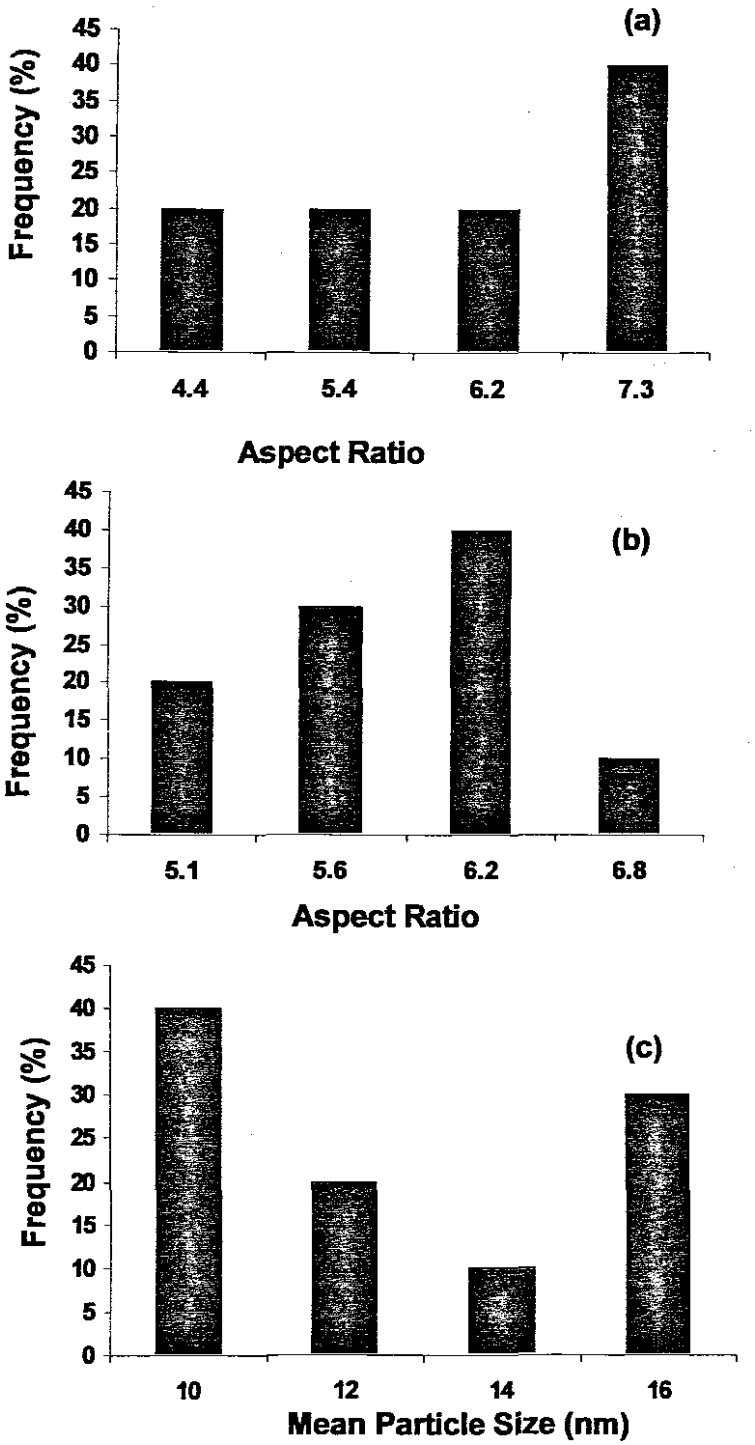

***Figure 3.18**: Aspect ratio histograms of CdS nanorods synthesized from (a) 1.0 g, (b) 0.70 g and (c) 0.35 g of $Cd(NH_2CSNHNH_2)_2Cl_2$ at 120 °C.*

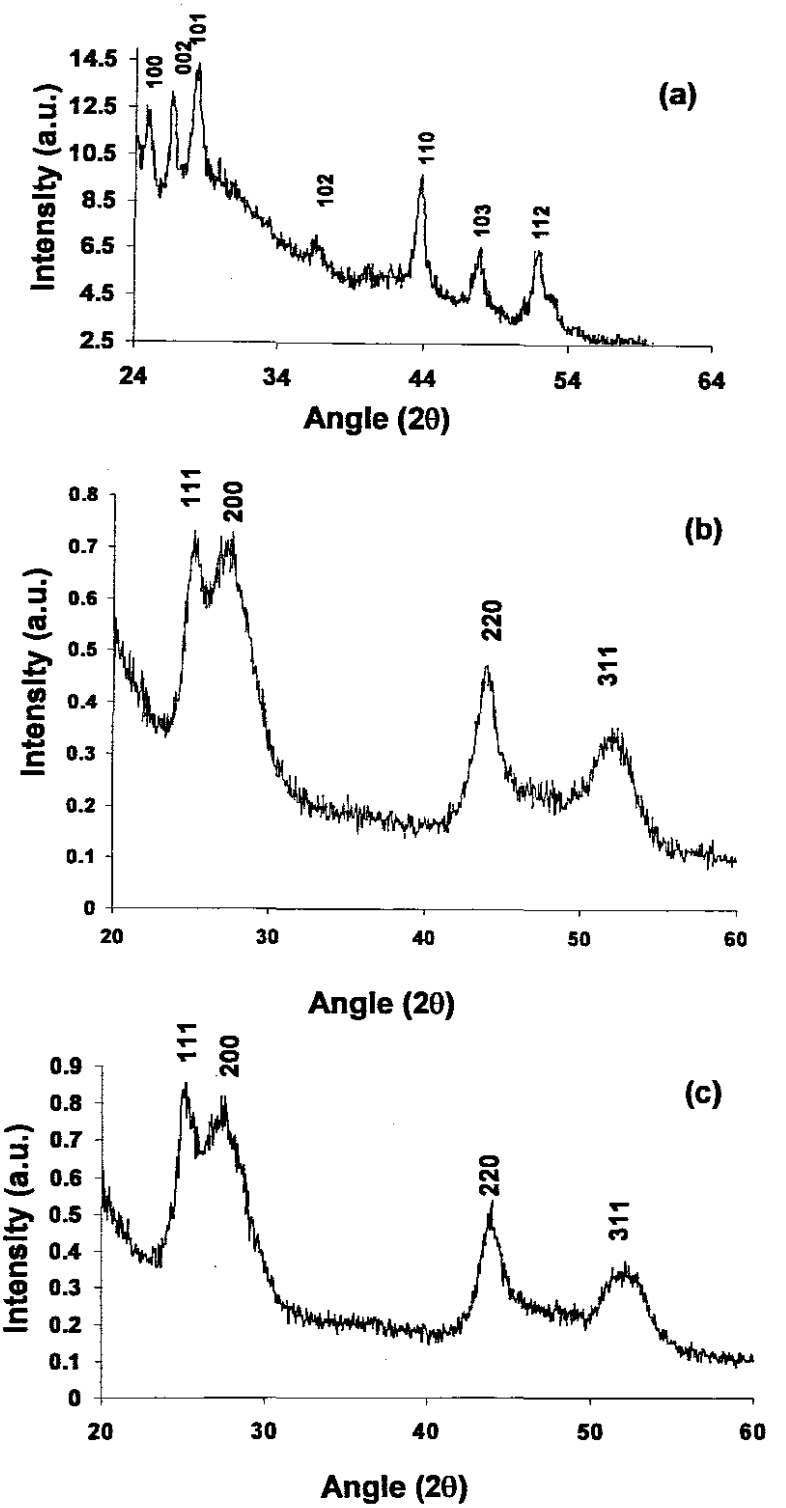

***Figure 3.19**: The diffraction patterns of CdS nanoparticles with (a) 1.0 g, (b) 0.70 g and (c) 0.35 g at 120 °C using $Cd(NH_2CSNHNH_2)_nCl_2$.*

The diffraction patterns for the CdS made from 1 g (Figure 3.19 (a)) of the precursor shows the peaks at (110), (103) and (112) planes, which can indexed to the wurtzite phase hexagonal CdS presenting in all the spectra. The narrow peaks at (100), (002) and (101) show that these nanocrystals are elongated towards the *c*-axis. The CdS nanoparticles synthesized using 0.70 g (b) and 0.35 g (c) of the precursor show the diffraction peaks at (111), (200), (220) and (311) suggesting the formation of the face centered cubic phase in the nanoparticles.

3.3.4 Synthesis of CdS nanoparticles using crystalline complex A, $[Cd(NH_2CSNHNH_2)Cl_2]_n$ and B, $[Cd(NH_2CSNHNH_2)_2Cl_2]$: Variation the nature of the precursor

3.3.4.1 Optical Properties

In order to investigate the effect of the molecular architecture of the complex on the morphology of the final nanomaterials both complexes were decomposed in hexadecylamine (HDA) under the same conditions. In both cases a pale yellow product was isolated. The UV/Visible absorption spectra were recorded and showed a significant blue shift in the optical band edge of the materials compared to that for the bulk material (515 nm, 2.41 eV) (A = 430 nm, 2.88 eV; B = 418 nm, 2.96 eV) shown in Figure 3.20. Both spectra exhibit excitonic peaks which is the evidence of the strong confinement of the exciton, also suggesting the formation of the nanoparticulate materials. The photoluminescence spectra both showed a large broad peak at 500 nm which is consistent with the trap defect in cadmium sulfide.

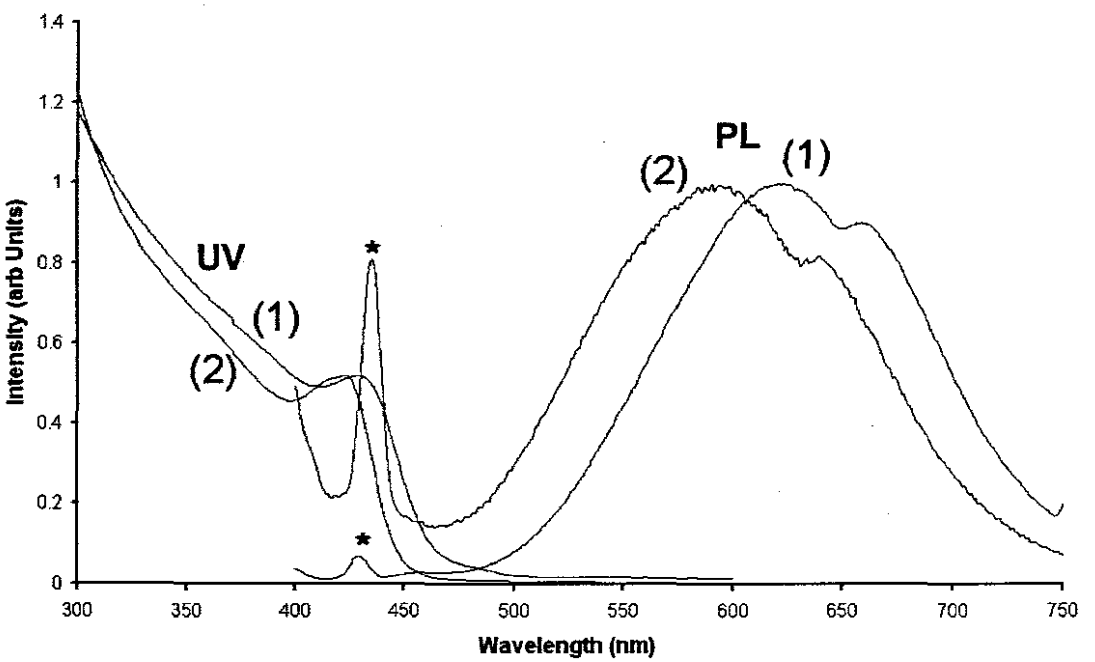

Figure 3.20: *Absorption and photoluminescence spectra of CdS nanorods made from complex A [spectrum (2)], and the one made from complex B [spectrum (1)]*

3.3.4.1 Structural Properties

The TEM images of the CdS nanorods made from complex A and B are shown in Figure 3.21 and 3.22, respectively. Complex A gave the rods of the lower aspect ratios (Figure 3.23) compared to the complex B. However, observing in Figure 3.21 (insert), it is pretty obvious that good crystallinity of the CdS nanorods is achieved with complex A rather than with complex B. This is clearly confirmed by the lattice fringes, with clear and rather accurate 0.334 nm spacing, which was difficult or not possible at all to achieve using complex B. This could be attributed to the entangling of this complex and its branching, compared to A. Powder XRD (Figure 3.24) of the materials

all to achieve using complex B. This could be attributed to the entangling of this complex and its branching, compared to A. Powder XRD (Figure 3.24) of the materials showed a significant difference between the two products. The product from complex A resulted in a typical hexagonal diffraction pattern. However, the diffraction pattern for B was less clear. Initially the pattern seems approximately consistent with a cubic lattice, typified by the absence of the {102} and {103} lines. However, the sharp diffraction line at 25° cannot be ignored and as it is consistent with the {100} plane for the hexagonal form of CdS.

The powder XRD results can be best understood in light of the nanomorphology of the material (Figure 3.24). In both cases there is a predominance of anisotropic material. Whilst in the aspect ratios of the materials, there is a significant difference in the widths of the rods, this feature can be seen from the aspect ratio distributions of the nanorods in Figure 3.23. Compound A gave rods with widths approaching the Bohr radius at 6 nm (±1.5 nm); however compound B results in the formation of rods with significantly smaller widths of 3 nm (±0.5 nm). These rod widths are consistent with the observed UV/visible absorption spectra. Furthermore measurement of the lattice spacing of the rods leads to the conclusion that the long axis is the c-axis of the unit cell. If the powder XRD patterns are considered in the light of this data it may be seen that diffraction from the {100} planes will approximate to an infinite lattice much more closely than planes with contributions from an orthogonal axis. Taking this into account one would expect to see a broadening of the {002} and {101} as well as the {110} and the {112}.

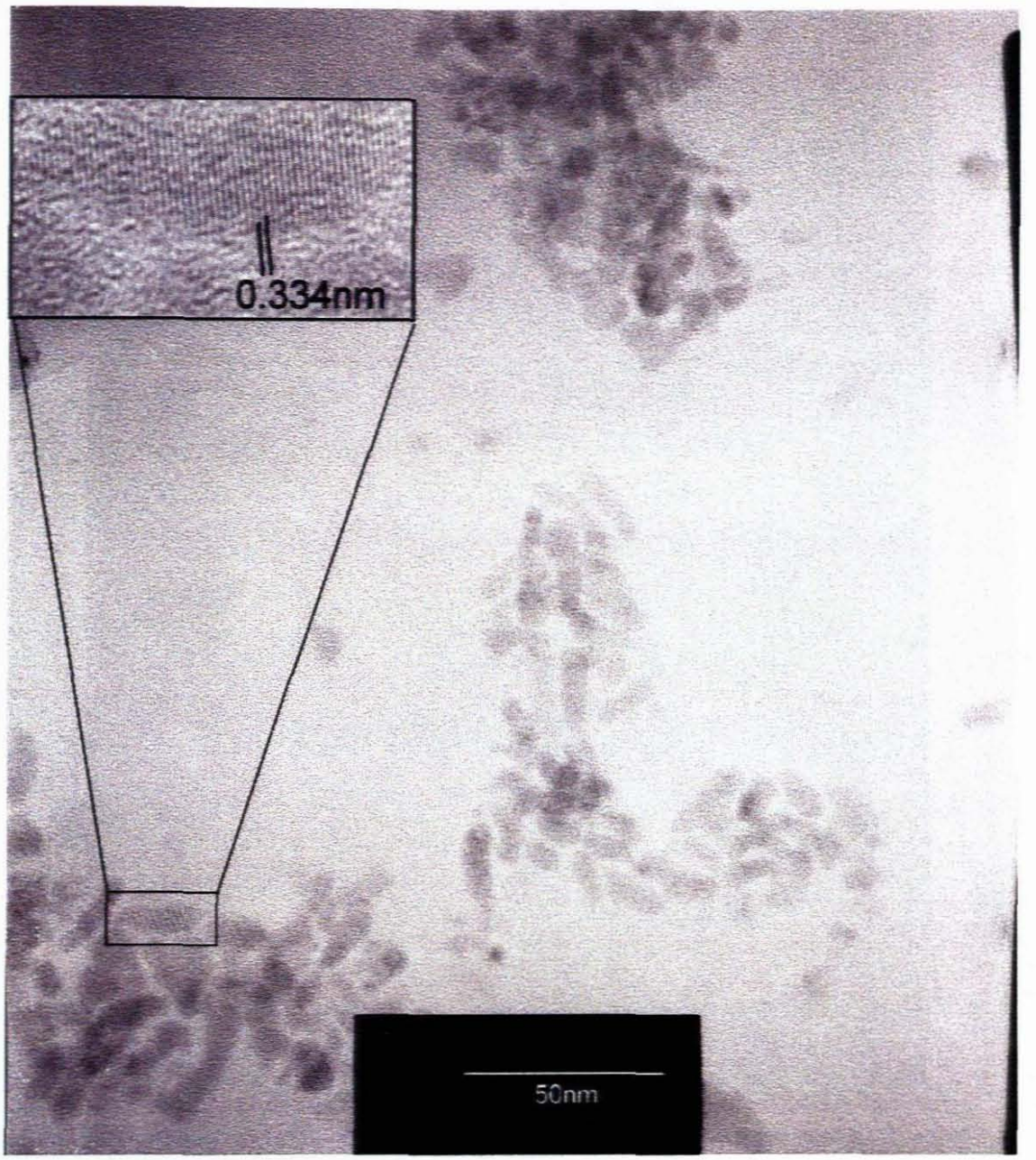

Figure 3.21: *TEM image of the CdS nanorods made from complex A, $Cd(NH_2CSNHNH_2)Cl_2]_n$.*

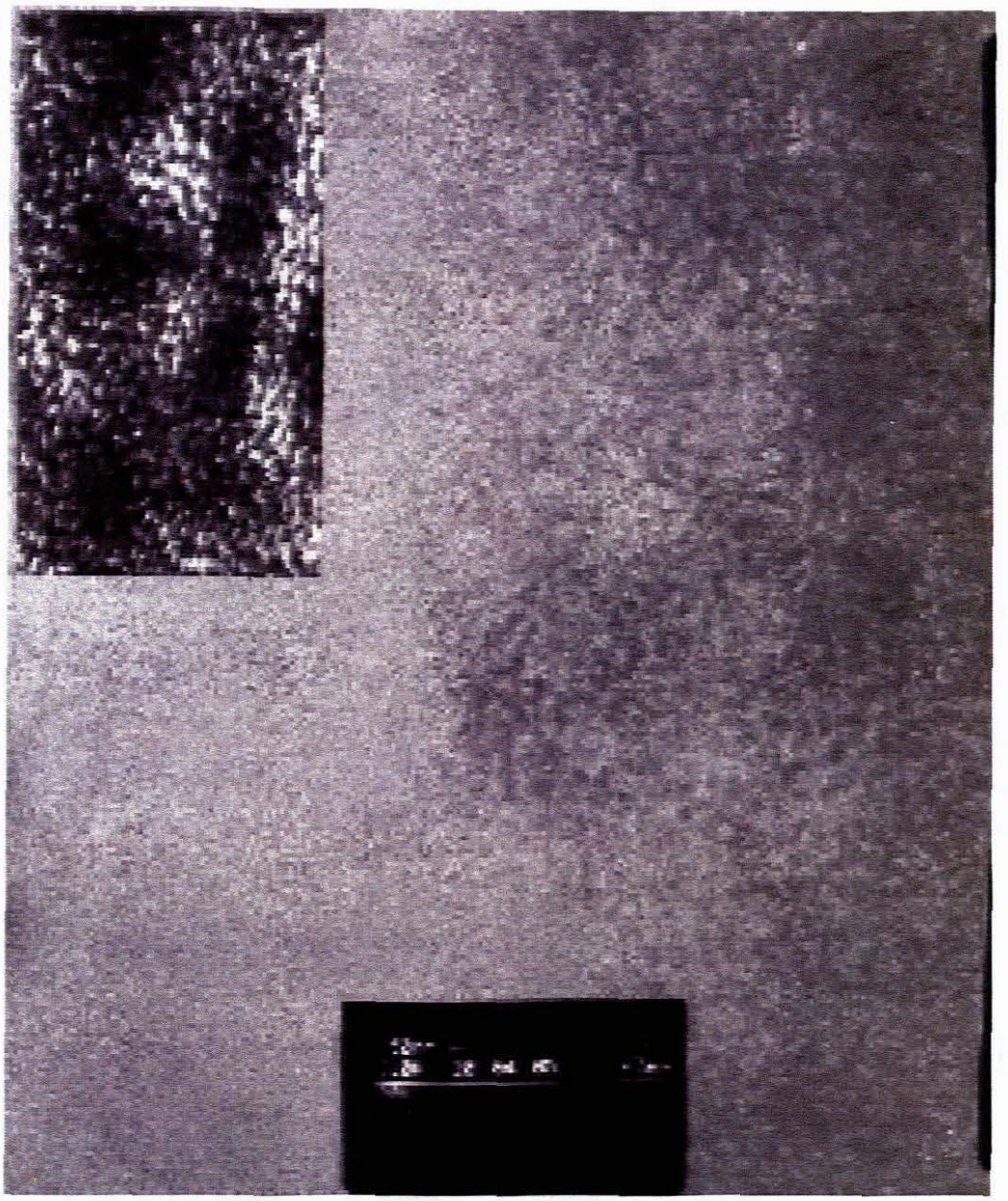

Figure 3.22: *TEM image of CdS nanorods made from complex B, $[Cd(NH_2CSNHNH_2)_2Cl_2]_n$.*

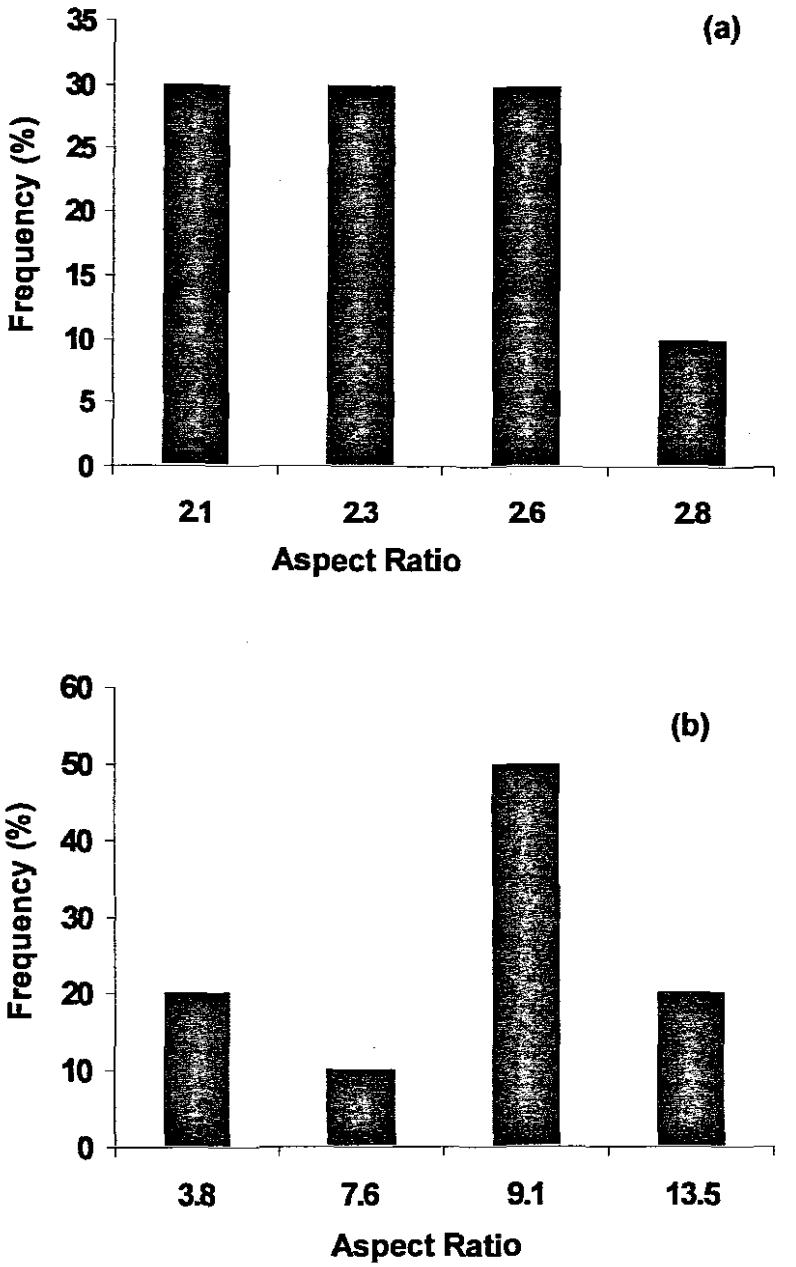

Figure 3.23: *Aspect ratio histograms for CdS nanorods made from (a) $[Cd(NH_2CSNHNH_2)Cl_2]_n$ (complex A), and (b) $[Cd(NH_2CSNHNH_2)_2Cl_2]_n$ (complex B)*

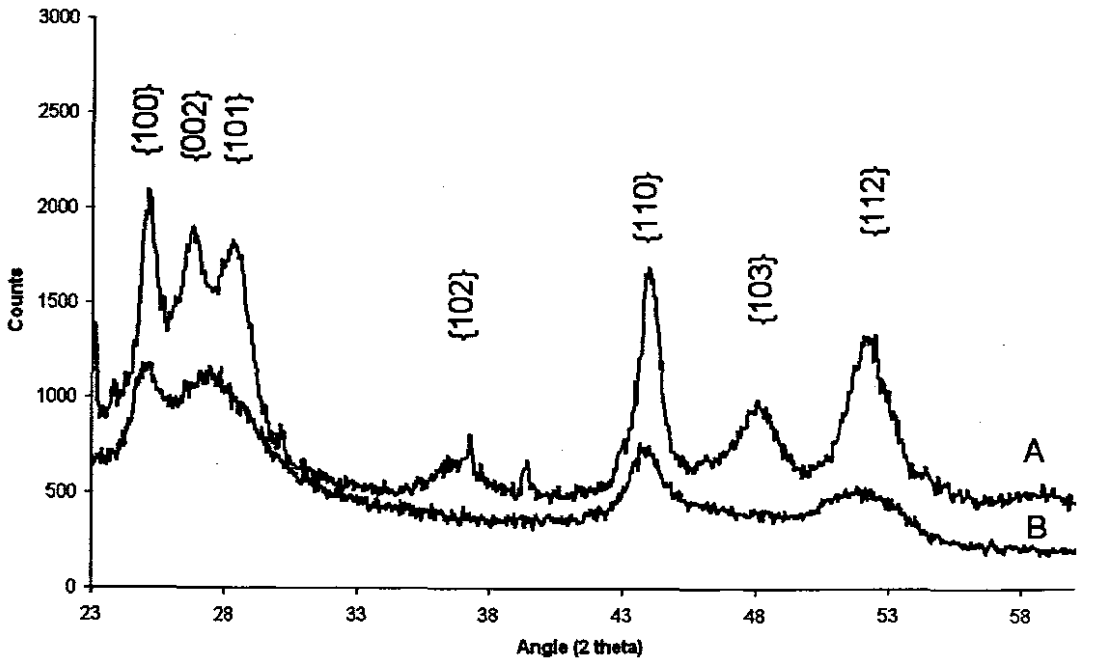

***Figure 3.24**: Powder diffraction patterns for the CdS nanorods made from complex A, $[Cd(NH_2CSNHNH_2)Cl_2]_n$, and B, $[Cd(NH_2CSNHNH_2)_2Cl_2]_n$*

3.3.5 Synthesis of the PbS nanoparticles using $[Pb(NH_2CSNHNH_2)(NO_3)_2]$

3.3.5.1 Optical Properties

PbS has a small bulk band gap of 0.41 eV (3100 nm) which makes them suitable for applications in the near IR such as in optical communication. $[Pb(NH_2CSNHNH_2)(NO_3)_2]$ was thermolysed in TOPO at 240 °C to give the dark grey colored nanoparticles. The UV/Vis spectrum of PbS shows an absorption peak that does not have an excitonic feature in the band edge. The UV/Vis. spectrum of the nanoparticles is shown in Figure 3.25. The PbS nanoparticles exhibit band edges at 375 nm (3.31 eV) and 630 nm (1.97 eV), which is a huge blue shift with respect to the bulk

PbS (3100 nm, 0.41 eV). However, it was rather surprising that these nanoparticles were non-luminescent, which could have been due to their insufficient coating by the surfactant. Sufficient coating renders the nanoparticles soluble in the non-polar solvents (such as toluene), which was not the case with PbS nanocrystals. No further determinations on shape control could therefore be carried out with this precursor because of inconsistent solubility in the polar solvents used for the optical and TEM properties of the nanocrystals, which would have lead to very inaccurate and biased results.

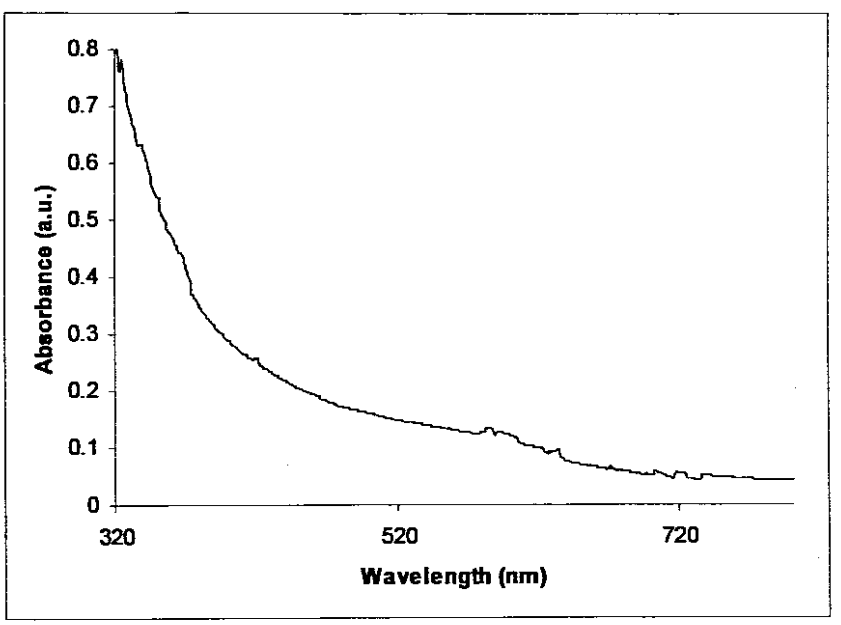

***Figure 3.25** : The UV/vis spectrum of PbS nanoparticles*

3.3.5.2 Structural properties

The prepared nanoparticles were characterized by powder XRD and TEM. PbS can exist either as the cubic or hexagonal phase even though a mixture of cubic and hexagonal phase is also possible. The powder XRD peaks observed are indexed as the face-centered cubic rock salt-like structure of PbS (Figure 3.26 (c)).[90] The sharpness and strength of the diffraction peaks suggests that the particles are crystalline. The TEM image (Figure 3.26 (a)) shows well-defined particles which are predominantly hexagonal in shape. The particles have an average size of *ca.* 7 nm. Their size distribution histograms are shown in (figure 3.26 (b)).

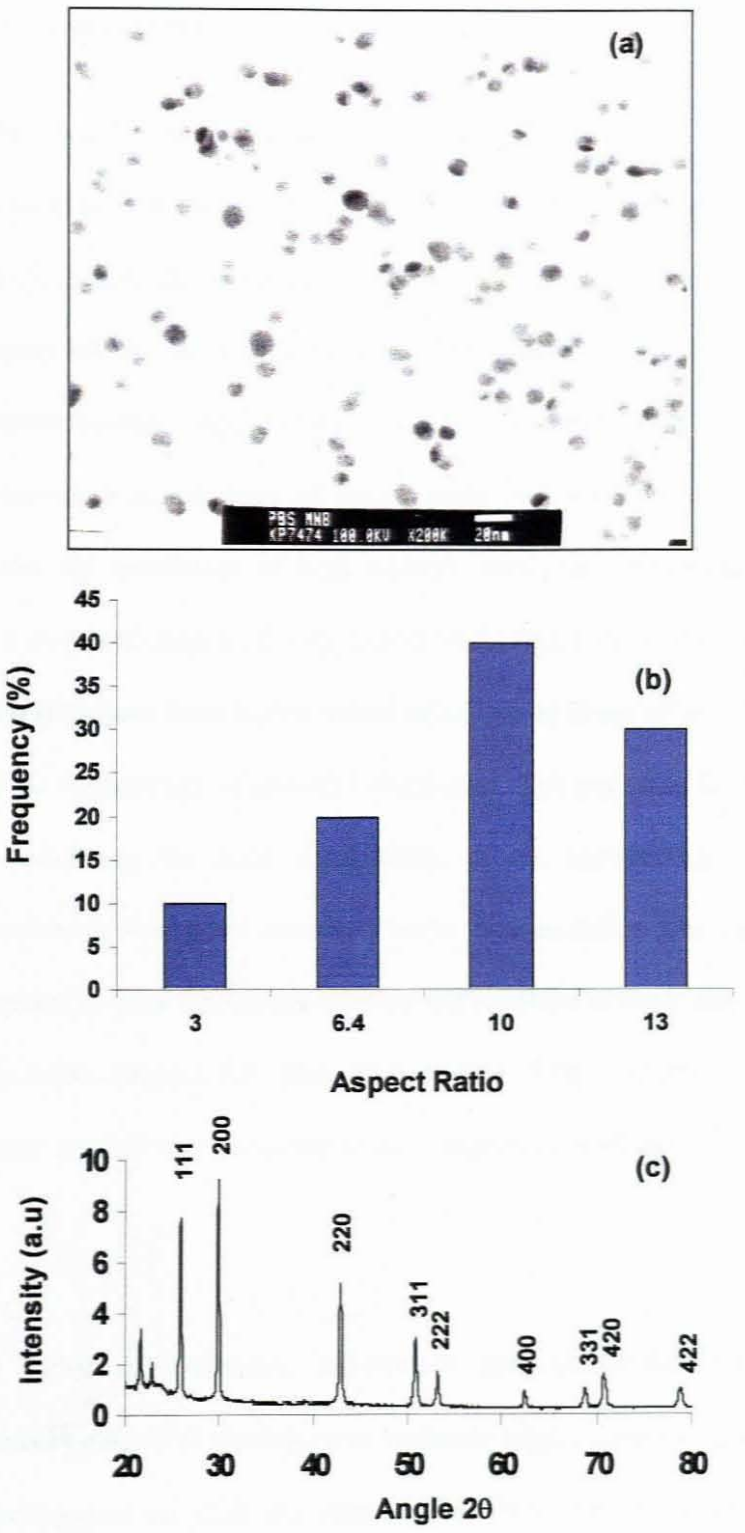

***Figure 3.26**: (a) The TEM image, (b) aspect ratio histogram, and (c) the powder diffraction pattern, of PbS nanoparticles synthesized from [$Pb(NH_2CSNHNH_2)(NO_3)_2$]*

3.4 Conclusions

The crystallographic phase of the initial nuclei and the following growth rate of the nanocrystals were found to be strongly dependent on the temperature. At higher temperatures, the reaction was thermodynamically driven, owing to the sufficient supply of the thermal energy and thus pushing the reaction system closer to the thermodynamic equilibrium. Hence, the formation of the thermodynamically determined morphology of nanocrystals is favored. In contrast, lower temperatures, under the conditions of high enough monomer concentration leads to a kinetically driven growth regime, giving nanocrystals with anisotropic morphologies. So, the shape evolution goes from higher aspect ratio rods to lower aspect ratio rods, and then to dots, as the temperature of growth is increased. The purity of the precursor plays a key role in achieving the good crystallinity of the nanoparticles, with the lattice fringes confirming this effect observed in the nanoparticles. The nature of the precursor also appears to play a profound role on the resultant crystallinity of the nanoparticles, with the more complex (complex B) analogue of the precursor giving the nanoparticles of lower crystallinity compared to the complex A analogue.

In order to synthesize anisotropic and thermodynamically metastable rod-like nanocrystals, it is necessary to maintain high monomer concentration in the reaction environment to shift the reaction far from thermodynamic equilibrium. It can be therefore concluded that the monomer concentration plays a key role in the shape controlled growth of the CdS nanocrystals. So, from higher to lower concentrations

under a condition of a moderate reaction temperature, the shape evolution goes from rods to dots, resulting from kinetic and thermodynamic regime, respectively. Shape control of PbS nanocrystals could not be achieved, due to insolubility of the nanocrystals as we move to the reaction conditions favoring larger sized structures, such as higher concentration, and hither temperatures. This precursor was not ideal for the determination of the shape evolution based on the critical parameters affecting growth.

4. References

1. S. Link, Z. L. Wang and M. A. El-Sayed, *J. Phys. Chem B*; 1999, **103**, 3529.
2. M. J. Hosteller, C. J. Zhong, B. K. H. Yen, J. Anderegg, S. M. Gross, N. D. Evans, M. Potter and R. W. Murray, *J. Amer. Chem. Soc.*, 1998, **120**, 9396.
3. Y. Wang, H. Liu and H. Toshima, *J. Phys. Chem.*, 1996, **100**, 1953.
4. M. T. Reetz, R. Breinbauer, and K. Wanniger, *Tetrahedron Lett.*, 1996, **37**, 4499.
5. L. Z. Zhang, W. Sun and P. Cheng, *Molecules 2003*, **8**, 211, 220.
6. A. A. Bol and A. Meijerink, *J. Lumin.*, 2000, **87**, 315.
7. X. Gong, W. J. Chen, P. F. Wu, W. K. Chan, *Appl. Phys. Lett.*, 1998, **73**, 2875.
8. R. N. Bhargava, D. Gallagher, X. Hong, A. Nurmiko, *Phys. Rev. Lett.*, 1994, **72**, 416.
9. S. Sun, C. B. Murray, L. Folks, A. Moser, *Science 2000*, **287**, 1989.
10. T. Hyeon, *Chem. Commun.*, 2003,927.
11. L. Manna, E. C. Scher, L. Li, A. P. Alivisatos, *J. Am. Chem. Soc.*, 2002, **124**, 7136.
12. C. Mao, J. Qi, A. M. Belcher, *Adv. Funct. Mater.*, 2003, **13(8)**, 648.
13. J. Wu, Y. Jiang, Q. Li, X. Liu, Y. Qian, *J. Cryst. Growth.* 2002, **235**, 421.
14. L. Spenhel, H. Hasse, H. Weller, and A. Henglein, *J. Amer. Chem. Soc*; 1987(a), **109**, 5649.
15. L. Spenhel, H. Weller, and A. Henglein, *J. Amer. Chem. Soc*; 1987(b), **109**, 6632.
16. M. L. Steigerwald, L. E. Brus, *Annual. Rev. Mater. Sci*; 1989, **19**, 471.
17. C. Pettit, P. Lixon, and M. P. Pileni, *Annual. Rev. Mater. Sci*; 1990, **18**, 319.
18. C. B. Murray, K. R. Kagan, M. G. Bawendi, *Ann. Rev. Mater. Sci.*, 2000, **30**, 545.

19. M. G. Bawendi, M. L. Steigerawld, L. E. Brus, *Ann. Rev. Phys. Chem.*, 1990, **41**, 477.

20. T. Trindade and P. O'Brien, *Adv. Mater.*, 1996, **8**, 161.

21. T. Trindade and P. O'Brien, *Chem. Mater.*, 1997, **9**, 523.

22. P. S. Nair, T. Radhakrihsnan, N. Revaprasadu, G. A. Kolawole and P. O'Brien, *Chem. Commun*; **2002**, 564.

23. L. Z. Zhang, W. Sun and P. Cheng, *Molecules 2003*, **8**, 211, 220.

24. C. F. Landes, S. Link, M. B. Mohamed, B. Nikoobakht, A. El-Sayed, Pure. Appl. Chem. 2002, 74(9), 1675.

25. S. McGarry, Carleton University: Department of Electronics 2004, 1.

26. A. Euteneuer, R. Hellmann, R. Gobel, S. Shevel, V. Vozny, M. Vytrykhivsky, W. Petri, C. J. Klingshirn, *J. Crystal Growth.*, 1998, **184/185**, 1081.

27. K. Shimakawa, A. Kolobov, S. R. Elliot, *Adv. Phys.*, 1995, **44**, 475.

28. K. D. Kepler, G. C. Lisensky, M. Patel, L. A. Sigworth, A. B. Ellis, *J. Phys. Chem.*, 1995, **99**, 16011.

29. C. Donega, S. G. Hickey, S. F. Wuister, D. Vanmaekelbergh, A. Meijerink, J. Phys. Chem., B 2003, **107**, 489.

30. L. Qu, Z. A. Peng, X. Peng, *Nano Lett.*, 2001, **1**, 333.

31. D. V. Talapin, A. L. Rogach, A. Kornowski, M. Hasse, H. Weller, *Nano Lett.*, 2001, **1**, 207.

32. D. Kulik, H. Htoon, C. K. Shih, Y. Li, *J. Appl. Phys.*, 2004, **95(3)**, 1056

33. T. Jonson and V. K. La Mer; *J. Am. Chem. Soc*; 1947, **69**, 1184.

34. L. E. Brus, *J. Chem. Phys.* 1983, **79**, 5566; L. E Brus, *J. Chem. Phys.* 1984, 4403.

35. R. Rosetti, J. L. Ellison, J. M. Gibson, L. Brus, *J. Chem. Phys.*, 1984, **80**, 4464.

36. R. Rosetti, R. Hull, J. M. Gibson, *J. Am. Chem. Phys.*, 1985, **85**, 552.

37. M. Green, P. O'Brien, *Chem. Commun.*, 1999, 2235.

38. Y. Wang, N. Herron, *Phys. Rev.*, B 1990, **42**, 7253; Y. Wang, N. Herron, *J. Phys. Chem.* 1991, **95**,525.

39. H. J. Wazke, J. H. Fendler, *J. Phys. Chem.*, 1987, **91**, 854.

40. T. Abe, Y. Tachibana, T. Uematsu, M. Iwamoto, *Chem. Commun.*, 1995, 1617.

41. Y. Wang, A. Suna, W. Mahler, R. Kosowski, *J. Chem. Phys.*, 1987, **87**, 7315.

42. A. R. Kortan, R. Hull, R. L. Opila, M. G. Bawendi, M. L. Steigerwald, P. J. Carrol, L. E. Brus, *J. Am. Chem. Soc.*,1990, **112**, 1327.

43. M. L. Steigerwald, A. P. Alivisatos, J. M. Gibson, T. D. Harris, T. D. Harris, R. Kortan, A. J. Muller, A. M. Tayer, T. M. Duncan, D. C. Douglas, L. E. Brus, *J. Am. Chem. Soc.*, 1988, **110**, 3046.

44. C. B. Murray, D. J. Norris, M. G. Bawendi, *J. Am. Chem. Soc*, 1993, **115**, 8706.

45. N. Revaprasadu, M. A. Malik, J. Cartens, and P. O'Brien, *J. Mater. Chem*; 1999, **9**, 2885.

46. A. A. Guzelian, J. E. B. Katari, U. Banin, A. V. Kadavanich, X. Peng, A. P. Alivisatos, K. Hamed, E. Juban, R. H. Wolters, C. C. Arnold, J. R. Heath, *J. Phys. Chem*; 1996, **100**, 7212.

47. T. Trindade, P. O'Brien, X. Zhang, *Chem. Mater.*, 1997, **9**, 523.

48. P. S. Nair, T. Radhakrihsnan, N. Revaprasadu, G. A. Kolawole and P. O'Brien, *Polyhedron*; 2003, **22**, 3129.

49. M. Harvey, S. Baggio, L. Suescun, R. Baggio, *Acta. Cryst.*, 2000. **C56**, 811.

50. Y. Tian, W. Yu, M. Jiang, S. S. S. Raj, P. Yang, H. Fun, *Acta. Cryst.*, 1999, **C55**, 1639.

51. M. K. Woode, R. F. Bryan, D. A. Bekoe, *Acta. Cryst.*, 1987, **C43**, 2324.

52. S. B. Novacović, Z. D. Tomić, V. Jevtović, V. M. Leovac, *Acta Cryst.*, 2002, m358.

53. M. A. Ali, M. Nazimuddin, H. Rahman, R. J. Butcher, *Transition Metal Chemistry*, 2002, 268

54. J. S. Casas, M. V. Castano, E. E. Castenallo, M. S. Garcìa-Tasende, A. Sćnchez, M. Sanjuán, J. Sordo, *Eur. J. Inorg. Chem.*, 2000, 83.

55. Y. Tian, C. Duan, C. Zhao, X. You, T. C. W. Mak, Z. Zhang, *Inorg. Chem.*, 1997, **36(6)**, 1247.

56. M. Jiang, Q. Fang, *Adv. Mater.*, 1999, **11(13)**, 1147.

57. R. Ballard, D. B. Powell, U. A. Jayasooria, *Acta Cryst.*, 1974. **B30**, 1111.

58. E. Labisbal, A. Sousa-Pedrares, W. Kaminsky, D. X. West, *Polyhedron*, in press.

59. D. X. West, S. B. Padhye, P. B. Sonawane, *Structural Bonding*, 1991, **76**, 4.

60. J. S. Casas, M. V. Castano, M. S. Garcia-Setende, J. Sordo, J. Zukerman-Schpector, *Z. Anorg. Allg. Chem.*, 1997, **623**, 825.

61. J. Parr, Polyhedron, 1997, **16(4)**, 551.

62. A. R. Mahjoub, A. Morsali, *Polyhedron*, 2002, **21**, 1223.

63. L. Shimoni-Livny, J.P. Glusker, C.W. Bock, *Inorg. Chem.*, 1998, **37**, 1853.

64. A. Morsali, A. Mahjoub, *Inorg. Chem. Commun.*, 2004, **7**, 915.

65. A. Morsali, A. Mahjoub, *Polyhedron*, 2004, **23**, 2427.

66. D.B. Mitzi, S. Wang, C.A. Feild, C.A. Chess, A.M. Guloy, *Science*, 1995, **267**, 1473.

67. P.G. Lacroix, R. Clement, K. Nakatani, J. Zyss, I. Ledoux, Science, 1994, **263**, 658.

68. S.D. Cox, T.T. Giex, G.D. Stuky, J. Bierlein, J. Am. Chem. Soc.,1988, **110**, 2986.

69. H.G. Zhu, Z.Yu, H. Cai, X.Z.You, J.J. Vittal, G.K. Tan, *Chem. Lett.*, 1999, 289.

70. D.B. Mitzi, K. Liang, S. Wang, *Inorg. Chem. Lett.*, 1998, 321.

71. V. Chakravarthy, A.M. Guloy, *Chem. Commun.*, 1997, 697.

72. H. Zhu, Y. Xu, Z. Yu, Q. Wu, H. Fun, X. You, *Polyhedron*, 1999, **18**, 3491.

73. K. Liang, D.B. Mitzi, M.T. Prikas, *Chem. Mater.*, 1998, **10**, 403.

74. G.A. Mousdis, V. Gionis, G.C. Papavassiliou, C.P. Raptopoulou, A. Terzis, *J. Mater. Chem.*, 1998, **8**, 2259.

75. A.B. Conadi, S. Bruni, F. Cariati, A.M. Ferrari, A. Saccani, F. Sandrolini, P. Sgaraboto, *Inorg. Chim. Acta.*, 1997, **254**, 137.

76. G. V. Romanenko, Z. A. Savelieva, and S. V. Larinov, *J. Struc. Chem.*, 2001, **42(5)**, 868.

77. R. A. L. Jones, 2002, Molecular Order in Soft and Condensed Matter, 1-18.

78. L. Gasque, S. Barnes, R. Ferrari, C. R. de Barbarin, M. J. Gutierrez, G. Mendoza-Diaz, *Polyhedron*, 2000, **19**, 649.

79. M. S. Atanassova, G. D. Dimitrov, *Spectrochimica Acta*, 2003, **A59**, 1655.

80. Y. Jun, Y. Jung, J. Cheon, *J. Am. Chem. Soc.*, 2002, **124(9)**, 615.

81. G. Markovich, C. P. Collier, S. E. Henrichs, F. Remacle, R. D. Levine, J. R. Heath, *Acc. Chem. Res.*, 1999, **32**, 415.

82. X. Peng, *Adv. Mater.*, 2003, **15(5)**, 459.

83. Z. A. Peng, X. G. Peng, *J. Am. Chem. Soc.*, 2002, **124**, 3343.

84. J. T. Hu, L. S. Li, W. D. Yang, L. Manna, L. W. Wang, A. P. Alivisatos, *Scienc,* 2001, 292, 2060.

85. E. C. Scher, L. Manna, A. P. Alivisatos, *Phil. Trans. R. Soc. Lond.*, A 2003, **361**, 241.

86. Y. Li, X. Li, C. Yang, Y. Li, *J. Chem. Mater.*, 2003, **13**, 2461.

87. L. Manna, E. Scher, A. P. Alivisatos, *J. Cluster Science*, 2002, **13(4)**, 521.

88. X. G. Peng, L. Manna, W. D. Yang, J. Wickham, E. Scher, A. Kandavich, A. P. Alivisatos, *Nature*, 2000, **404**, 59

89. S. Lee, S. Cho, J. Cheon, *Adv. Mater.*, 2003, **15**, 441

90. Joint Committee on Powder Diffraction Standards, Diffraction Data File, No. 05-0592, PCPDS International Centre for Diffraction Data, Pensylvania, 1991.

91. S. D. Bunge, K. M. Krueger, T. J. Boyle, M. A. Rodriguez, T. J. Headley and V. Colvin, *J. Mater. Chem.*, 2003, **13**, 1705.

92. X.G. Peng, L. Manna, W.D. Yang, J. Wickham, J. Scher, A. Kadavanich and A.P. Alivisatos, *Nature*, 2000, **404**, 59.

93. M. A. Malik, N. Revaprasadu, and P. O'Brien, *Chem. Mater.*, 2001,**13**, 913.

94. M. Green and P. O'Brien, *Chem. Commun.*, 1998, 2459.

95. T. Trindade, P. O' Brien and N. Pickett, *Chem. Mater.*,**13**, 2001, 3843.

96. B. O. Regan, M. Grzatzel, *Nature*, 1991, **353**, 373.

97. M. Gratzel, A. J. Frank, *J. Phys. Chem.*, 1982, **86**, 2964.

98. A. Gafeldt, M. Gratzel, *Chem. Rev.*, 1995, **95**, 49.

99. M. Summers, and J. Eastoe, *Advanced Colloid Interface Science*, 2003, **100**, 137.

100. O. L. Padilla De Jesús, *et al.*, *Bioconjugate Chem.*, 2002, **13**, 453.

101. T. Sanji, *et al.*, *Chem. Commun.*, 1999, **21**, 2201.